UNIVERSITÀ
DEGLI STUDI
DI PADOVA

UNIVERSITÀ DEGLI STUDI DI PADOVA

Dipartimento di Fisica e Astronomia "Galileo Galilei"

Ph.D. Degree in Physics

XXXVI cycle

Complete Study of Proton Capture on Carbon Isotopes at Astrophysical Energies

Coordinator	**Ch.mo Prof. Giulio Monaco**
Supervisor	**Prof. Antonio Caciolli**
Co-Supervisor	**Dr. Axel Boeltzig**

Candidate **Jakub Skowronski**

Academic Year 2022/2023

Nothing behind me, everything ahead of me,
as is ever so on the road.

Jack Kerouac, *On the Road*

Abstract

This thesis presents a comprehensive investigation of the $^{12}C(p,\gamma)^{13}N$ and the $^{13}C(p,\gamma)^{14}N$ reactions, crucial elements that help in understanding different stages of stellar evolution. In particular, the ratio of carbon isotopes, $^{12}C/^{13}C$, directly observable in the stellar atmospheres, is profoundly impacted by the dynamics of stars. Thus, it is a useful observable that can be tested against the stellar models to better constrain the mixing phenomena within Red Giant Branch (RGB) and Asymptotic Giant Branch (AGB) stars, offering valuable insights into their evolution. Additionally, the carbon isotopic ratio serves as a potent tool to study the chemical evolution of galaxies.

The primary focus of this study was the determination of precise cross section data for these reactions, achieved through experiments conducted at LUNA, located in the Laboratori Nazionali del Gran Sasso (LNGS), both the $^{12}C(p,\gamma)^{13}N$ and the $^{13}C(p,\gamma)^{14}N$, and at Felsenkeller laboratories, only the $^{12}C(p,\gamma)^{13}N$. The energy range covered in the former is $E_p = 70 - 400$ keV, the latter instead is $E_p = 320 - 620$ keV. By employing multiple experimental techniques and performing rigorous cross checks, highly precise cross section data were obtained for the $^{12}C(p,\gamma)^{13}N$ and $^{13}C(p,\gamma)^{14}N$ reactions. Additionally, an in depth characterization of systematic uncertainties was performed with several supplementary measurements to enhance the reliability of the results. The results show cross sections approximately 30 % lower for both reactions with respect to the literature values.

The novel $^{12}C/^{13}C$ ratio derived from this study, in combination with the obtained reaction rates, can significantly advance our ability to model and understand the mixing phenomena occurring in stars. The improved precision facilitates the constraining of theoretical stellar models against the observations, leading to more accurate predictions of stellar evolution and nucleosynthesis processes.

Contents

Chapter 1

Introduction

The research in Nuclear Astrophysics is of fundamental importance to understand the origin of all the elements in our Universe. It focuses on studying the intricate nuclear reaction networks that are responsible of creating nuclei heavier than H and that drives the stellar evolution. Stars are the main blacksmith of our Universe that not only produce the energy necessary for life on Earth, but also creates more and more complex elements inside their cores that make up everything in our Universe. Thus, by knowing the rates of these reactions inside stellar interiors it is possible to study the evolution of our Universe.

In this chapter the main concepts of stellar evolution will be illustrated, focusing on two different types of stars that are particularly prolific in terms of nucleosynthesis. Then the main ingredients of the reaction mechanism inside the stars will be explained. Finally, the two reactions under study, namely the $^{12}\mathrm{C}(p,\gamma)^{13}\mathrm{N}$ and $^{13}\mathrm{C}(p,\gamma)^{14}\mathrm{N}$ will be described and the state of the art discussed.

1.1 Stellar Evolution

Hydrogen and helium are still the most abundant elements in our Universe. Most of these are located in the interstellar medium in form of a interstellar nebula. This could be created either from the nuclei directly coming from the Big Bang itself or from the remnants of an already died star. When the mass of the elements reaches the critical value, the gravitational force starts to compress all the nuclei, which as a consequence increase their kinetic energy and thus the temperature. When the density and the energy of the nuclei is high enough, the first fusion reaction is ignited and the star is born.

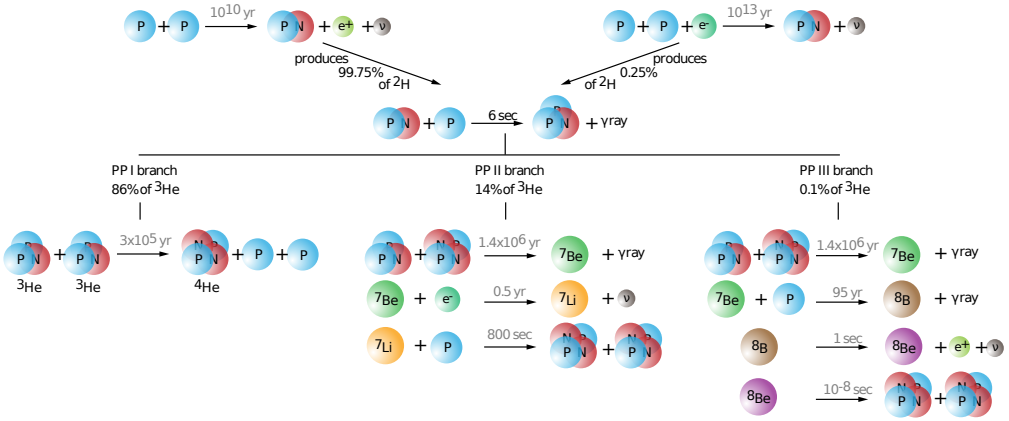

Figure 1.1: All the possible *pp* chains inside the star hydrogen burning region. Three different branches are possible. The total outcome is the ^{4}He production, but as a byproduct also some amounts of *d*, ^{3}He, ^{7}Li and ^{7}Be can be produced [2].

Initially, the star burns hydrogen to produce helium nuclei, for a total reaction of $4\,^1\mathrm{H} \rightarrow {}^4\mathrm{He} + 2\,e^+ + 2\,\nu_e$, which is referred to as hydrogen burning. This stage of the stellar life is called Main Sequence [1]. The hydrogen burning can occur through two different chains of reactions, depending on both the mass of the star and its composition. If the star is small, the main mechanism is the *pp* process. It is a chain of reactions that starts from the $p + p$ and finishes by producing one ^{4}He nucleus. In reality, the chain can be divided in three different sub-chains, predominance of which depends on the star temperature. The full structure of the *pp* chains can be seen in Fig. 1.1.

An alternative to the the *pp* process is the CNO cycle. It consists in several reactions on C, N and O nuclei that cathalitically create one ^{4}He nucleus from $4\,^1$H. The entire cycle can be seen in Fig. 1.2. This is the predominant mechanism of the hydrogen burning for star with masses approximately 1.5 higher than the solar one [1]. Nevertheless, the star composition must contain some of the nuclei that takes part in it. This propriety is called metallicity, ie. how many nuclei heavier than ^{1}H and ^{4}He does the star contain. As an example, the first generation stars, created just after the Big Bang, have very low metallicity, since no C, N nor O nuclei were produced before. Thus these, even with high enough mass, can not burn the hydrogen through the CNO cycle. Additionally, the cycle is important for the nucleosynthesis: the amounts of each isotope are changed when the cycle is ignited and reaches an equilibrium value given by the reaction rates of each of the reactions.

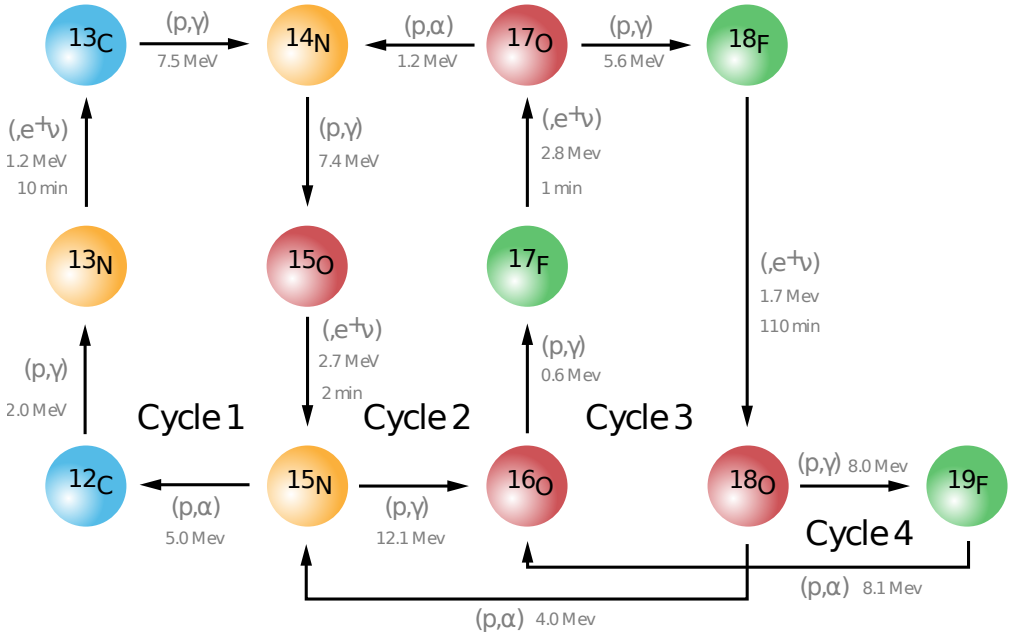

Figure 1.2: The CNO cycles inside the stellar hydrogen burning regions. Three different closed cycles are possible, depending on the star temperature [2].

Once most of the hydrogen has been burned and the star is not able to sustain itself, the hydrogen burning region is pushed towards an outer shell of the star, leaving the core made of helium. The stars thus begins to expand and cool while the core is being contracted and enters into the Red Giant Branch (RGB) phase. At this point, the first dredge up (FDU) occurs [3]. The convective motion penetrates into the hydrogen burning regions of the star and brings up heavier elements, such as carbon and nitrogen, from the stellar core to the surface. As a result of FDU, the surface elemental abundances of the star change. The newly mixed material, enriched in hydrogen burning products, is transported to the stellar surface, where it can be observed through spectroscopic analysis. This alteration of surface composition is an important aspect of stellar evolution and has implications for the chemical enrichment of the interstellar medium and the formation of subsequent generations of stars and planetary systems.

When a high enough temperature is reached in the core, the helium burning can be started inside the core which will produce enough energy to stop the core contraction. The process consists in triple ^{4}He reactions that create ^{12}C nuclei [1]. This process is highly unlikely due being a two step process: first, the ^{8}Be nucleus must be produced, which is unstable with a half life of 8.19×10^{-17} s, and then has

to capture a ^{4}He nucleus before decaying. Nevertheless, this process is favoured by the existence of the Hoyle state in the ^{12}C nuclei [1].

Once the star has exhausted most of its helium, the process called second dredge up (SDU) occurs [3], which is analogous to the FDU: the convective envelope penetrates in the helium burning regions and brings up all the produced elements to the stellar surface.

At this evolutionary point, the star usually enters its most prolific stage for nucleosynthesis: the Asymptotic Giant Branch (AGB) [3]. The stars once again expands and cools, leaving a core made of carbon and oxygen, the products of the helium burning. The helium burning starts again in a shell around the core, until the helium is mostly exhausted. At this point, the hydrogen burning starts in a thin shell around the helium one. At a certain point, when the helium builds-up significantly from the hydrogen burning shell, the helium burning ignites again. This process is known as helium flash and it repeats several times during the following star evolution. The hydrogen and helium shells are constantly switched off and on up until most of the hydrogen is burned and it can no more provide helium for the other shell.

In the meantime, the phenomena called third dredge up (TDU) occurs several times. When the hydrogen shell is switched off, the convective motion can penetrate down to the helium burning region and thus brings up all the encountered material up to the surface, enriching the surface with the helium burning products and several other elements [3]. A simplified scheme of the TDU is shown in Fig. 1.3. The TDU is thus responsible for the creation of carbon stars. Carbon stars are giant stars with a surfaces carbon abundance higher than the oxygen one, resulting from the dredge up of carbon-rich material from the helium burning ashes. These carbon stars are particularly interesting to astronomers because they play a crucial role in the chemical enrichment of the universe. Additionally, the AGB start pulsation can trigger intense mass loss in the star [4]. As the convective envelope reaches deeper layers and brings up the hot material from the deeper region, it becomes unstable leading to the ejection of stellar material in the form of stellar winds that then enrich the interstellar medium.

Once the AGB star finishes most of its helium and hydrogen, and thus is not able to maintain the burning in its shells, two fates are possible. Either the star mass is big enough to start the process of carbon burning, or it dies as a White Dwarf, ie. hot stellar core remnant made of carbon and oxygen unable to undergo further fusion

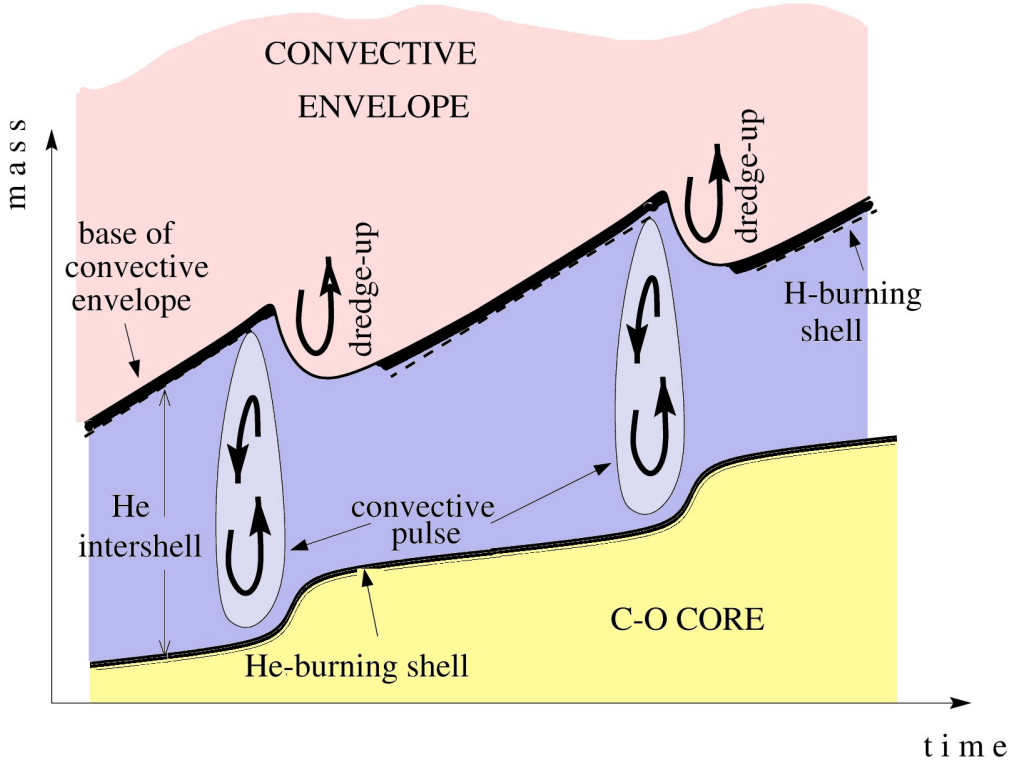

Figure 1.3: The third dredge up representation for an AGB star. The convective shell penetrates deep inside the helium burning ashes when the hydrogen burning shell is switched off. This repeats several time during the AGB phase [5].

processes. If the star mass is approximately $> 8M_{\odot}$, the ^{12}C $+^{12}$ C fusion starts inside the stellar core. At this point the star evolution is quick and straightforward with respect to the previous stages, producing heavier and heavier nuclei: once the ^{12}C has been depleted, the neon burning phase starts, followed by the neon burning, the oxygen burning and the silicon burning phases. When iron-peak elements have been reached, the star is not able anymore to produce any energy building heavier elements since the fusion processes starts to be endothermic and the stellar core inevitably collapses, exploding in the supernova and leaving either a Neutron Star or a Black Hole [1].

1.1.1 The ^{12}C and ^{13}C Ratio

As seen in the previous section, the elemental abundances in the stellar atmosphere can provide important information on both the star evolution and its nucleosynthesis. The ^{12}C and ^{13}C ratio, in particular, is an important observable since it can be readily observed in stellar spectra [6] and it an observable sensible to the non-standard mixing processes [7]. In particular, the carbon isotopic ratio in the RGB stars can give insight on the stage of their nucleosynthesis and their mixing processes. As an example, the observations show that the occurrence of FDU is linked to lower atmospheric ^{12}C/^{13}C ratios [6]. These abundances, however, are not well reproduced by standard stellar models, thus extra-mixing processes are needed to model stars that are climbing the Red Giant Branch [6]. For now, the thermohaline-induced mixing seems to give the most promising results for the low-mass stars. However, some discrepancies are still present [6]. For higher mass stars, a contribution from the rotation induced mixing is needed to describe the observed abundances, which are not affected if the star mass is too low [7].

Similar conclusion has been reached in [8] where a different type of mixing is used. It is claimed that this could derive from the magnetic buoyancy effects inside these stars, which is able to give a good description of the observed isotopic ratios. However, quite intense magnetic fields deep in the stars are required for which little evidence is still present in literature. Nevertheless, the magnetic buoyancy mixing is successfully used to describe other important variables in the AGB stars, like the formation of the ^{13}C pocket [9], which could confirm its need in the description of the AGB star mixing processes. On the other side, the mixing induced by the star rotation is able to explain the ^{13}C pocket formation as well [10].

In other studies, focused on the AGB stars, the need of extra mixing processes is evidenced by the lower ^{12}C/^{13}C ratios than expected [11]. The ^{12}C that is

brought towards the surface during the TDU phenomena must be compensated by its destruction while it crosses the hydrogen burning regions. In there, the ^{12}C is partially converted into ^{13}C and thus lower ratios are achieved in the stellar surface. Similar conclusions are reached by studying the presolar SiC grains [12]. These are thought to be created in the loosely bound atmospheres of the AGB stars, and as such can be readily used to test the AGB star models. In the newest study, some of the SiC grains present anomalies in the ^{12}C and ^{13}C isotopic ratio that still are not well understood due to the lack of knowledge in the extra mixing processes that occur inside some of the AGB stars [13].

Additionally, the ^{12}C/^{13}C ratio is a good tracer for the chemical evolution of galaxies. In [14] a positive gradient of the carbon isotopic ratio was found in function of the distance from the center of the galaxy. The ^{12}C found in the interstellar medium (ISM) is thought to be produced in three different scenarios: the AGB stars, that loose their mass through the TDU episodes, the heavy stars that explodes in supernovae and the White Dwarfs that accrete material from a companion star and hence explode as a supernovae [14]. The ^{13}C instead is mainly expelled from the AGB stars, where it is produced through the CNO cycle. The latter contribution is delayed because it involves low or intermediate AGB stars, which lifetimes are generally much larger. Hence, the observation of a positive gradient is a direct consequence of the more frequent star cycling in the center of the galaxy, where the gas density is higher, with respect to the outer regions [14]. As this hypothesis describes very well the data, the ^{12}C/^{13}C can be used to estimate the date and position at which planetary systems were born, since this value is locked at their formation time.

Finally, in order to improve the models for both the extra mixing in the RGB and AGB stars, and have a more precise description of the chemical evolution of galaxies, having a precise reaction rate for both the ^{12}C$(p,\gamma)^{13}$N and ^{13}C$(p,\gamma)^{14}$N reaction is mandatory. This is due to the fact that the carbon isotopic ratio in the hydrogen burning regions is directly proportional to these two quantities.

1.2 Nuclear Reactions in Stars

In order to understand how the nuclear reaction occur inside the stellar interiors, it is necessary to introduce the reaction rate formalism. Generally, it is possible to describe a nuclear reaction inside the stars as:

$$a + b \rightarrow c + b \tag{1.1}$$

where the $a+b$ is the entrance channel and $c+b$ is the exit channel, which includes either particles or radiation that takes part in it. The fundamental quantity that describes the probability of each type of reaction is the cross section, $\sigma(E)$ [1], which depends on the energy, E, of the system in the Center of Mass (CM) reference. This refers only on occurrence of a single reaction, wheres inside the stars many particles of type a and b are present. Additionally, the energy is not unique. The star, in fact, can be modelled as an ideal gas where the particle velocities, v, follow a Maxwell Boltzmann distribution, $\phi(v)$. Thus, the number of reactions per unit time and unit volume, r_{ab}, can be written as:

$$r_{ab} = N_a N_b \int_0^\infty \phi(v) v \sigma(v) dv \tag{1.2}$$

$$= N_a N_b \left\langle \sigma v \right\rangle_{ab} \tag{1.3}$$

where N_a and N_b are the number densities of particles a and b, respectively, and $\left\langle \sigma v \right\rangle_{ab}$ is the reaction rate per particle pair. The latter is one of the most important quantities in the nuclear astrophysics. This value, however, is usually very low and the r_{ab} is increased by extremely high particle densities inside the stellar core. This is due by the fact that particles inside the stars have relatively low energies, eg. a temperature of 0.2 GK, typical of hydrogen burning in RGB stars [15], corresponds to a mean energy of about 20 keV. Hence, the cross section at such low energies drops exponentially due to the presence of the Coulomb barrier [1] and the reaction is mainly driven by the quantum tunneling effect. For this reason, the cross section is usually parameterized as:

$$\sigma(E) = \frac{1}{E} \exp\left(-2\pi\eta(E)\right) S(E) \tag{1.4}$$

$$2\pi\eta(E) = 0.989534 Z_0 Z_1 \sqrt{\frac{1}{E} \frac{M_0 M_1}{M_0 + M1}} \tag{1.5}$$

where the $1/E$ factor is associated to the de Broglie wavelength, the $\exp\left(-2\pi\eta(E)\right)$ is the factor proportional to the tunneling probability, with $\eta(E)$ being the Sommerfeld parameter, $S(E)$ is the astrophysical S-factor, the Z_0 and Z_1 are, respectively, the atomic numbers of the projectile and the target and M_0 and M_1 are

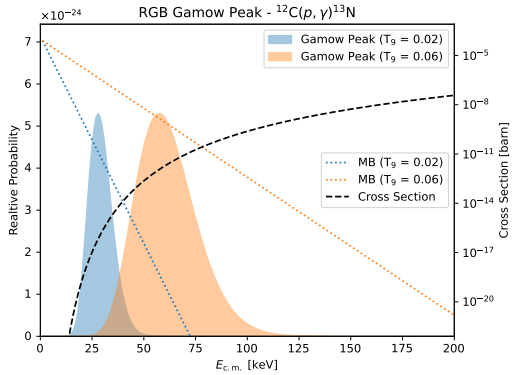

Figure 1.4: Two Gamow peaks for the $^{12}C(p,\gamma)^{13}N$ reaction for, respectively, the minimum and the maximum temperature in the RGB hydrogen burning region [15].

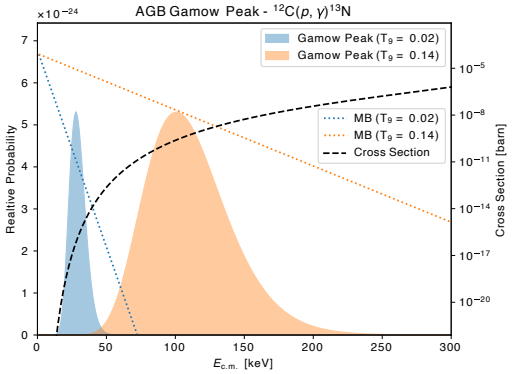

Figure 1.5: Two Gamow peaks for the $^{12}C(p,\gamma)^{13}N$ reaction for, respectively, the minimum and the maximum temperature in the AGB hydrogen burning region [16].

the masses (in amu) of, respectively, the projectile and the target [1]. The latter is the variable that incorporates all the nuclear structure proprieties of the compound that is being formed and as such has much more steady dependence on the energy, since the exponential has been factored out. This is incredibly helpful to extrapolate the cross section at the energy ranges of interest, which are otherwise mostly inaccessible for the experiments.

In order to estimate the energy region of interest, it is possible to plug the Equation 1.4 inside the reaction rate rate integral in Equation 1.3. The product of the cross section and the Maxwell Boltzmann distribution gives the Gamow peak [1] which indicates the energy range at which the reaction occurs inside the stellar medium at a given temperature, being the product of the energy and reaction probabilities. An example of the Gamow peak for the $^{12}C(p,\gamma)^{13}N$ reaction is shown in Fig. 1.4 and Fig. 1.5 for, respectively, RGB and AGB stars.

1.3 Proton Capture on Carbon Isotopes

The $^{12}C(p,\gamma)^{13}N$ and $^{13}C(p,\gamma)^{14}N$ consists in the capture of the proton by the respective carbon isotopes and the consequent production of a nitrogen isotope. Both the reactions are exothermic, i.e. the energy is released due to the fact that the binding energies per nucleon of both the ^{13}N and ^{14}N are higher than in the respective carbon nuclei [1]. The total difference in the binding energies is called the Q-value of the reaction and can be easily calculated from the initial and final

masses of the nuclei. In case of the $^{12}C(p,\gamma)^{13}N$, the Q-value is (1943.5 ± 0.3) keV [17], whereas for the $^{13}C(p,\gamma)^{14}N$ it amounts to (7550.5636 ± 0.0003) keV [17].

The capture of the proton can occur through two different mechanisms, namely the direct capture (DC) or resonant capture. The former refers to a mechanism where a proton is captured by a nucleus without any intermediate steps: it directly merges with the nucleus, resulting in the formation of the new compound, whether in its ground state or in an excited state, and in the simultaneous emission of a γ-ray. In contrast, resonant capture involves a two-step process. First, the incoming proton forms the compound directly in its excited state, known as a resonance. This subsequently decays to its ground state by emitting γ-rays. Resonant capture is characterized by the involvement of specific energy levels in the compound nucleus, making it highly dependent on the total energy of the reactants, ie. Q-value plus the proton energy, matching the resonant energy of the nucleus.

In both the reactions of interest, no resonance is present in the Gamow windows of the hydrogen burning regions in both AGB and RGB stars. Nevertheless, two excited states are present in the ^{13}N and in the ^{14}N nuclei, respectively, at approximately $E_p = 421$ keV and $E_p = 551$ keV, which tail can affect the cross section even at lower energies. The level scheme of the two reactions is shown in Fig. 1.6 and in Fig. 1.7. The two reactions are different in complexity: in the $^{12}C(p,\gamma)^{13}N$ only one γ-ray is emitted, whereas for the $^{13}C(p,\gamma)^{14}N$ several different excited states can be populated through the DC process and many more γ-rays are emitted, given the much complex γ-cascades.

Since the γ-rays are emitted in each reaction, these can be counted and associated to the number of occurred reactions, N_r. By dividing this term by the number of incoming protons, N_p, a quantity called reaction yield, Y, is obtained which then is linked to the reaction and target proprieties, ie. cross section, $\sigma(E)$, target thickness, ΔE, and the effective stopping power, $\epsilon(E)$, as follows [1]:

$$\left[\frac{N_r}{N_p}\right]_{exp} = Y = \left[\int_{E-\Delta E}^{E} \frac{\sigma(E)}{\epsilon(E)} dE\right]_{theo} \tag{1.6}$$

This equations make it possible to link the experimental variables to the cross section that can be then promptly extracted by using the information provided on the target thickness and composition. Since an integral is present on the right part of the equation, the value that is obtained is in reality the mean cross section

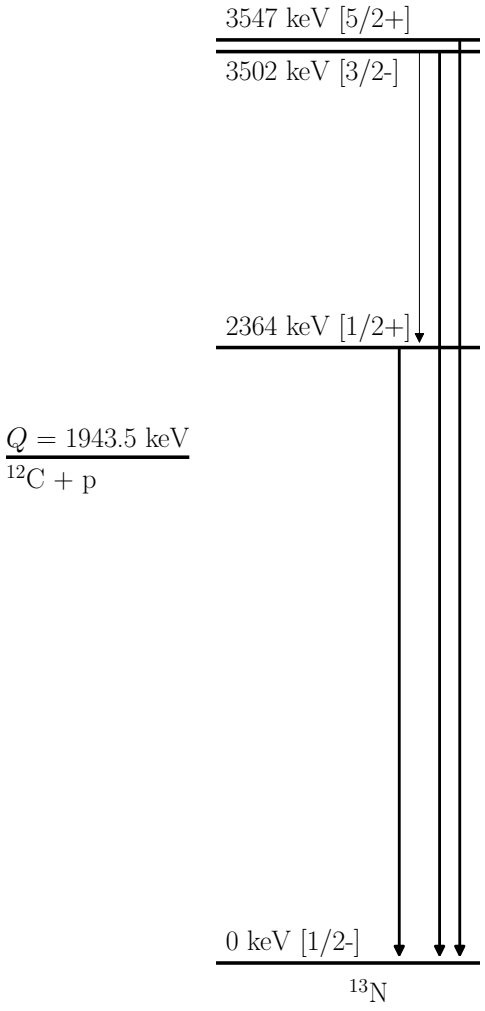

Figure 1.6: The level scheme for the $^{12}\mathrm{C}(p,\gamma)^{13}\mathrm{N}$ reaction. Only one direct capture transition to the ground state is possible.

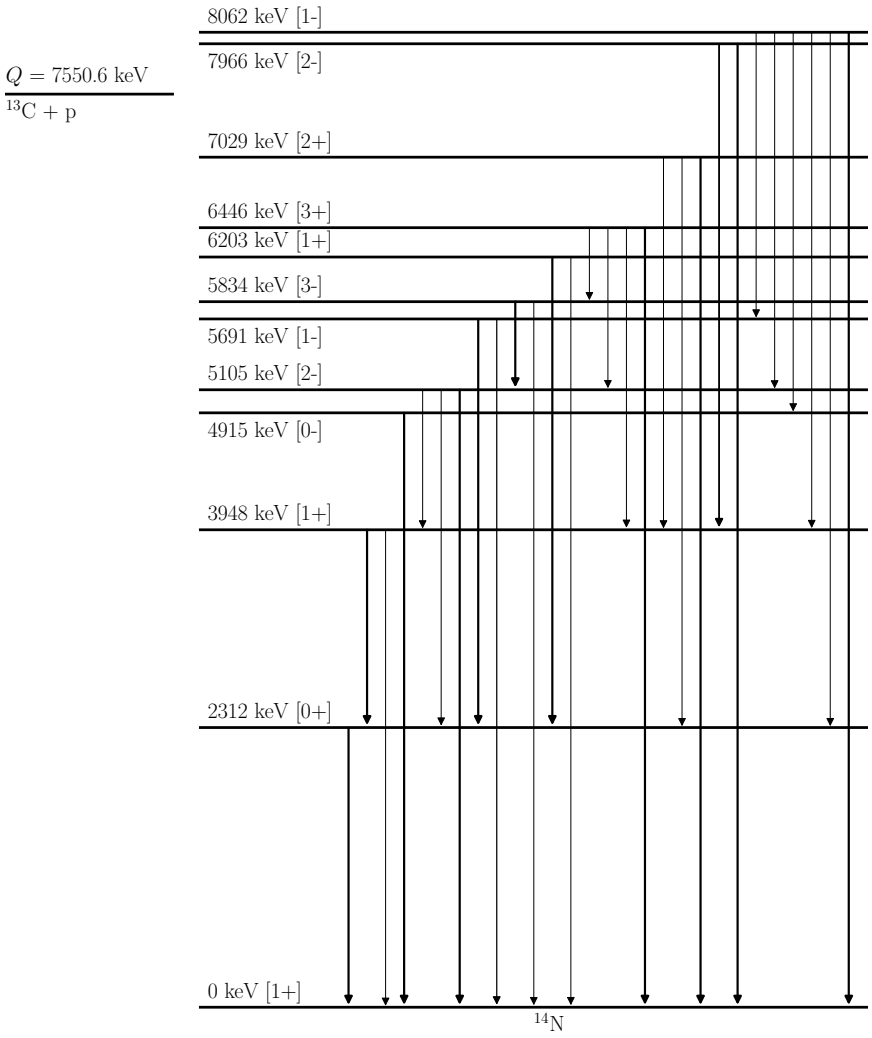

Figure 1.7: The level scheme for the $^{13}\mathrm{C}(p,\gamma)^{1N}\mathrm{N}$ reaction. Mainly the first 6 lowest levels are populated by the direct capture process that then decay by following their γ-ray cascade.

averaged over the energies spanned over the target. Thus, in order to correct for this issue, the effective energy, E_{eff}, that is then associated to the cross section, is calculated as follows [1]:

$$E_{\text{eff}} = \frac{\int_{E-\Delta E}^{E} \sigma(E) E dE}{\int_{E-\Delta E}^{E} \sigma(E) dE} \tag{1.7}$$

These two equations are fundamental to obtain the cross section for both the reactions under study. In the following, the review of all the literature studies for both the reaction will be revised.

1.3.1 State of the Art - $^{12}\text{C}(p,\gamma)^{13}\text{N}$

The $^{12}\text{C}(p,\gamma)^{13}\text{N}$ was studied several times in the past. In Fig. 1.8 the literature cross section data in form of the astrophysical S-factor are shown. In the following brief descriptions of each study is given:

Hall and Fowler (1950) [18] The reaction was studied between 88 keV and 128 keV by counting the emitted positrons from the decay of ^{13}N nuclei. The target was made from pure graphite disk. The data acquisition took place only after the sample was irradiated and brought to the counting station. Slightly higher ^{13}N life time of $((10.13 \pm 0.10)$ min) than the current value of (9.965 ± 0.004) min is reported in the paper. Only the yield values are reported in the paper in form of a plot with a statistical uncertainty of 20 %. No cross section value is reported, although the details of its calculation is discussed. The systematic effects due to the accelerator voltage inaccuracy and the stopping power uncertainty are reported as 10 % each.

Bailey et al. (1950) [19] The reaction cross section was studied in the energy range between 125 keV and 200 keV. A 0.5 mm thick carbon target was used. The positrons emitted by the decay of the ^{13}N nuclei were counted. The obtained yield values are in agreement with the Hall and Fowler study. The cross section data are reported in the plot with a statistical uncertainty ranging from 5 % up to 10 %. A 10 % systematic uncertainty due to the stopping power is reported.

Vogl PhD. Thesis (1963) [20] The $^{12}\text{C}(p,\gamma)^{13}\text{N}$ reaction was studied in three different energy ranges. Below 300 keV a soot target of unknown thickness was

used. In the region between 300 keV and 480 keV evaporated targets with 39 % of ^{12}C were employed which thicknesses were obtained by scanning the 448 keV narrow resonance in the $^{13}C(p,\gamma)^{14}N$ reaction, whereas above 480 keV methyl iodide targets, with calculable thicknesses were used. The γ-rays were detected with a NaI(Tl) crystal. Additionally, a plastic scintillator was used as an anti-coincidence shield to reduce the observed background. The soot target data were normalized to the evaporated ones to have a good overlap in the cross section. The low energy data agree with the past studies, however large statistical uncertainty is present in the overlap region. No major insight is provided for the systematic errors. The cross section data are provided in a table.

Rolfs and Azuma (1974) [21] The reaction cross section was measured in the energy range between 150 keV and 2500 keV. Both the 457 keV and 1699 keV resonances were studied. The experiments were conducted in two different facilities for, respectively, first and second resonance. However, it is not clear which is the clear energy cut. The targets were made by depositing the ^{12}C on tantalum backings. The γ-rays were observed with two Ge(Li) detectors at, respectively, 0° and 90°. The data were normalized to the elastic scattering cross section by performing a run at 250 keV where protons were detected. The rest of the data points were then normalized to that value. The data are provided in form of the differential cross section plots, thus these are rather problematic to be extracted precisely. They are in good agreement with the previous studies. No systematic uncertainty is discussed.

Burtebaev et al. (2008) [22] The reaction was studied at 7 different energies in the 354 – 1061 keV range. A HPGe detector was used to observe the emitted γ-rays. The targets were made by evaporating first Ta, then ^{27}Al and finally $^{!2}$C on Cu backings. The Ta layer was needed to reduce the proton energies when reaching the Cu layer. The ^{27}Al layer, instead, was used to measure the thickness of the ^{12}C by looking at the energy shift of the 992 keV narrow resonance. The cross sections are provided in a table. The overall reported systematic uncertainty is 10.2 % and a good agreement was found with the previous results.

Gyürky et al. (2023) [23] The cross section was studied in the 300 – 1900 keV range. The targets were prepared by electron beam evaporation of graphite on tantalum backings and were then characterized by using the (1747.6 ± 0.9) keV narrow resonance of the $^{13}C(p,\gamma)^{14}N$ reaction. The number of ^{13}N decays was

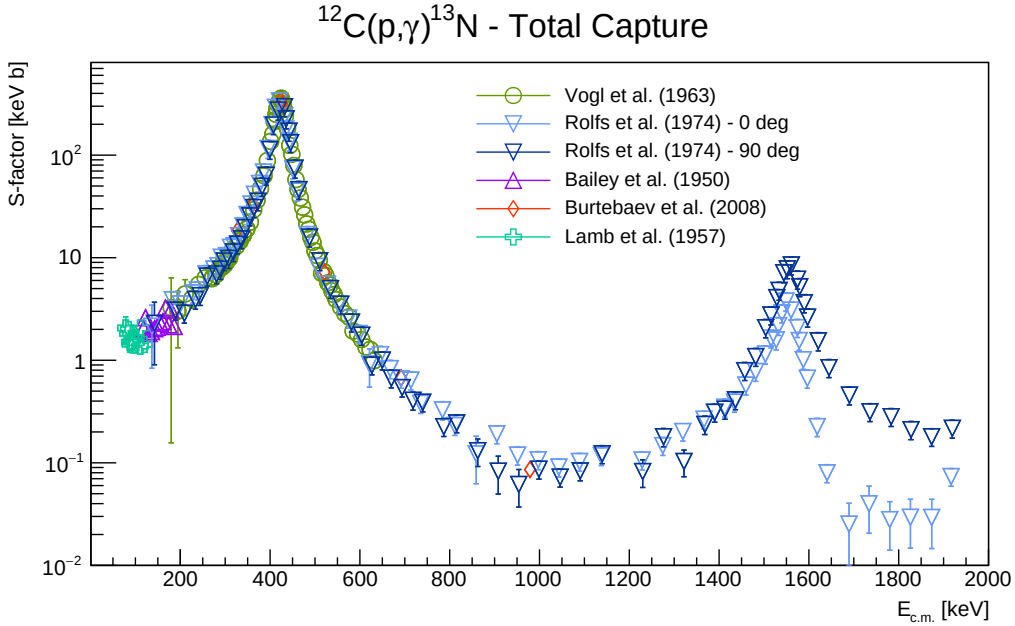

Figure 1.8: The literature S-factor values for the $^{12}\mathrm{C}(p,\gamma)^{13}\mathrm{N}$ reaction. The Rolfs differential data were multiplied by 4π in order to compare it with the other datasets.

counted by observing the 511 keV γ-rays emitted by the annihilation events due to the positron emission. Cross section data are presented in a table with both the statistic and total uncertainties. Even if the authors claims the data are in good agreement with the literature, the cross sections for energies lower than 600 keV are approximately 20 % lower.

1.3.2 State of the Art - $^{13}\mathrm{C}(p,\gamma)^{14}\mathrm{N}$

The $^{13}\mathrm{C}(p,\gamma)^{14}\mathrm{N}$ reaction was focus of many experiments in the past. However, only one of these measured the cross section for all the transitions, whereas the others focused on the capture to the ground state. In Fig. 1.9 the literature cross section data in form of the astrophysical S-factor are shown for the latter one and in the following brief descriptions of each study is given:

Seagrave (1952) [24] The reaction was studied between 400 keV and 2700 keV. The detection system consisted in Geiger tubes. Both thick and thin targets were used by evaporating ^{13}C on silver backings. The yield data are provided over the wide energy range in form of plots. The cross sections are provided in a table only at the top of the resonances.

Woodbury and Fowler (1952) [25] The cross section is obtained only at the proton energy of 129 keV. A NaI crystal was used to count the γ-rays emitted in the reaction. The targets were made by cracking enriched methyl iodide on tantalum strips and the narrow resonance at (1747.6 ± 0.9) keV was used to characterize them. The obtained cross section value is compared with an extrapolated value from the Seagrave (1952) study with an observed value about 50 % higher than the extrapolated one.

Hester and Lamb (1961) [26] In this measurement, graphite targets with 1.1 % abundance of ^{13}C were employed. A NaI crystal was used to count the emitted γ-rays. The efficiency was obtained by extrapolating the integral bias curve. A 1 % precision is stated for the accelerator voltage. The cross section was obtained from the observed yields assuming an infinitely thick target. The obtained values are in good agreement with the Woodbury and Fowler (1952) measurement.

Vogl PhD. Thesis (1963) [20] The $^{13}\mathrm{C}(p,\gamma)^{14}\mathrm{N}$ measurements were conducted in the same manner as the previously discussed $^{12}\mathrm{C}(p,\gamma)^{13}\mathrm{N}$. Only the cross section values for transition to the ground state are reported. In general, a good agreement was found with the previous studies. However, a small disagreement with respect to the Hester and Lamb (1961) is stated.

King et al. (1994) [27] In this study, six different transitions in the $^{13}\mathrm{C}(p,\gamma)^{14}\mathrm{N}$ reaction were investigated in the beam energy range between 120 keV and 950 keV. Two different accelerator setups were used for, respectively, the measurements in $E_p = 120 - 325$ kev and $E_p = 255 - 950$ kev ranges. The targets were prepared by evaporating the carbon powder, enriched up to 99 % in ^{13}C, on tantalum backings. These were characterized with the use of the 448 keV narrow resonance. As an additional cross check, the shape of the primary γ-ray was used for the target thickness estimation. The γ-rays were observed with both Ge(Li) and Ge detectors, calibrated in efficiency with calibration sources and proton induced reactions. The detectors were positioned at 0°, 45°, 90° and 135°, thus the angular distribution of several primary transitions were studied. The absolute cross sections were obtained relative to the $^{14}\mathrm{N}(p,\gamma)^{15}\mathrm{O}$ and $^{19}\mathrm{F}(p,\alpha\gamma)^{16}\mathrm{O}$ resonances. The obtained energy of the broad resonance at 0.55 MeV is shifted by approxiamtely 5 keV with respect to Vogl PhD. Thesis (1963). A systematic uncertainty of 11.7 % is reported for the absolute normalization. Finally, the extrapolations at stellar energies is obtained and the reaction rate calculated.

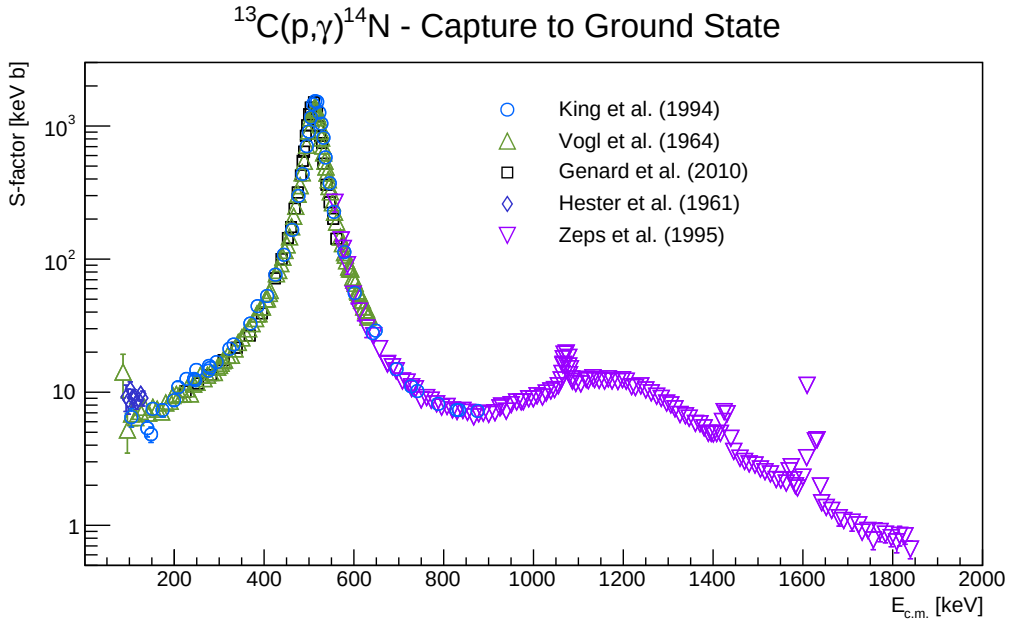

Figure 1.9: The literature S-factor values for the $^{13}\mathrm{C}(p,\gamma)^{14}\mathrm{N}$ reaction. Only the transition to the ground state is showed since it is the most studied one. The Zeps data were arbitraily renormalized to make them comparable with the other datasets.

Zeps et al. (1995) [28] This study focuses on the nuclear theory to describe the mixing within the ^{14}N nuclei. Nevertheless, many resonances were studied in the energy range between 500 keV and 2000 keV, reporting new $\omega\gamma$ values for high lying resonances. No information is provided on the target production, which was characterized with the narrow resonance at 1.75 MeV. Both NaI and Ge(Li) detectors were used to count the emitted γ-rays. For what concerns the cross data, only not normalized values are available. The reported energy for the 0.55 MeV resonance indicates a possible 5 keV shift in the King et al. (1994) result.

Genard et al. (2010) [29] Unlike other studies, the reaction was performed in inverse kinematics. The ^{13}C beam impinged on the ^{1}H target implanted in silicon backing. The γ-rays were detected with the use of an HPGe detector. The $^{15}\mathrm{N}(p,\alpha\gamma)^{12}\mathrm{C}$ reaction was used to characterize the target. The cross section was measured in the $E_p = 225 - 561$ keV range, only for the transition to the ground state. The result for the $\omega\gamma$ of the 551 keV resonance is approximately 30 % lower than the value reported in King et al. (1994). However, the work was never published and only a conference proceeding exists.

Chapter 2

Experimental Campaign at LUNA

Due to the significant decrease in cross section below the Coulomb barrier and the low energies involved in astrophysical contexts, determining the cross sections of reactions induced by charged particles is challenging. The experiments usually must be designed to measure extremely small cross sections, on the order of pico to femto barn or less. This makes it necessary to reduce the potential noise, in this case the cosmic and environmental radiation, as much as possible. Additionally, the accelerator used in these experiments must provide an intense and stable beam over long periods of time and should have the smallest possible energy spread.

The LUNA experiment [30] is one of the few places in the world where all these conditions are matched and the experiments of astrophysical interest performed. In here, beneath the Gran Sasso mountain in Italy, both the $^{12}C(p,\gamma)^{13}N$ and $^{13}C(p,\gamma)^{14}N$ measurement were performed. The underground environment resulted in a significant reduction in cosmic background. In addition, the laboratory utilizes the LUNA 400 kV accelerator which maintains a stable beam for extended periods with an incredibly low energy spread. These combined factors provide an exceptional opportunity to obtain highly precise measurements of reaction cross sections at extremely low energies.

In this chapter the experiments performed at LUNA will be described. The experimental setups used for the $^{12}C(p,\gamma)^{13}N$ and $^{13}C(p,\gamma)^{14}N$ reaction study will be illustrated and all the analysis steps for both experimental campaigns will be thoroughly explained.

2.1 The LUNA Facility

The LUNA experiment is located in the underground laboratory at Laboratori Nazionali del Gran Sasso (LNGS) in Italy, situated in the heart of the Gran Sasso mountain. As the rock thickness is approximately 1400 m [30], the muon flux, built up from cosmic radiation interacting with the upper atmosphere, is substantially reduced by a factor of 10^6 compared to the Earth's surface [30]. Additionally to the natural shielding, a Pb castle of different thicknesses is usually built around the detectors in order to decrease the background from the radioactivity of the surrounding rocks. In fact, the γ-peaks that are present below 3 MeV comes from radioactive nuclei that are naturally present in the environment. In Figure 2.1 the HPGe background spectra acquired both on the surface and at the LUNA experiment are compared. As can be seen, the background reduction is particularly important for the region above the 3 MeV where about 5 orders of magnitude reduction in the γ-spectrum is achieved. For what regards the region below 3 MeV, the environmental γ-background can be easily reduced by adapting the Pb shield thicknesses basing on the necessities of each experiment, i.e. depending on where the γ-rays of interest are expected to appear.

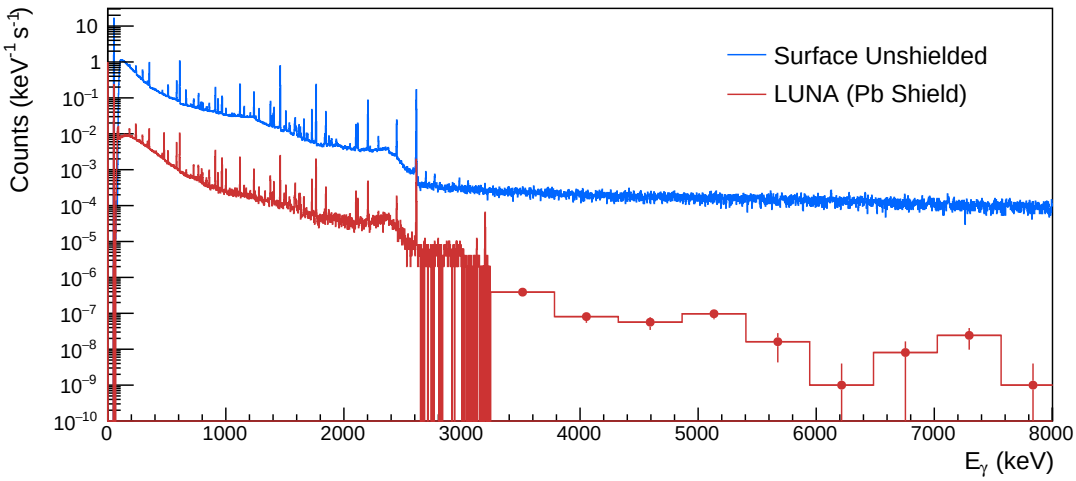

Figure 2.1: The comparison of HPGe spectra taken both on the surface and at the LUNA experiment. The Pb shield (15 cm) reduces the environmental background coming from the surrounding rocks. The muon flux (above 2.5 MeV), instead, is reduced by the Gran Sasso mountain.

The LUNA 400 kV accelerator, mounted in the LNGS tunnels, can accurately deliver protons and alpha particles with energies ranging from 50 to 400 keV,

with a beam stability of ± 2 eV in an hour and an energy spread of 100 eV [31]. Typical beam currents on target at LUNA are between $100-400$ μA. Two separate beamlines exist at the LUNA facility for various experiments, with one line devoted to solid targets experiments and the other containing a windowless gas target system.

2.2 Experimental Setup

The study of both the reactions involved the use of two different detector setups located on the same beamline. The latter consists of several water-cooled collimators, a quadruple magnet, steerer magnets and a bending magnets 2.2. All these were used to drive and optimize the beam that impinged on the targets and to avoid the stray beam hitting other parts of the target holder besides the active target surface. The targets, which will be described in more detail in the following sections, usually consisted in 0.4 mm thick Ta disks with the element of interest evaporated on top of it.

When the beam was stopped in the target, its power dissipated in the target material with heating power ranging between $10-100$ W, corresponding to currents of a few hundred μA and energies of a few hundred keV. Due to the concentration of this power on a relatively small area, active cooling was necessary to prevent excessive heating of the target. High temperatures can lead to the deterioration of the target through evaporation or diffusion of the active material. To mitigate this risk, the target holder was designed in a way to permit the water flow on the backside of the Ta disk.

The target chamber, on which the target holder was screwed, was electrically isolated from the beamline thus acting like a Faraday cup. This allowed for the direct measurement of the number of impinging protons per unit time as an electric current. The ORTEC Model 439 Digital Current Integrator was utilized to convert the accumulated charge into a series of pulses, with each pulse representing a fixed amount of collected charge.

One factor that could lead to a systematic error in the determination of the intensity of impinging protons by current measurements is the emission of electrons from the target due to the interaction of the proton beam with the target material. If these secondary electrons are not collected, the measured current would be larger than that corresponding to the flux of protons, resulting in overestimated accumulated charges and underestimated yields. To address this issue, a copper

tube was placed inside the beamline, separated from both the target chamber and other parts of the beamline. The tube was positioned very close to the front of the target, and a potential of $-300\,\mathrm{V}$ was applied to deflect electrons emitted from the target back onto it. This system is known as secondary electron suppression.

Another potential source of distortion in the current reading on the target could be the protons from the beam hitting the tube of the secondary electron suppression. This effect was taken care of by monitoring the power source connected to the tube to detect if any part of the beam impinged on the tube.

The copper tube also had a secondary function. It was in thermal contact with a bath of liquid nitrogen and functioned as a cold trap to capture organic vapors in the beamline volume. This prevented the deposition of contaminants on the target surface. The additional material deposited in front of the active target, in fact, would cause energy loss of the protons before they reach the active layer and consequently, building up over time, the energies observed in the active layer would change. This type of build up can usually be easily checked after the beam irradiation by looking at the energy position of well-known narrow resonances.

Finally, in Fig. 2.2 a simplified scheme of the solid target beamline is shown. The detection setup, located at the end of the beamline are not shown and will be discussed in the following sections.

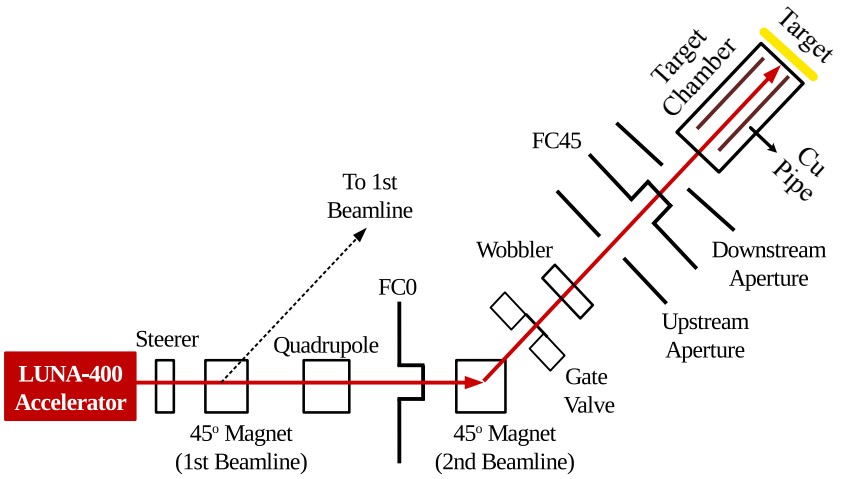

Figure 2.2: A simplified scheme of the solid target setup. Several magnetic appliances are present to drive the beam directly to the target.

2.2.1 Targets

During the experiments two different types of targets were used. The evaporated ones, made by evaporating respectively the ^{12}C and ^{13}C powders, provided by Sigma Aldrich with chemical purities of 99.9 % and respective isotopic purities of 99 %, on 0.4 mm thick Ta backings and 6 mm thick natural graphite disks. The usage of a heavy metal as the backing permits to avoid any possible background reaction on it due to the much higher Coulomb barrier. Before the evaporation, the Ta backing were chemically cleaned to reduce as much as possible the presence of contaminants, as oxygen and fluorine, that could generate unwanted background in the γ-spectra. The thick targets, instead, were used for normalization cross checks and for the $^{12}C(p,\gamma)^{13}N$ measurements with the BGO detector. In Figure 2.3 - 2.4 pictures is shown of the two types of targets mounted on the target holder.

Figure 2.3: The picture of the evaporated ^{12}C target on the Ta disk mounted on the target holder.

Figure 2.4: The picture of the graphite disk mounted on the target holder. The disk is placed on a blank Ta disk of the same thickness as in the evaporated target case.

The evaporated targets were prepared and characterized at the ATOMKI facility and were used for most of the measurements. The evaporation procedure was the same one used for the target production of the recent $^{13}C(\alpha,n)^{16}O$ experiment [32]. The thickness of all the evaporated targets lied in the 7 – 18 keV range at proton beam energy of 380 keV. The graphite disk, instead, was thick enough to entirely stop the beam. After the irradiation at LUNA, the evaporated targets were charactarized at ATOMKI both on the beamspot and off the beamspot through the Nuclear Resonant Reaction Analysis (NRRA) by exploiting the 1.7 MeV resonance in the $^{13}C(p,\gamma)^{14}N$ reaction [28].

2.3 HPGe Campaign

The first measurement of both the $^{12}C(p,\gamma)^{13}N$ and $^{13}C(p,\gamma)^{14}N$ was conducted with the use of the high-purity germanium (HPGe) detector in close geometry. The detector efficiency was obtained by using the radioactive sources and the resonant proton capture reactions on both ^{27}Al and ^{14}N targets. In total, four different evaporated ^{12}C targets, three evaporated ^{13}C and an infinitely thick ^{nat}C (graphite) target were used, described in Section 2.2.1.

The high energy resolution of the HPGe detector permitted to carefully study the branchings of both the reactions. Additionally, it allowed to use the so-called Peak Shape Analysis to retrieve both the S-factor and the target information directly from the primary γ-peak.

In the following, the analysis procedure will be explained. First, the efficiency of the HPGe detector will be described. Then the Peak Shape Analysis that was used to extract the cross section information will be discussed and explained. Finally, the additional cross-check for the target composition and the angular distributions will be shown.

2.3.1 HPGe Detection Setup

In Figure 2.5 the scheme of the detection setup is shown, which allowed placing one HPGe detector either at 0° or 55° from the beam axis. The 55° angle was selected to minimize the potential influence of angular distribtuion of γ-ray emission with respect to the beam axis, as the Legendre polynomial P_2 vanishes for $\cos^2(\theta) = 1/3$ and was mainly used to cross check the angular distribution. Additionally, to enhance the detection efficiency for γ-rays resulting from reactions in the target in the 0° configuration, the detector was placed in close proximity to the target, at a distance of approximately 5 mm from the back of the target holder (or about 1.4 cm from the beam spot). In order to reduce the environmental background, the detector was shielded with 15 cm of lead mounted on rails to create a quick access to the target as necessary for the frequent target exchange. The lead shielding was able to reduce the environmental background by two orders of magnitude (as can be seen in Fig. 2.1).

The high voltage of 4900 V was supplied by the CAEN N1471HET module. The signal from the preamplifier integrated into the detector was amplified by an ORTEC Model 671 spectroscopic amplifier before being fed into an ORTEC ASPEC-

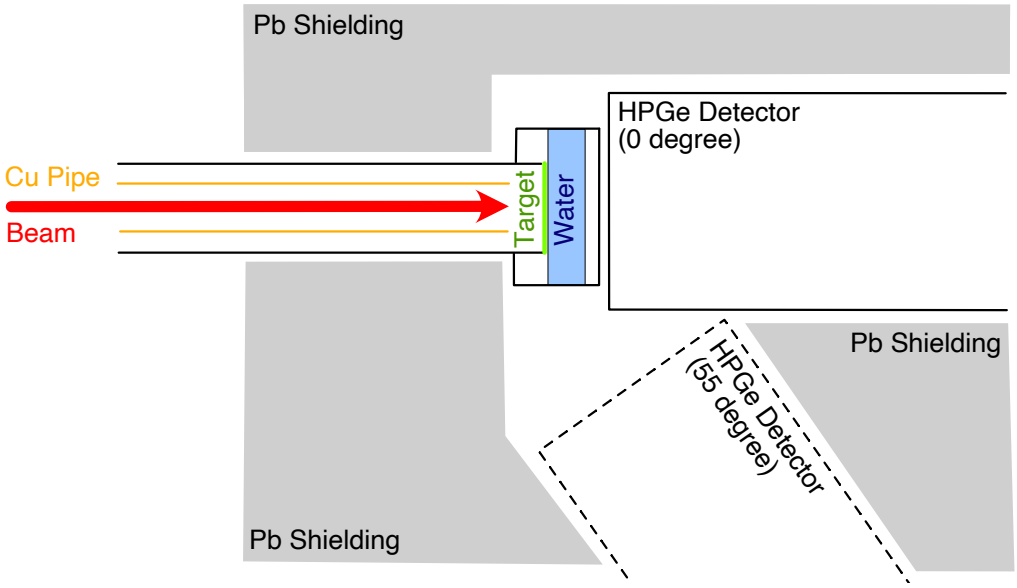

Figure 2.5: The scheme of the HPGe detection setup both in 0° and 55° configuration. When the HPGe was used at 0°, the 55° was closed with a lead block.

927 Multi-Channel Analyzer (MCA). The MCA had a second input connected to a pulse generator that was triggered by the signal of the current integrator. This allowed the charge on the target to be recorded together with the γ-ray spectrum, as an event in the second MCA channel corresponded to a fixed amount of charge on the target.

The ORTEC MAESTRO software was used to acquired the spectra. The data saved included the count of the binned spectrum, live time, and real time. Live time is the duration in which the acquisition could detect events, i.e. when the acquisition was not in busy state, while real time is the actual time passed between the start and the stop of the acquisition. Dead time, i.e. time period during which the acquisition system could not register any event, was calculated as the difference between the two aforementioned quantities. Intermediate spectra were saved at fixed time intervals during long runs to obtain information on the spectrum's evolution during the measurement.

2.3.2 Efficiency

The absolute full-energy peak efficiency, $\eta_{ph}(E_i)$, for a mono-cromatic γ-ray source of an energy E_i, such as ^{137}Cs, is defined as the number of observed events in the observed γ-peak, $N(E_i)$, and the amount of emitted γ-rays. The latter can be

obtained from the activity, A, of the radioactive source. Hence:

$$\eta_{ph}(E_i) = \frac{N(E_i)}{b_i A \Delta T} \tag{2.1}$$

where ΔT is the acquisition time and b_i is the branching of the observed γ-ray. Ideally, by using this formula it is possible to calibrate the detector efficiency by using radioactive sources that emits γ-rays at different energies.

Unfortunately only few sources are mono-energetic. Usually one decay is followed by the emission of several γ-rays in cascade, e.g. in ^{60}Co case which decay scheme is shown in Fig. 2.6. In addition, it is possible that more than one excited state of the daughter nuclei is populated, which further complicates the efficiency extraction, e.g. in the ^{133}Ba case illustrated in Fig. 2.7. When more than one γ-ray is emitted in coincidence with an another one, or more precisely in a time window lower than the timing resolution of a given detector (for an HPGe we are talking about ~ 200 ns), it is possible that two or more γ-rays are indistinguishably seen as one. This give rise to two different well-know effects called coincidence summing in and summing out [33].

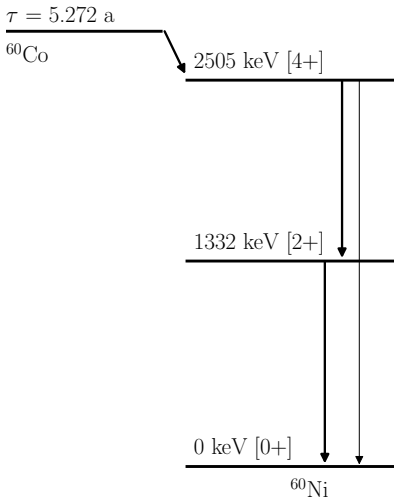

Figure 2.6: ^{60}Co decay scheme.

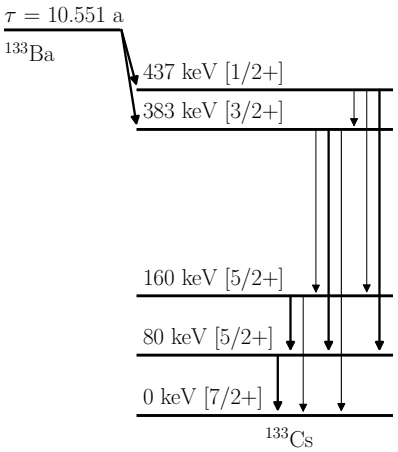

Figure 2.7: ^{133}Ba decay scheme.

These two effects are proportional to the solid angle covered by the detector, thus they highly depend on the distance from the γ-ray source. At close distances both the summing out and summing in can have a large impact on the observed full-

energy γ-peak. On the contrary, if the detector is far, and thus its solid angle is small, the two can be completely neglected.

In order to deal with both the effects it is necessary to parametrise all the γ-rays adequately. Let's take as an example the ^{60}Co. In this case $\sim$ 99.9 % of the decays occurs through a γ-cascade where two γ-rays are emitted, $E_{\gamma,1}$ and $E_{\gamma,2}$. Since the summing out can remove some counts from the γ-peak because of a non-null probability of observing a fingerprint of the second γ-ray in coincidence, it is possible to write the following:

$$N(E_{\gamma,1}) = N_{\text{decays}} b_1 \eta_{ph}\,(E_{\gamma,1})(1 - b_2 \eta_{tot}(E_{\gamma,2})) \tag{2.2}$$

$$N(E_{\gamma,2}) = N_{\text{decays}} b_1 b_2 \eta_{ph}\,(E_{\gamma,2})(1 - \eta_{tot}(E_{\gamma,1})) \tag{2.3}$$

where $N(E_{\gamma,i})$ is the expected number of observed γ-rays, N_{decays} is the calculated number of decays of the ^{60}Co source and $\eta_{tot}(E_{\gamma,i})$ is the total efficiency of the detector for a given γ-ray, i.e. the probability to see the γ-ray anywhere in the spectrum. The position of the branching parameters, b_i, depends on whether the γ-ray of interest is emitted before or after the other one.

Let's now consider the remaining $\sim$ 0.01 % of the ^{60}Co decays, which occurs through a single γ-ray, $E_{\gamma,3}$. In reality those are hardly observed given the very low branching, but the example is only for instructive purpose. In this case the equation becomes:

$$N(E_{\gamma,3}) = N_{\text{decays}}\,(b_3 \eta_{ph}(E_{\gamma,3}) + b_1 b_2 \eta_{ph}(E_{\gamma,1}) \eta_{ph}(E_{\gamma,2})) \tag{2.4}$$

where the new factor describes the possibility of observing the two γ-rays depositing the full-energy in coincidence, thus contributing to the observed counts through the summing in. No summing out is expected in this case.

The procedure can be generalized to a case where the decays occurs through several γ-rays and where many different cascades can contribute in generating the γ-ray of interest:

$$\begin{aligned} N(E_{\gamma,k}) =& N_{\text{decays}} \sum_{i=0}^{N_1} \prod_{j}^{k} b_{ij} \eta_{ph}(E_{\gamma,k}) \\ & \times \left[\left(1 - \sum_{l=0}^{k} \prod_{l}^{k} \eta_{tot}(E_{\gamma,l}) - \sum_{l=k+1}^{n_1} \prod_{l}^{n_1} b_l \eta_{tot}(E_{\gamma,l}) \right) \right. \\ & \left. + \sum_{l=0}^{N_2} \prod_{h}^{n_2} b_h \eta_{tot}(E_{\gamma,h}) \right]_i \end{aligned} \tag{2.5}$$

where k is the index of the γ-ray of interest in a given i-th cascade, n_1 is the index of the last decay, i.e. to the ground state, n_2 is the index of the decay to state that γ-ray of interest decays to, and N_1 and N_2 are the numbers of, respectively, decays cascades that produces the γ-ray of interest and cascades that can create summing in. The first summation is due to different cascades that can generate the γ-ray of interest, the two summations inside the brackets takes into account the summing out of the γ-rays produced respectively before and after the γ-ray of interest, whereas the last term describes the summing in contribution.

One last problem to address is the fact that radioactive sources are not enough to describe the detector efficiency in a wide energy range. Most of these are not able to produce γ-rays with energies higher than 3 MeV. Thus, in order to get the efficiency information in higher energy regions it is necessary to use nuclear reaction resonances, e.g. $^{27}\mathrm{Al}(p,\gamma)^{28}\mathrm{Si}$ ones, that populate high lying excited states. These usually permit to extend the efficiency calibration up to 10 MeV. In case of resonances the N_{decays} is substituted by the rate of the resonance, R, which describes the strength of the resonance and thus depends on its $\omega\gamma$. Nevertheless, the precise dependence can be neglected for the purpose of this work and it can be treated as free parameter. This is due to the fact that the selected nuclear resonances emit both low energy and high energy γ-rays in cascade, where the former energy range is very well constrained by the radioactive sources. By treating R as a free parameter we are indirectly using not the absolute yields of the γ-rays but their ratio, i.e. how many high energy γ-rays are observed with respect to the lower lying ones in the same γ-cascade.

Multiparametric Fit In order to address all of the aforementioned issues, several different radioactive sources and resonances were used at LUNA: ^{60}Co, ^{137}Cs, $^{27}\mathrm{Al}(p,\gamma)^{28}\mathrm{Si}$ resonances at 223 keV and 327 keV [34] and $^{14}\mathrm{N}(p,\gamma)^{15}\mathrm{O}$ resonance at 278 keV [35]. The spectra were acquired at four different distances: 1.45 cm, 6.45 cm, 11.45 cm and $\sim$ 16.45 cm. Additionally, in order to test the reproducibility of the efficiency calibration the data were taken both before and after the measurements.

To extract the efficiency curve for the HPGe detector, a multiparametric fit was performed. The following parametrizations were used to describe the full-energy and total efficiencies as a function of the detector position d and the γ-ray en-

ergy [35]:

$$\eta_{ph}(d, E_\gamma) = D(d, E_\gamma) \exp\left[a + b\ln(E_\gamma) + c\ln^2(E_\gamma)\right] \tag{2.6}$$

$$\ln\left(\frac{\eta_{ph}}{\eta_{tot}}\right) = k_1 + k_2\ln(E_\gamma) + k_3\ln^2(E_\gamma) \tag{2.7}$$

where a, b, c, k_1, k_2 and k_3 are free parameters, and D is a function of distance, d, that describes the detector response in function of the solid angle:

$$D(d, E_\gamma) = \frac{1 - \exp\left(-\frac{d+d_0}{d_1+d_2\sqrt{E_\gamma}}\right)}{(d+d_0)^2} \tag{2.8}$$

where d_0, d_1 and d_2 are free parameters.

The rates of the resonances, R_i, were left free to vary in the fitting procedure. The activities of the radioactive sources, A_i, were instead treated as nuisance parameters since their values are affected by a 1 % uncertainty. In case of the ^{60}Co and ^{14}N$(p,\gamma)^{15}$O angular correlations were taken into account by calculating the attenuation coefficients [36], needed to account for the finite angle covered by the detector. On the contrary, for the ^{27}Al resonances it was not possible to apply the corrections since the coefficients of the Legandre polynomial are not present in literature.

Finally, the Equation 2.5 was used to calculate the expected counts in each γ-peak at every distance. The χ^2 value was then calculated where both the statistical and the model errors were included. The model uncertainty was calculated by using the literature uncertainties on the branchings for each γ-decay. Finally, it was possible to minimize the χ^2 and obtain the best-fit values for the parameters. The final full-energy efficiency and the residues can be seen in Fig. 2.8. The best fit parameters are reported in Table 2.1.

d_0	2.0 ± 0.2	k_1	-1.47 ± 0.09
d_1	5.4 ± 0.4	k_2	-0.6 ± 0.2
d_2	0.1 ± 0.05	k_3	-0.1 ± 0.08
a	0.08 ± 0.01	$R(^{14}$N - 274 keV)	41.6 ± 0.6
b	-0.57 ± 0.02	$R(^{27}$Al - 223 keV)	0.39 ± 0.01
c	-0.103 ± 0.009	$R(^{27}$Al - 327 keV)	13.0 ± 0.3

Table 2.1: Best-fit parameters and their errors obtained from the chi-squared minimization

In order to obtain an estimate of the efficiency uncertainty at each energy, a Monte Carlo approach was followed. First a multivariate normal distribution was created

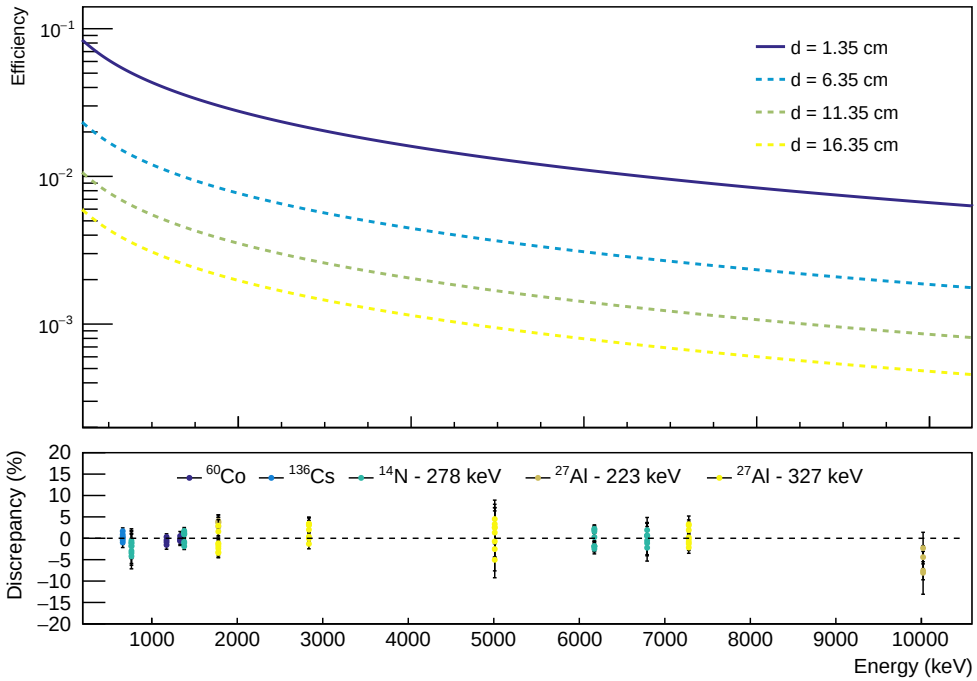

Figure 2.8: (Upper panel) The efficiencies for the best-fit parameters at different distances. (Lower panel) Best fit residues for the multiparametric minimization for all the distances.

from the covariance matrix of the parameters. Then it was sampled 10000 times and 1σ confidence interval could be derived. The result of the parameter sampling is showed in Fig. 2.9. In the region of interest for this study, between 2 MeV and 8 MeV, the efficiency uncertainty ranges from 2 % to 3%.

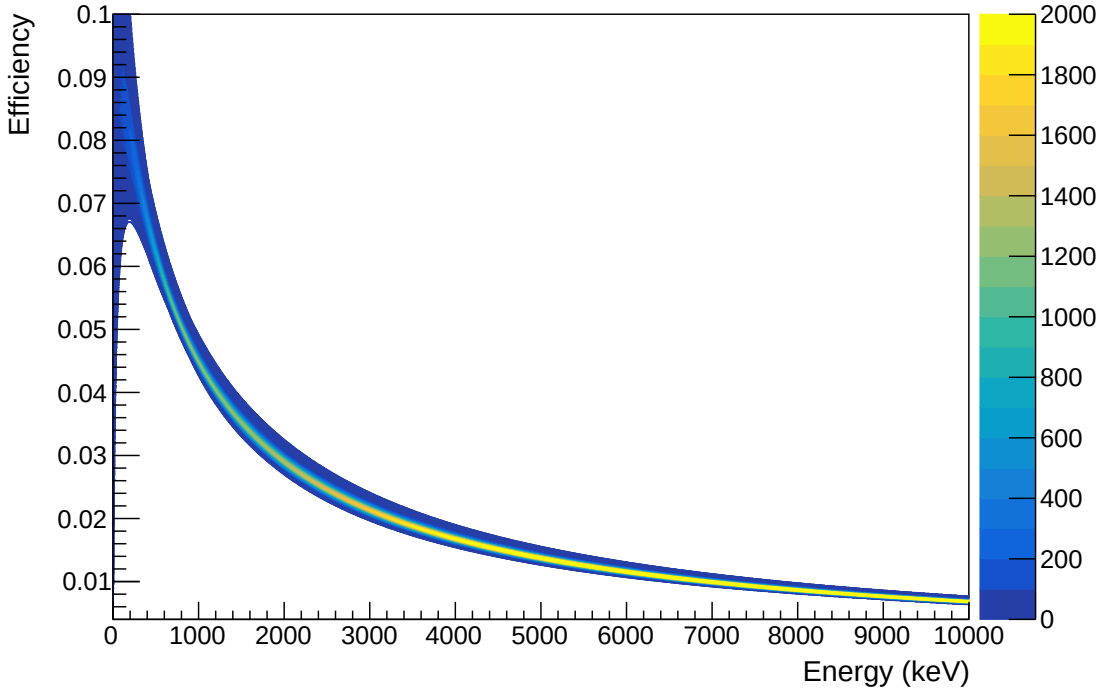

Figure 2.9: The result of the Monte Carlo sampling of the best-fit parameters used to extract 1σ region for uncertainty estimation.

2.3.3 Peak Shape Analysis

Once the detector efficiency was calibrated, the data acquired by irradiating the evaporated targets with proton beam were analyzed in order to extract the cross section. Since it was not possible to perform the target scans, e.g. with the NRRA technique, and thus to obtain the target information during the irradiation, the analysis procedure relied on the so called Peak Shape Analysis [1], that will be described in the following.

If we consider a direct capture process of a proton with a subsequent primary γ-ray emission, an infinitesimal yield, dY, inside an infinitesimal thickness of the target, dE, depends on the cross section of the reaction, $\sigma(E_p)$, at the energy of the beam,

E_p, inside the infinitesimal slice of the target, as follows from Equation 1.6. Since the protons loss their energy while travelling through the target, the contribution of the deeper parts will be lower than that of the initial layers following the exponential drop of the cross section, thus affecting the shape of the observed γ-peak. The width of the γ-peak, instead, will depend on the target thickness, i.e. how much energy the beam has lost inside it. The thicker the target, the wider the primary γ-peak will be. These concepts can be easily visualized in Fig. 2.10. Since the shape of the γ-peak depends on the aforementioned quantities, it is possible to extract them by parametrizing the γ-peak and fit it against the data.

Given the primary γ-peak for either $^{12}\mathrm{C}(\mathrm{p},\gamma)^{13}\mathrm{N}$ or $^{13}\mathrm{C}(\mathrm{p},\gamma)^{14}\mathrm{N}$ reaction, it is always possible to make a transformation from its energy, E_γ, to the corresponding proton energy (in CM frame) at which the reaction took place, $E_{\mathrm{c.m.}}$, by using the following relation:

$$E_\gamma = Q + E_{\mathrm{c.m.}} - \Delta E_{\mathrm{Rec}} + \Delta E_{\mathrm{Dopp}} \tag{2.9}$$

where Q is the Q-value of the reaction, ΔE_{Rec} is the correction for the recoil effect of the $^{13,14}\mathrm{N}$ compound nucleus and ΔE_{Dopp} is the correction for the Doppler effect. The last two terms are defined as [1]:

$$\Delta E_{\mathrm{Rec}} = \frac{E_\gamma^2}{2M_{^{13,14}\mathrm{N}}c^2} \tag{2.10}$$

$$\Delta E_{\mathrm{Dopp}} = \frac{v}{c} E_\gamma \cos\theta \tag{2.11}$$

where c is the speed of light, v is the compound nucleus velocity and θ is the angle between the beam direction and the γ-ray detector.

By differentiating Equation 2.9 we obtain that:

$$dE_\gamma = dE_p \tag{2.12}$$

where the correction terms are negligible. By using this equivalence and Equation 2.9 it is possible to work directly in the E_γ domain. Using the following definition of the experimental yield [1]:

$$Y_i = \frac{N_i}{N_p \eta(E_\gamma) W(\theta, E_p)} \tag{2.13}$$

where N_i is the number of counts inside each i-th bin, $\eta(E_\gamma)$ is the full-energy efficiency of the detector, N_p is the number of incoming protons and $W(\theta, E_p)$ is the angular distribution factor.

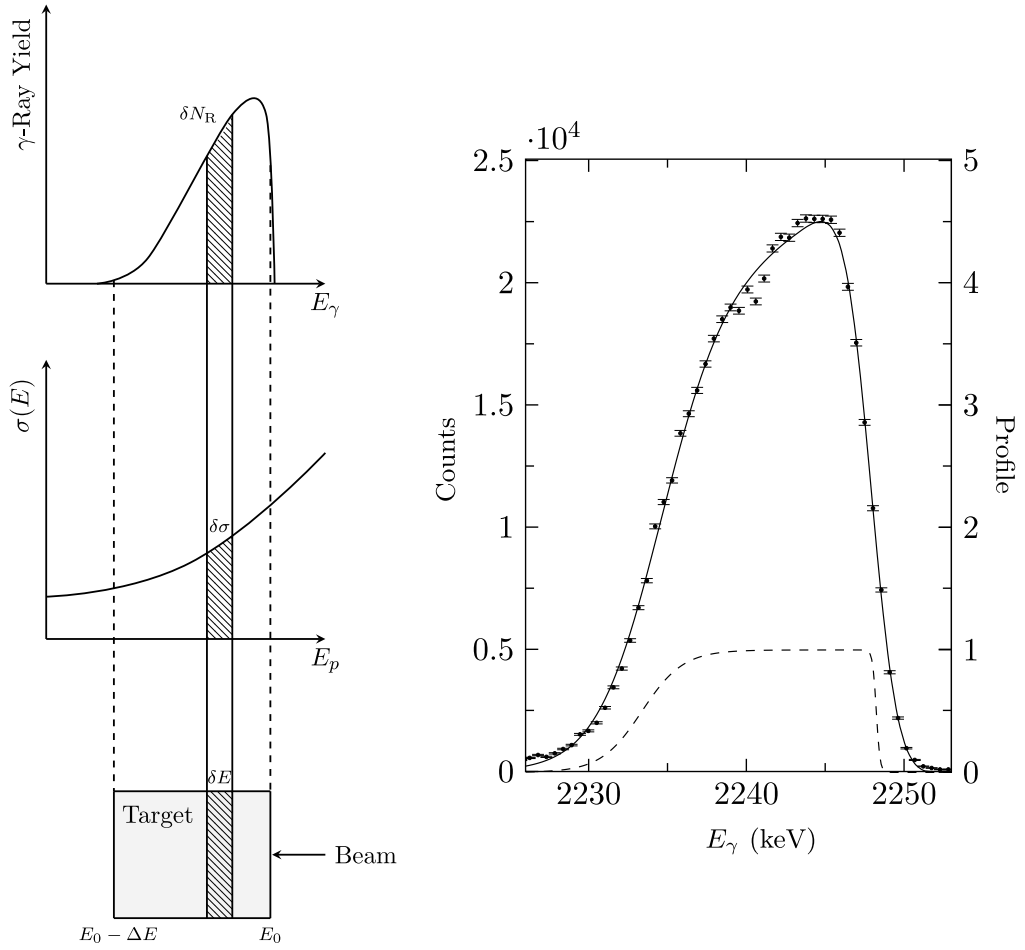

Figure 2.10: Left: The peak shape of the γ-ray emitted reflects the cross section dependence on energy as the beam loses energy inside the target. The number of counts, δN_R, corresponding to a thin slice of the target of width, δE, is proportional to the integral of the cross section. Right: Example of the γ-ray peak from the study of the $^{12}C(p,\gamma)^{13}N$ reaction. The dashed line represents the target profile.

By combining the Equation 2.13 with Equation 1.6, and substituting the infinitesimal dE_γ with the discretized ΔE_γ given by the binning of the γ-spectrum, it is possible to obtain the following relation:

$$N_i = \frac{\sigma(E_{p,i})}{\epsilon_{\text{eff}}(E_{p,i})}\eta_{ph}(E_{\gamma,i})W(\theta, E_p)N_p\Delta E_{\gamma,i} \tag{2.14}$$

Up to now, the thickness of the target, ΔE, which is the integration range of the Equation 1.6 was omitted. The target profile can be modelled by the use of two Fermi functions as follows [32]:

$$P(E_p) = \Big[\exp\Big(\frac{E_p - E_0}{\Gamma_1}\Big) + 1\Big]^{-1}\Big[\exp\Big(\frac{E_0 - E_p - \Delta E}{\Gamma_2}\Big) + 1\Big]^{-1} \tag{2.15}$$

where E_0 is the incident beam energy, ΔE is the target thickness, and Γ_1 and Γ_2 are two parameters accounting, respectively, for the slopes of the falling and leading edges of the target profile. By introducing it to the Equation 1.6 it is possible to extend the integral to infinity, i.e. the integral domain information is handled by the target profile itself. By doing this, the $P(E)$ can be added to the model as a multiplicative factor:

$$N_i = P(E_{p,i})\frac{\sigma(E_{p,i})}{\epsilon_{\text{eff}}(E_{p,i})}\eta_{ph}(E_{\gamma,i})W(\theta, E_p)N_p\Delta E_{\gamma,i} \tag{2.16}$$

In order to describe the real γ-ray peak, several other crucial ingredients are missing, such as the detector response, the Doppler broadening and the beam straggling inside the target. All these points will be thoroughly discussed in the following sections.

HPGe Detector Resolution

The resolution of the HPGe detector, i.e. its response function, can be parameterized as a Gaussian distribution, $\mathcal{N}(E_\gamma, \sigma_{\text{HPGe}}(E_\gamma))$, with a given width, $\sigma_{\text{HPGe}}(E_\gamma)$. Unfortunately, it can not be calculated a priori, i.e. from the detector data sheet, or at least it will not precisely corresponds to that value due to the aging of the detector itself. Hence, in order to calibrate the detector resolution, the γ-peaks from the radioactive sources were analyzed. In Tab. 2.2 all the used γ-peaks are listed. It was not possible to use the nuclear reaction resonances, as the $^{14}\text{N}(\text{p},\gamma)^{15}\text{O}$ one, due to the Doppler effect: when the γ-ray is emitted, the excited nucleus is still moving through the target, thus the width of the γ-peak will be broadened and thus can not be used for the resolution calibration.

In order to extend the resolution to higher energies, the data were fitted with the following formula [33]:

$$\sigma_{\mathrm{HPGe}} = \sqrt{a + b \times E_\gamma} \tag{2.17}$$

where a and b are the only free parameters of the fit.

After finding the best fit parameters, the covariance matrix was obtained and 3σ intervals were calculated for each energy. The results are shown in Fig. 2.11.

Source	γ-rays (keV)
^{60}Co	1173.240 ± 0.003
	1332.508 ± 0.004
^{88}Y	898.05 ± 0.01
	1836.090 ± 0.008
^{137}Cs	661.659 ± 0.003

Table 2.2: List of all the γ-rays used for the resolution calibration.

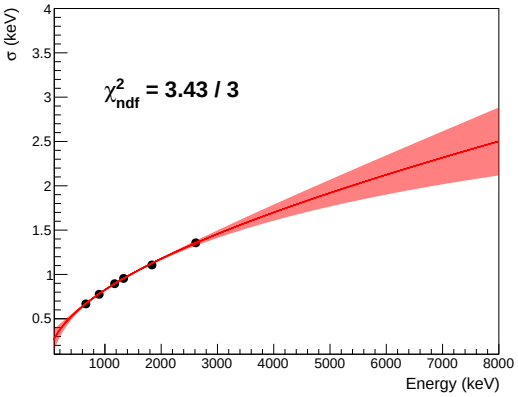

Figure 2.11: The result of the minimization for the σ_{HPGe}. The red area represents the 3σ confidence interval.

The 3σ interval was then used for the Peak Shape Analysis as the upper and lower bounds in which the $\sigma_{\mathrm{HPGe}}(E_\gamma)$ parameter could vary. As can be seen from the plot, at energies close to 2 MeV, near the region of interest of the $^{12}\mathrm{C}(\mathrm{p},\gamma)^{13}\mathrm{N}$ reaction, the detector resolution is well known and its value is close to 1 keV, thus not affecting very much the primary γ-peak shape. Whereas, in the case of the $^{13}\mathrm{C}(\mathrm{p},\gamma)^{14}\mathrm{N}$ reaction which emits γ-rays up to 8 MeV we expect that the primary γ-peak will be looking more like a Gaussian respect to the other reaction. An example of this can be seen in Fig. 2.12 and in Fig 2.13, where two different detector responses were applied.

Doppler Broadening

The Doppler shift can be calculated as follows [1]:

$$\Delta E_{\mathrm{Dopp}}(E_\gamma, E_p, \theta) = 4.63367 \times 10^{-2} \frac{\sqrt{M_p E_p}}{M_0} E_\gamma \cos\theta \tag{2.18}$$

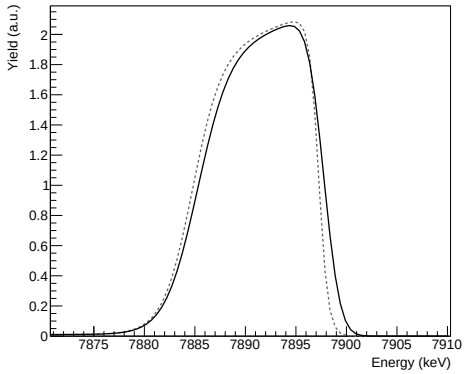

Figure 2.12: An example of the Gaussian peak convolution of the γ-peak yield calculated with Equation 2.16 with $\sigma_{\mathrm{HPGe}} = 1$ keV. This is a typical resolution for the γ-peak of the $^{12}\mathrm{C}(\mathrm{p},\gamma)^{13}\mathrm{N}$ reaction.

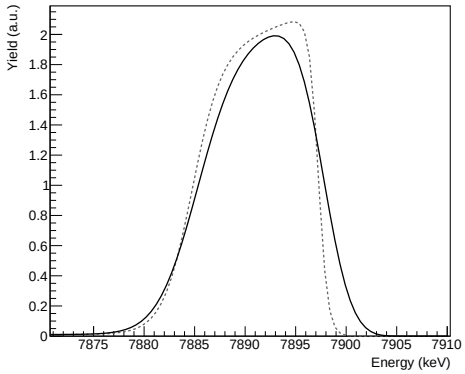

Figure 2.13: An example of the peak convolution of the γ-peak yield calculated with Equation 2.16 with $\sigma_{\mathrm{HPGe}} = 2$ keV. This is a typical resolution for the main γ-peak of the $^{13}\mathrm{C}(\mathrm{p},\gamma)^{14}\mathrm{N}$ reaction.

where M_0 is the mass of the recoil nucleus and θ is the emission angle of the γ-ray respect to the nucleus trajectory. The Doppler term depends both on the proton and the γ-ray energies, whereas the intrinsic detector resolution depends only on the latter.

Ideally, it would be possible to analytically calculate the Doppler contribution to the γ-peak by averaging it over the detector geometry. Nevertheless, the knowledge of the detection efficiency in function of the γ-ray emission angle would be needed which is not something that can be easily measured. To overcome this problem and study the impact of this effect on the shape of the primary γ-peak, the Monte Carlo method was preferred. Both the $^{12}\mathrm{C}$ and $^{13}\mathrm{C}$ primary γ-rays were simulated within the Geant4 framework [37] by assuming a mono-energetic γ-ray. The HPGe detector was put along the 0° axis with respect to the beam. The emission angle was considered isotropic, thus sampled from a uniform distribution. Once the emission direction was drawn, the energy of the γ-ray was calculated according to Equation 2.18.

The result in case of the $^{13}\mathrm{C}(p,\gamma)^{14}\mathrm{N}$ transition to the ground state is shown in Fig. 2.14. As can be seen, the Doppler has an important effect on the energies of the γ-ray seen by the HPGe detector by shifting the energies towards lower values. In order to obtain a description of this effect, that can be introduced in the Peak Shape Analysis fit, the following skewed normal distribution was used to

fit simulated spectrum:

$$f_{\text{broad}}(E_\gamma, \sigma_{\text{Dopp}}, \alpha) = \mathcal{N}(E_\gamma, \sigma_{\text{Dopp}}) \times \Phi(\alpha E_\gamma, \sigma_{\text{Dopp}}) \tag{2.19}$$

$$\tag{2.20}$$

where $\Phi(\alpha E_\gamma, \sigma_{\text{Dopp}})$ is the cumulative distribution function of $\mathcal{N}(E_\gamma, \sigma_{\text{Dopp}})$, with the α parameter that governs the skewness of the total distribution. The best fit values for both the σ_{Dopp} and α were used in order to convolve the modelled primary γ-peaks with the skewed normal distribution. An example of the convolution can be seen in Fig. 2.15. The same procedure was followed in case of the other primary γ-rays and in the case of the $^{12}\text{C(p,}\gamma)^{13}\text{N}$ reaction, where similar skewness parameters were obtained but with lower σ_{Dopp}, accordingly to the Doppler effect dependence on the energy of the γ-ray.

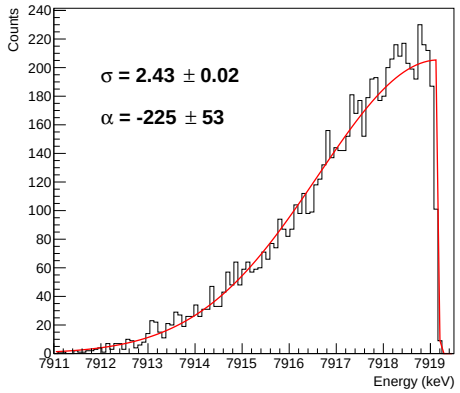

Figure 2.14: The γ-peak from the ground state transition of the $^{13}\text{C}(p,\gamma)^{14}\text{N}$ obtained from the Geant4 simulation of the HPGe detector. The Geant4 spectrum was not smeared with the detector resolution in order to highlight the effect of the Doppler broadening.

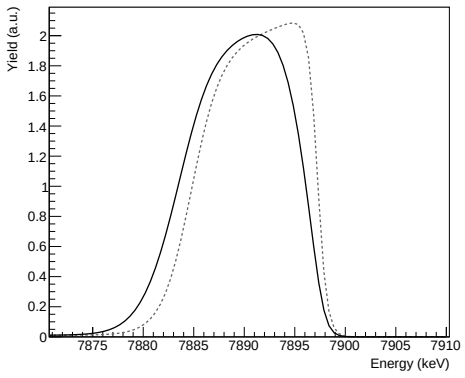

Figure 2.15: The effect of the Doppler broadening on the primary γ-peak to ground state of the $^{13}\text{C}(p,\gamma)^{14}\text{N}$. The dashed line is the γ-peak yield calculated with Equation 2.16 and the solid line is the convolution with the skewed normal distribution obtained from Geant4 simulation.

Beam Straggling

When the beam enters the target, it starts loosing energy and thus it widens its energy distribution because of the statistical nature of the energy loss. This effect is called the beam straggling and should be taken into account during the γ-peak parametrization since at each point of the target profile, protons with different energies can produce the γ-ray. An approximate solution for this is the convolution

of its profile by the mean of the following function [38]:

$$f_{\text{stragg}}(E_p, E_{\text{slowed}}(x)) = \exp\left[-\frac{(E_p - E_{\text{slowed}}(x))^2}{2\sigma^2_{\text{strag}}(E_{\text{slowed}}(x)) + 2\sigma^2_{\text{beam}}}\right] \tag{2.21}$$

where the $E_{\text{slowed}}(x)$ is the energy of the beam at a given position, x, inside the target, the σ_{beam} is the initial energy spread of the LUNA 400 kV accelerator ($\leq$ 0.1/2.355 keV), and $\sigma_{\text{strag}}(E_{\text{slowed}}(x))$ is the straggling contribution to the energy spread.

In order to use this equation, it is necessary to calculate the spread of the beam energy at a certain distance x inside the target, the $\sigma_{\text{strag}}(E_p)$ parameter. To achieve it, the Chu's theory of straggling was used where [39]:

$$\sigma^2_{\text{strag}}(E_p) = \sigma^2_{\text{Bohr}} H(E_p, Z_2) \tag{2.22}$$

$$\sigma^2_{\text{Bohr}} = 4\pi e^4 Z_1^2 Z_2 \Delta x \tag{2.23}$$

where Z_1 and Z_2 are the atomic numbers of, respectively, the projectile and the target, e is the fundamental charge and $H(E_p, Z_2)$ is the Chu correction to the Bohr formula for low-energy region.

The values of the correcting function, in case of the $^{12/13}$C target, were taken from SIMNRA [40], and are listed in Tab. 2.16. Furthermore, it is possible to interpolate $H(E)$ with [41]:

$$H(E) = aE^n \exp(-bE) + (1 - \exp(-cE)) \tag{2.24}$$

where a, b, c and n are free parameters. The resulting curve can be visualized in Fig. 2.17.

Once the energy spread, $\sigma_{\text{strag}}(E_p)$, has been calculated at each position, x, inside the target, it is possible to apply the convolution. However, since the calculated $\sigma^2_{\text{strag}}(E_p)$ values are of the order of 0.5 keV, which is approximately the width of each bin inside the γ-spectrum, the convolution has little effect on the γ-peak shape with respect to all the previous corrections. For this reason and due to the fact that the convolution with an energy dependant σ is computationally heavy, this effect was neglected in the Peak Shape Analysis.

Cross Section

Both the ^{12}C$(p,\gamma)^{13}$N and ^{13}C$(p,\gamma)^{14}$N reactions present a broad resonance at energies close to the measurement range at LUNA (at $E_{\text{cm}} = 424.2$ keV and $E_{\text{cm}} =$

Energy (keV)	$H(Z_2 = 6)$
10	0.16325
50	0.48162
100	0.667
200	0.824
300	0.858
400	0.881
500	0.899

Figure 2.16: Data for the Chu $H(E_p)$ function in case of the C nuclei.

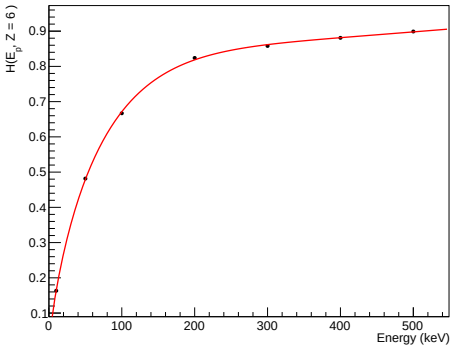

Figure 2.17: The result of the interpolation for the Chu $H(E_p)$ function.

517.8, respectively). Given the resonance widths, their tails strongly contribute to the reaction cross section at lower energies. Nevertheless, it is not possible distinguish between the resonant and direct capture contributions [1] from an experimental point of view.

This creates a major issue for the analysis since in the energy range spanned throughout the target the $S(E_p)$ is a strongly varying function. On the other side, the shape of the S-factor depends on several resonance parameters, which will be discussed in Sec. A. It is possible to use the literature values for the two broad resonances to decouple their contribution from the direct capture one. The latter can be then considered with a good approximation constant throughout the target. Hence, it is possible to write the cross-section as:

$$\sigma(E_p) = \sigma_{\mathrm{NR}}(E_p) + \sigma_{\mathrm{R}}(E_p) \tag{2.25}$$

where $\sigma_{\mathrm{NR}}(E_p)$ and $\sigma_{\mathrm{R}}(E_p)$ are, respectively, the direct capture and the resonant components. The latter can be parametrized by the use of the Breit-Wigner distribution [1]:

$$\sigma_{\mathrm{R}}(E_p) = \frac{\pi}{k^2}\frac{2J+1}{(2j_p+1)(2j_t+1)}\frac{\Gamma_p(E_p)\Gamma_r(E_p)}{(E_p - E_{\mathrm{R}})^2 + (\frac{\Gamma(E_p)}{2})^2} \tag{2.26}$$

where k is the wavenumber, J, j_p and j_t are, respectively, the spin of the resonance, the projectile and the target, $\Gamma_p(E_p)$ and $\Gamma_r(E_p)$ are the widths of the entrance and reaction channels, $\Gamma(E_p)$ is the total width of the resonance and E_R is the energy of the resonance in the CM.

	E_{R} (keV)	Γ (keV)	$\omega\gamma$ (eV)
$^{12}\mathrm{C}(p,\gamma)$	424.2	35	1.52
$^{13}\mathrm{C}(p,\gamma)$	517.8	40	8.8

Table 2.3: Resonance parameters used for both $^{12}\mathrm{C}(p,\gamma)^{13}\mathrm{N}$ [21] and $^{13}\mathrm{C}(p,\gamma)^{14}\mathrm{N}$ [27] reactions.

The parameters used for the resonance were taken from [20, 27] and shown in Tab. 2.3. Since the resonance parameters depends on the projectile energy, E_p, they had to be recalculated for each single proton energy. The wavenumber, k, was calculated as [1]:

$$k = 4.125 \times \left(\frac{M_0 + M_1}{M_1}\right)^2 \frac{10^6}{E_{p,\mathrm{Lab}} M_0} \tag{2.27}$$

where M_0 and M_1 are, respectively, the masses of the projectile and the target in amu, and $E_{p,\mathrm{Lab}}$ is the laboratory projectile energy in eV. The widths were then recalculated by using the following relations [1]:

$$P_l(E_p) = R\left(\frac{k}{F_l^2(\eta;\rho) + G_l^2(\eta;\rho)}\right)_{\rho=kR} \tag{2.28}$$

$$\Gamma = 2P_l(E_p)\gamma^2 \tag{2.29}$$

$$R = 1.2(A_p^{\frac{1}{3}} + A_t^{\frac{1}{3}}) \tag{2.30}$$

where $P_l(E_p)$ is the penetration factor, $F_l^2(\eta;\rho)$ and $G_l^2(\eta;\rho)$ are, respectively, the regular and irregular Coulomb functions, R is the radius of the compound nucleus, A_p, A_t, Z_1 and Z_2 are, respectively, the mass numbers and the charges of the projectile and the target and γ^2 is the reduced width of the resonance, which does not depend on the projectile energy and incorporates all the unknown properties of the nuclear interior. For the calculation, only the s-wave was included given the low energies of the projectile, i.e. only $l = 0$ contribution of the penetration factor was calculated.

Finally, once the resonant contribution was calculated for each proton energy it was therefore fixed and only the direct capture contribution was used as free parameter of the fit.

Minimization

It is possible to write the final model as follows:

$$N_i = \Big[\int_{-\infty}^{\infty} dE_\gamma \; \mathcal{N}(E_\gamma, \sigma_{\mathrm{HPGe}}(E_\gamma)) \times \tag{2.31}$$

$$\int_{-\infty}^{\infty} dE_\gamma \; f_{\mathrm{broad}}(E_\gamma, \sigma_{\mathrm{Dopp}}, \alpha) \times \tag{2.32}$$

$$\frac{\sigma(E_{p,i})}{\epsilon_{\mathrm{eff}}(E_{p,i})} \eta_{\mathrm{ph}}(E_{\gamma,i}) P(E_{p,i}) N_p \Delta E_{\gamma,i} \Big]_i \tag{2.33}$$

This is the final equation that models the shape of the γ-peaks from the primary γ-ray transitions. By fitting it to the experimental spectra acquired with the HPGe detector, it was then possible to extract both the cross section and the target profiles at different stages of the irradiation.

In order to perform the minimization, the MINUIT2 [42] library was used. The variable that was minimized is the negative logarithm of the Poissonian likelihood defined as:

$$\mathcal{L} = \prod_i \exp(\lambda_i) \frac{1}{N_i} \lambda_i^{N_i} \tag{2.34}$$

where λ_i are the calculated values according to Equation 2.33 and N_i are the observed counts in each i-th bin of the spectrum.

Analysis

During the data taking two different types of runs were performed: the long ones, which are used to extract the information about the cross section over a wide energy range, and the reference ones. The latter ones were carefully performed at the same energy ($E_p = 380$ keV) and were used to extract the information on the target profile at different accumulated beam charges, Q_{acc}. These were then used as the target profiles for the other runs by bounding their parameters in a 3σ region during the minimization. Since the $^{13}\mathrm{C}(p,\gamma)^{14}\mathrm{N}$ presents several primary transitions, the γ-peak fitted for the target profile extraction was the DC $\rightarrow gs$ being the one with the highest statistics. Additionally, in case of the $^{13}\mathrm{C}(p,\gamma)^{14}\mathrm{N}$, a two step target profile was assumed since most of the γ-peaks showed a tail on the low-energy side. An example of the reference run fits can be seen in Fig. 2.18 and in Fig. 2.19.

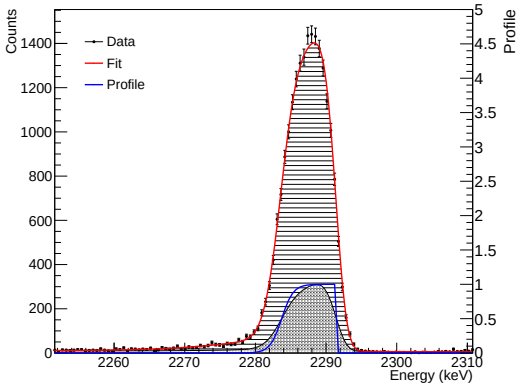

Figure 2.18: An example of the reference fit for the ^{12}C. The dotted and the dashed areas indicate, respectively, the resonant and the DC contributions. The blue line represents the target profile.

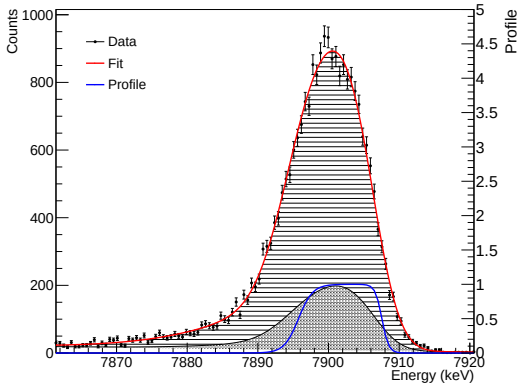

Figure 2.19: An example of the reference fit for the ^{13}C. The dotted and the dashed areas indicate, respectively, the resonant and the DC contributions. The blue line represents the target profile.

In order to account for the change in the target stoichiometry, a new parameter, $R_i \leq 1$, was introduced that governs the height of the profile. This change can be attributed to the presence of a contaminant nuclei inside the target, or e.g. due to the carbon layer diffusion inside the Ta backing. Since the precise identification of its origin is out of the scope of this work, it was enough to assume a fresh target at the beginning of the measurement, i.e. $R_i = 1$ at $Q_{acc} = 0$ C, and then calculate the R_i to re-normalize the results to the first reference run. The evolution of the target profile for one of the ^{13}C targets can be seen in Fig. 2.20.

In order to check the reliability of the target profiles obtained from the primary γ-peaks, these were compared with the NRRA scans performed at ATOMKI using the 1.7 MeV resonance in the $^{13}\mathrm{C}(p,\gamma)^{14}\mathrm{N}$ reaction. The profiles obtained with the Peak Shape Analysis were used to fit the NRRA scans. The ΔE parameter was adequately converted by using the stopping power ratios and then left fixed. All the other parameters were left free to vary. The results for two respective ^{12}C and ^{13}C targets are shown in Fig. 2.21 and Fig. 2.22. Additionally, the total degradation of the target was compared by calculating the ratio of the integrals of the profiles at the beginning and at the end of the irradiation. The results for two different targets are shown in Fig. 2.23 and Fig. 2.24. In all cases a good agreement was found between the target profiles from the Peak Shape Analysis and the NRRA scans.

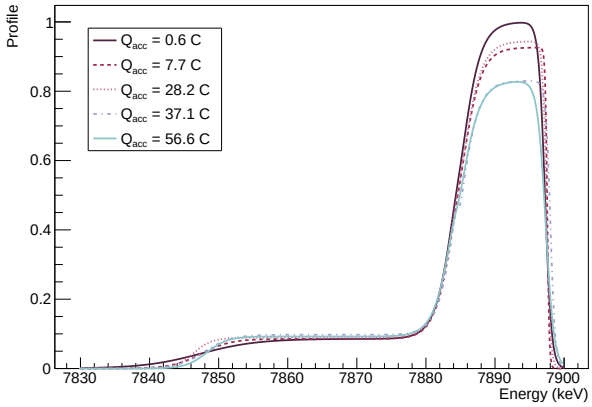

Figure 2.20: The evolution of the target profile for a ^{13}C target.

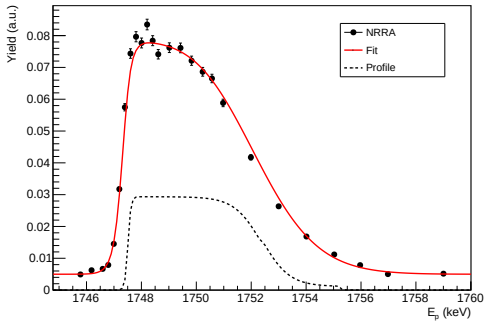

Figure 2.21: The fit of the NRRA scans with the profile obtained with the Peak Shape Analysis for a ^{12}C target.

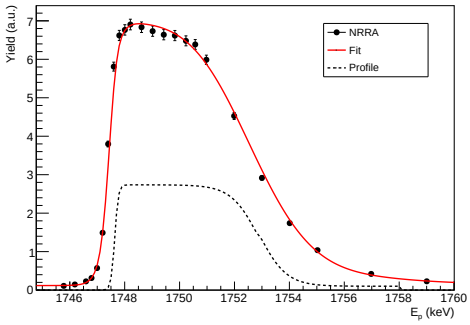

Figure 2.22: The fit of the NRRA scans with the profile obtained with the Peak Shape Analysis for a ^{13}C target.

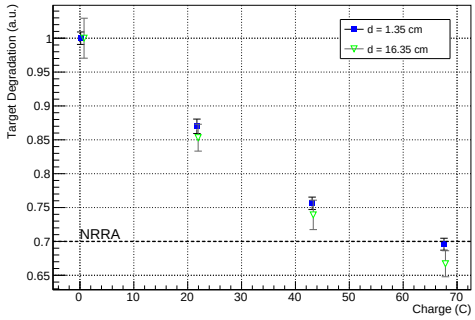

Figure 2.23: The target degradation evolution of for a ^{12}C target. The dashed line shows the result from the NRRA made after the main measurement.

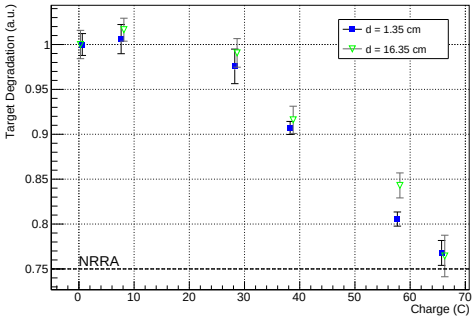

Figure 2.24: The target degradation evolution for a ^{13}C target. The dashed line shows the result from the NRRA made after the main measurement.

After the analyzing the reference runs, all the remaining runs were fitted. The non resonant cross, $\sigma_{\mathrm{NR}}(E_p)$, section was written in terms of the S-factor, $S_{\mathrm{DC}}(E_p)$, which was then left free to vary. All the other parameters were restricted in a 3σ region of the previously obtained values. In case of the ΔE, the value was calculated run by run (depending on the total beam charge accumulated on target up to that point) by linearly interpolating its value between the previous and the next reference run. Additionally, it was scaled to the energy of the given run using the stopping power ratio at the run energy and at the reference energy. In case of the $^{13}\mathrm{C}(p,\gamma)^{14}\mathrm{N}$ reaction, as discussed, transitions to several excited states are present. The same procedure was used for those. In Fig. 2.25 and in Fig. 2.26 some examples of fits for these transitions are showed.

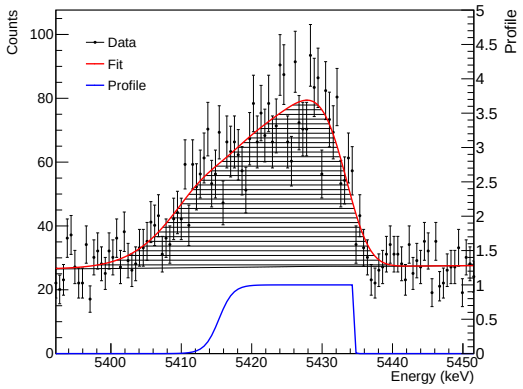

Figure 2.25: An example of the DC $\rightarrow$ 2312 keV transition fit ($E_p = 190$ keV) for the ^{13}C target. The blue line represents the target profile.

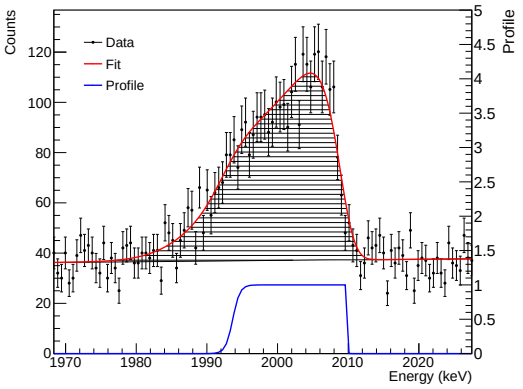

Figure 2.26: An example of the DC $\rightarrow$ 5691 keV transition fit ($E_p = 160$ keV) for the ^{13}C target. The blue line represents the target profile.

To evaluate the statistical error contribution, all the parameters were kept fixed apart from the S-factor. Then, in order to get the systematic contribution due to the target profile uncertainty, the statistical contribution was subtracted from the best-fit error obtained from the initial minimization with MINUIT. The sources and contributions of all the systematic uncertainties are shown in Tab. 2.4 and in Tab. 2.5.

Finally, the obtained values of S-factor for both the ^{12}C and ^{13}C, are shown in Fig. 2.27 and in Fig. 2.28, respectively. The minor transitions for the ^{13}C are showed in Fig. 2.29 - 2.33. In case of the DC $\rightarrow$ 4915 and DC $\rightarrow$ 5691 transitions, the data are corrected for the angular distribution reported in [27] by calculating

Source	Percentage
Efficiency	2 %
Stopping [43]	6.4 %
Target	1.2 %
Total	6.8 %

Table 2.4: The systematic error sources for the $^{12}C(p,\gamma)^{13}N$ measurement with the HPGe.

Source	Percentage
Efficiency	2.6 %
Stopping [43]	6.4 %
Target	1.7 %
Total	7.1 %

Table 2.5: The systematic error sources for the $^{12}C(p,\gamma)^{13}N$ measurement with the HPGe.

the attenuation factors in the present geometry [36]. All the S-factor values were corrected for the screening effect using the prescriptions from [44]. The calculated screening correction amounted up to 20 % for the lowest energies. Nevertheless, above 150 keV the correction was under 5 %. A conservative uncertainty of 50 % was considered for this correction. The obtained S-factor values are 25 % and 30 % lower for, respectively, $^{12}C(p,\gamma)^{13}N$ and $^{13}C(p,\gamma)^{14}N$ literature data, indicating a new normalization for the cross sections.

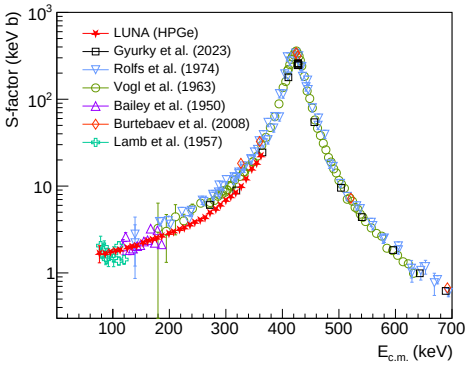

Figure 2.27: The extracted S-Factor for the $^{12}C(p,\gamma)^{13}N$ reaction.

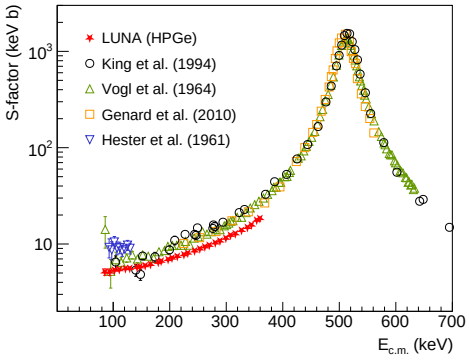

Figure 2.28: The extracted S-Factor of DC $\rightarrow$ gs for the $^{13}C(p,\gamma)^{14}N$ reaction.

2.3.4 Additional Data

During the HPGe measurement, several other data sets were acquired in order to check the data consistency. First, runs with a infinitely thick graphite target were acquired. Additionally, several runs at 55° were performed for both the reactions in order to check any possible angular distribution effects. Finally, some attempts were made to extract information about the target composition from the acquired spectra.

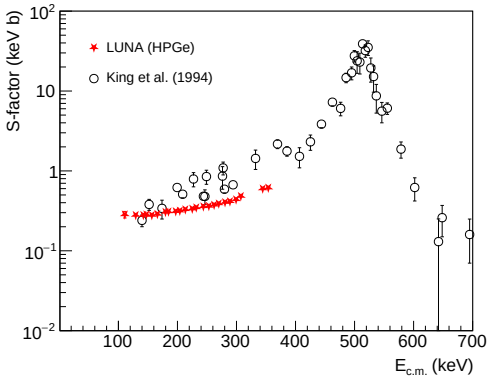

Figure 2.29: The extracted S-factor of DC $\rightarrow$ 2312 keV for the $^{13}\mathrm{C}(p,\gamma)^{14}\mathrm{N}$ reaction.

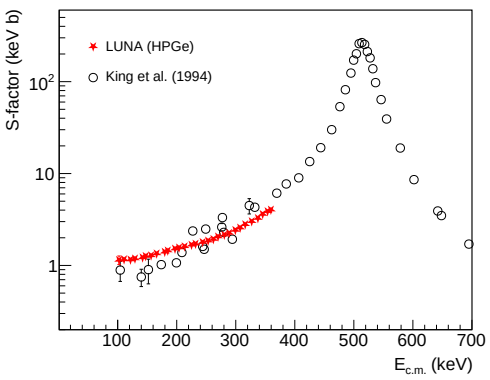

Figure 2.30: The extracted S-factor of DC $\rightarrow$ 3948 keV for the $^{13}\mathrm{C}(p,\gamma)^{14}\mathrm{N}$ reaction.

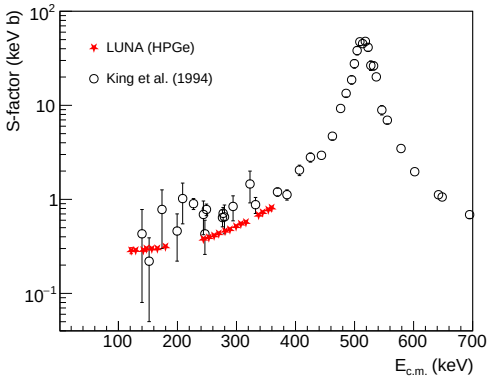

Figure 2.31: The extracted S-factor of DC $\rightarrow$ 4915 keV for the $^{13}\mathrm{C}(p,\gamma)^{14}\mathrm{N}$ reaction.

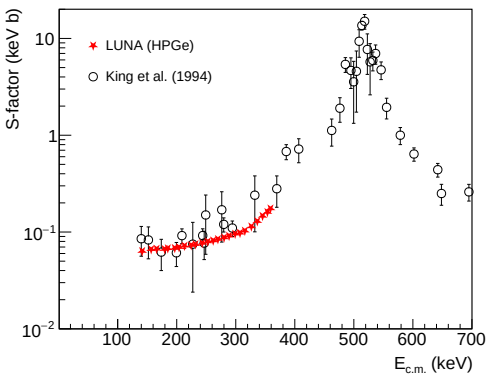

Figure 2.32: The extracted S-factor of DC $\rightarrow$ 5105 keV for the $^{13}\mathrm{C}(p,\gamma)^{14}\mathrm{N}$ reaction.

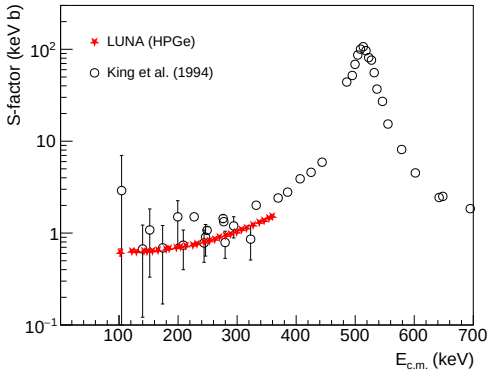

Figure 2.33: The extracted S-factor of DC $\rightarrow$ 5691 keV for the $^{13}\mathrm{C}(p,\gamma)^{14}\mathrm{N}$ reaction.

Infinitely Thick Target

A 6.35 mm thick graphite target with a reported purity of 99.999 % was mounted in the same setup configuration as the evaporated targets. Since the graphite is thick enough to stop all the beam, it is ideal to cross check the data extracted with the evaporated target. The reaction yield of the latter strongly depend on the thickness of the target whereas the former, being infinitely thick and thus stopping all the beam, is not affected by target profile and degradation, but only on the S-factor trend as a function of energy. Unfortunately, the graphite could be used only to test the $^{12}C(p,\gamma)^{13}N$ reaction, since the ^{13}C abundance in the natural graphite is only 1 %.

In total four different runs were acquired: two of them in between one evaporated target and the other, where the graphite was irradiated with a 380 keV proton beam both at 1.45 cm and 16.45 cm distances, and then the other two at 380 keV and 200 keV, both in close distance.

The experimental yield was extracted from the γ-peak using the Equation 1.6. In the efficiency calculation, the target thickness was added to the detector distance to account for the smaller solid angle. Additionally, it was necessary to calculate the correction for the γ-ray absorption due to the graphite layer. The reaction occurs at the surface of the target, thus the extra material was attenuating the γ-ray flux. For this purpose, the NIST [45] absorption coefficients were used. For a 6.35 mm of graphite and a 2.2 MeV γ-ray, the original flux is reduced by 10 %.

In the the Fig. 2.34 an example of the graphite γ-peak can be seen. In Tab. 2.6 the results are reported. The expected yields were calculated by using the S-factor values from the evaporated targets. It was observed that the second set of measurements shows consistently lower yield values with respect to the expected values, probably due to an incorrect positioning of the HPGe detector. The first two, instead, agree very well with the expected values.

Angular Distribution

For the angular distribution check, the same target chamber was used but the HPGe was positioned at an angle of 55° and distance of 14 cm. This position was selected since the Legandre polynomial of second order vanishes at 55°. Additionally, the higher distance guarantees a smaller solid angle, thus higher precision in angle determination and lower uncertainty in efficiency calculation. At this distance, in fact, the summing in and summing out have much lower impact than in

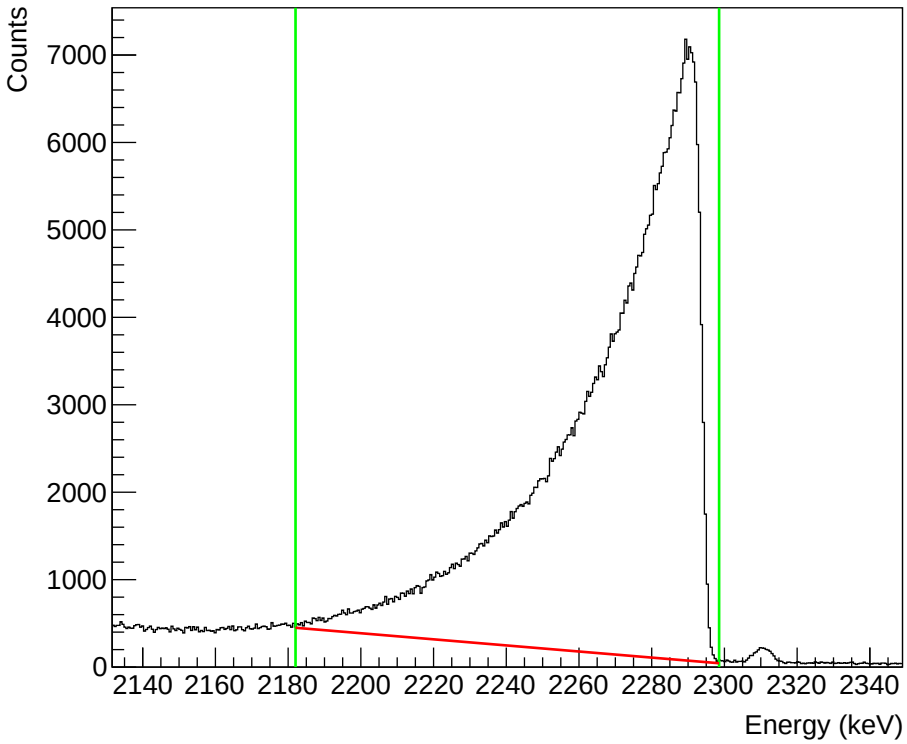

Figure 2.34: An example of the graphite γ-peak at 380 keV in close geometry. The green and red lines represents, respectively, the ROI and the calculated background.

Energy	Position	Observed Yield	Calculated Yield	Discrepancy
380 keV	1.985 cm	$(1.24 \pm 0.01) \times 10^{11}$	1.234×10^{11}	0.5 %
380 keV	16.985 cm	$(1.25 \pm 0.01) \times 10^{11}$	1.234×10^{11}	1.3 %
380 keV	1.985 cm	$(9.67 \pm 0.01) \times 10^{12}$	1.234×10^{11}	-21.6 %
200 keV	1.985 cm	$(4.02 \pm 0.02) \times 10^{14}$	5.029×10^{14}	-20.1 %

Table 2.6: Results for the graphite target. The second set of measurements shows a consistent discrepancy with the calculated values.

close distance.

The new geometry was calibrated in efficiency. The procedure was the same as the one described in Section 2.3.2. The systematic error for the efficiency ranges from 2.2 % at 2 MeV to 4.6 % at 8 MeV. The result of the multiparametric fit can be seen in Fig. 2.35.

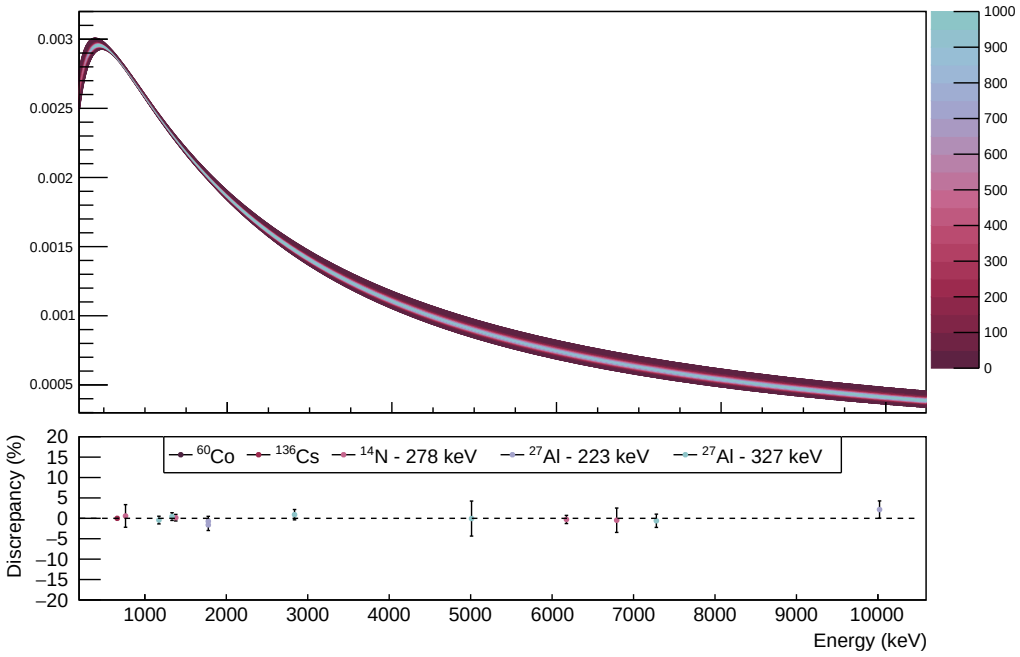

Figure 2.35: The result of the multiparametric fit for the efficiency in the 55° geometry. In the upper panel the result of the Monte Carlo treatment is displayed.

The γ-peaks were integrated and the yields calculated. In case of the $^{13}C(p,\gamma)^{14}N$, the values were corrected with the angular distributions reported in [27]. The discrepancies with respect to the yields extracted at 0° are shown in Tab. 2.7 and in Tab.2.8. The $^{12}C(p,\gamma)^{13}N$ reaction yields agree well with the isotropic distribution reported in the literature. For what regards the $^{13}C(p,\gamma)^{14}N$, all the transitions agree with the angular distributions reported in [27] apart for the 5105 keV one. It is the only one for which the angular distribution is not reported in the literature. Nevertheless this transitions makes only 0.5 % of the total transition probability thus should not affect the total reaction rate.

Energy (keV)	Discrepancy (%)
341.8	3 ± 4
294.8	1 ± 4
248.0	3 ± 4

Table 2.7: The discrepancies between the results at 0° and 55° for the $^{12}C(p,\gamma)^{13}N$. The calculated uncertainty is both statistical and systematic due to the efficiency.

Transition	Energy (keV)	Discrepancy (%)
0 keV	343.4	2 ± 4
	287.2	-3 ± 4
	192.6	-2 ± 4
2312 keV	343.4	1 ± 10
	287.2	5 ± 10
	192.6	-6 ± 9
3948 keV	343.4	-7 ± 9
	287.2	-3 ± 9
	192.6	-5 ± 9

Transition	Energy (keV)	Discrepancy (%)
4915 keV	343.4	-2 ± 9
	287.2	-7 ± 9
	192.6	-4 ± 9
5105 keV	343.4	45 ± 22
	287.2	68 ± 22
	192.6	52 ± 20
5691 keV	343.4	-4 ± 9
	287.2	-5 ± 9
	192.6	-6 ± 9

Table 2.8: The discrepancies between the results at 0° and 55° for the $^{13}C(p,\gamma)^{14}N$. The reported uncertainty is the sum of the statistical and the efficiency one.

Target Composition

The isotopic purities of the ^{12}C and ^{13}C targets reported by Sigma-Aldritch were tested by analyzing the spectra of the reference runs. Since these were performed consistently during the irradiation, they permitted to look for any change in the isotopic ratio during the irradiation.

Initially, the search was made for any possible contaminant other than carbon. For this, all the γ-peaks in the spectra were identified. In Fig. 2.8 an example of spectra for both the reactions are shown. No evidence of contaminants other than ^{19}F, which is a well-know Beam Induced Background (BIB) at LUNA [30], were found in the spectra.

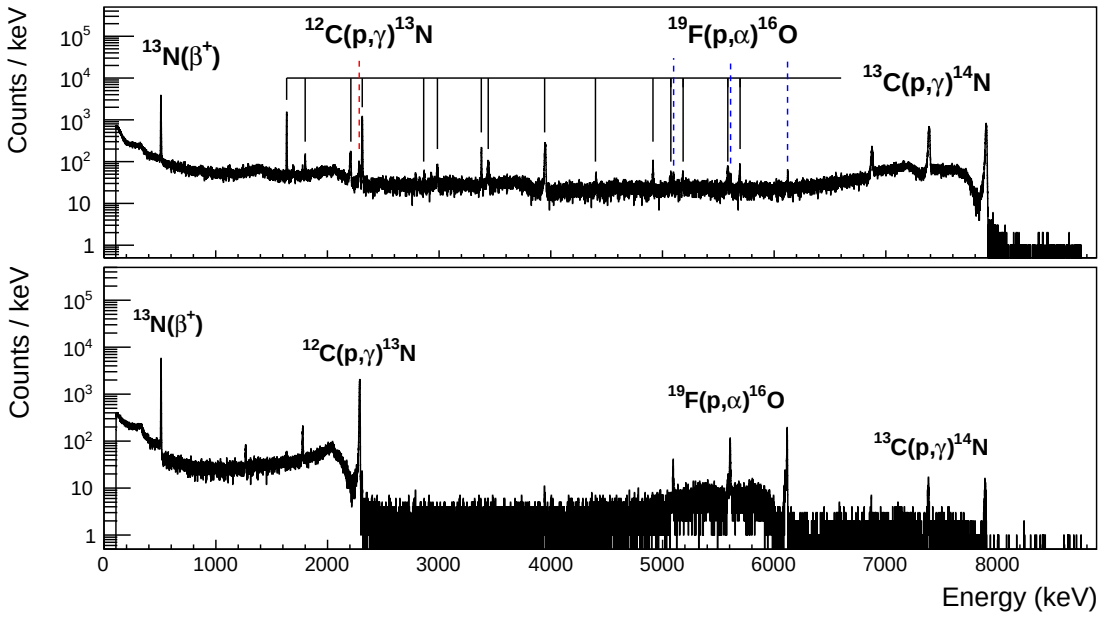

Figure 2.36: The spectra for both the ^{13}C$(p,\gamma)^{14}$N (upper panel) and ^{12}C$(p,\gamma)^{13}$N (lower panel).

The ^{13}C and ^{12}C peaks were then analyzed in spectra of both the reactions. The yield were calculated by integrating the γ-peaks. Then the following relation was used:

$$\frac{Y_{^{12}\mathrm{C}}}{Y_{^{13}\mathrm{C}}} = \frac{R \int_{\Delta E} \frac{\sigma_{^{12}\mathrm{C}}(E)}{\epsilon(E)}}{(1-R) \int_{\Delta E} \frac{\sigma_{^{13}\mathrm{C}}(E)}{\epsilon(E)}} \tag{2.35}$$

where the cross sections are the ones previously obtained, and the R parameter is the isotopic ratio of carbon inside the target, and $\epsilon(E)$ is the stopping power in

case of pure either ^{12}C or ^{13}C target. The results are shown in Tab. 2.9.

Target	^{12}C/^{13}C Ratio
nat3	0.988 ± 0.002
nat4	0.978 ± 0.002
nat7	0.991 ± 0.002
nat8	0.992 ± 0.002
graphite	0.991 ± 0.001

Target	^{12}C/^{13}C Ratio
enr1	0.022 ± 0.003
enr2	0.026 ± 0.003
enr3	0.013 ± 0.003

Table 2.9: Results for the isotopic ratio for the ^{12}C (left table) and the ^{13}C (right table) targets.

In case of the ^{13}C targets, the amount of the contaminating ^{12}C is higher than the expected one for two different targets. On the other hand, the ^{12}C targets seem to have an amount of ^{13}C consisted with the reported one, apart for one of the targets. This is due to the fact that the Ta backing was recycled from the $^{13}C(\alpha, n)^{16}O$ measurement [32]. Nevertheless, all the values fall well within the previously reported target uncertainty.

2.4 BGO Campaign

The second measurement of both the reactions was focused on the use of a 4π BGO detector. The high efficiency and the segmentation in six independent crystals permitted to push the detection limit lower than with the HPGe while losing the ability to discriminate between the different transition, given the much worse energy resolution of the BGO. An example of the spectra taken with the BGO at a beam energy of $E_p = 380$ keV is shown in Fig. 2.37.

In the first section, the method for obtaining the detection efficiency will be explained. In this case it was not viable to extract it with the multi parametric approach and thus simulations had to be exploited. Then the two analyses procedures for the respective reactions will be illustrated.

2.4.1 BGO Detector

The detector consisted of six BGO segments, each approximately 58 cm^2 $\times$ 28 cm in size, placed around a cylindrical borehole. It was shielded with a 10 cm thick lead castle to reduce the environmental background. The scheme of the setup is shown in Figure 2.38. These crystals were arranged in a way to entirely cover the target located at the center of the borehole for maximum detection efficiency of

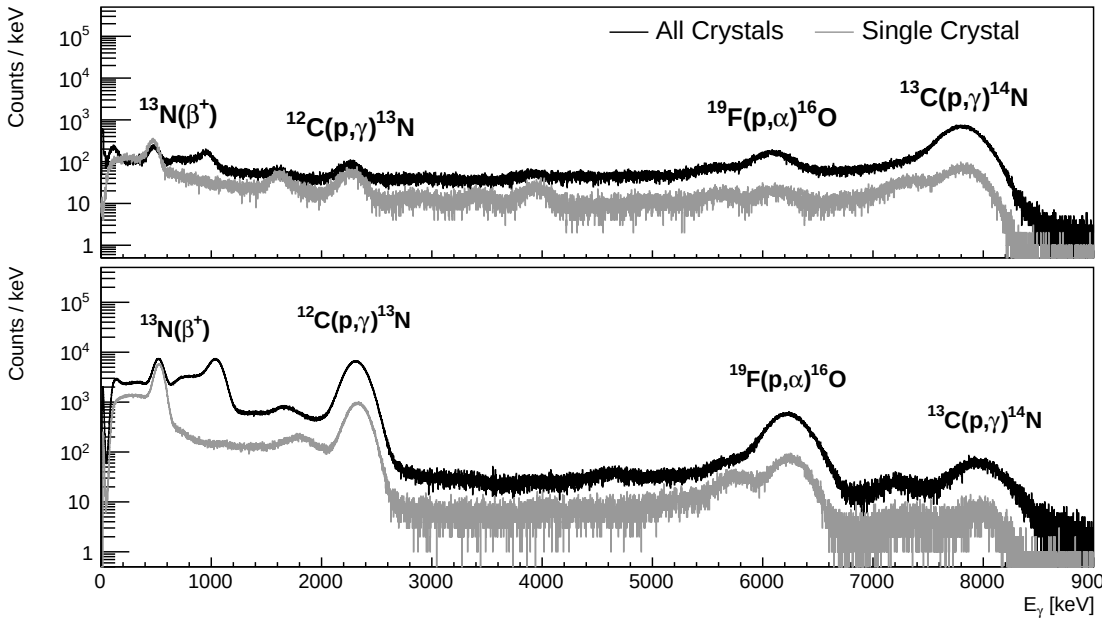

Figure 2.37: (Upper Panel) BGO spectrum of the $^{13}\mathrm{C}(p,\gamma)^{14}\mathrm{N}$ reaction at $E_p = 380$ keV. (Lower Panel) BGO spectrum of the $^{12}\mathrm{C}(p,\gamma)^{13}\mathrm{N}$ reaction at $E_p = 380$ keV.

γ-rays. The detector was designed to utilize the advantageous properties of BGO for highly efficient γ-ray detection and coverage of a large solid angle with the sensitive detector volume.

The crystals signals were read out separately by photomultiplier tubes, which were positioned at the end of the bars. The other end (towards the beamline) was covered by a plastic light reflector. The segmentation of the detector enabled the potential to recover some information about individual γ-rays in the cascades. On the contrary, by adding the single crystal signals in coincidence, the efficiency could be maximized, similar to having a detector with one large crystal.

The detector segments' six PMTs were powered by a programmable CAEN V6533 VME high voltage supply. This module had six independent channels, which meant that the voltage for each PMT could be adjusted separately. This feature enabled setting the gain of each channel such that the relationship between the amplitude of the electronic signal of the PMT and the γ-ray energy deposited in the detector was approximately the same for each channel (gain matching). The cathode output of each PMT was connected to the ORTEC preamplifiers. Additionally, a pulser signal was provided to the test input of the six preamplifiers and the test input of

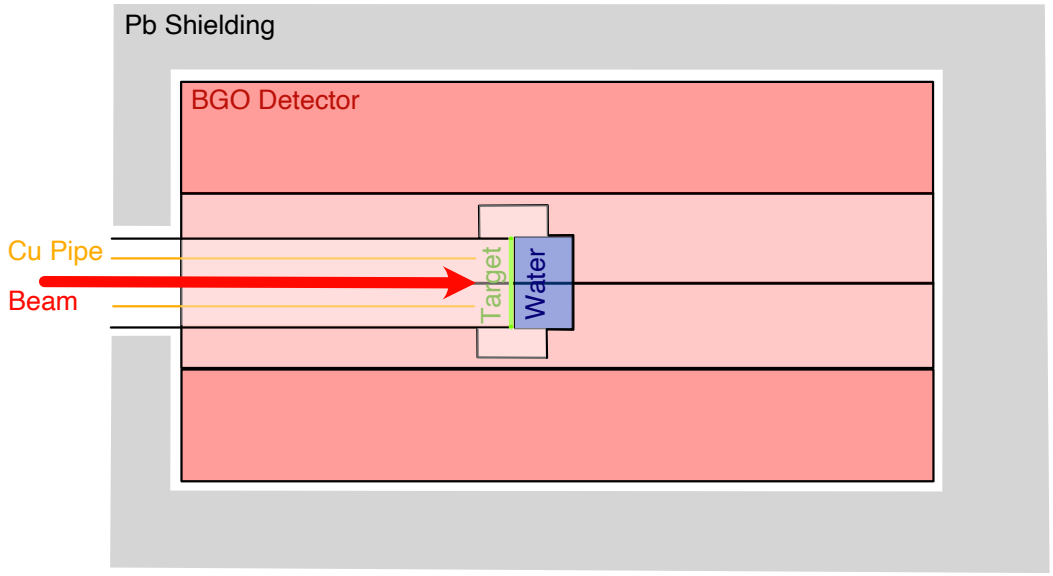

Figure 2.38: A simplified scheme of the BGO detection setup.

an additional preamplifier.

For the BGO detector, a digital data acquisition system was established. This setup involved using the CAEN V1724 digitizer with 8 channels, a resolution of 14 bit, and a sampling rate of 100 MS/s. The digitizer firmware supported pulse height analysis of the digitized signal on the internal FPGA. The CoMPASS software by CAEN was utilized for the acquisition of list mode data, gathering and saving information event by event. Each saved event included a trigger timestamp, energy, and some additional information indicating special events and conditions.

The first 7 channels of the digitizer were used to read the output of all the 7 preamplifiers. The remaining channel, instead, was connected to a pulse generator that was activated by the current integrator. This permitted to acquire one signal for 1 μC of accumulated charge. These were then used to reconstruct the current on the target.

Every channel was configured to trigger autonomously. Consequently, the obtained data consisted of list mode data for each channel, including a time stamp and energy information for each event. The digitizer supplied synchronization of the timestamps across various channels internally.

2.4.2 Efficiency

The efficiency calibration of the BGO detector is based on the Geant4 simulations [37], since the BGO detector is used in summing mode and an analytic description of the efficiency, as the one described in Section 2.3.2, would be troublesome. The efficiency itself heavily depends on the reaction that is being measured. The $^{12}C(p,\gamma)^{13}N$ emits only a single γ-ray, thus the efficiency will approximately be the sum of efficiencies in all the crystals. However, by summing the spectra from all the crystals, the events that consists of two Compton scattering in nearby crystals can be successfully reconstructed, modifying the full-energy efficiency. The $^{13}C(p,\gamma)^{14}N$, instead, emits several different γ-rays, making the efficiency much more complicated. On the other hand, the efficiency can be readily retrieved from the simulations once the implemented setup was validated them with well-known calibration sources or nuclear resonances. The geometry used in the simulations is shown in Fig.2.39.

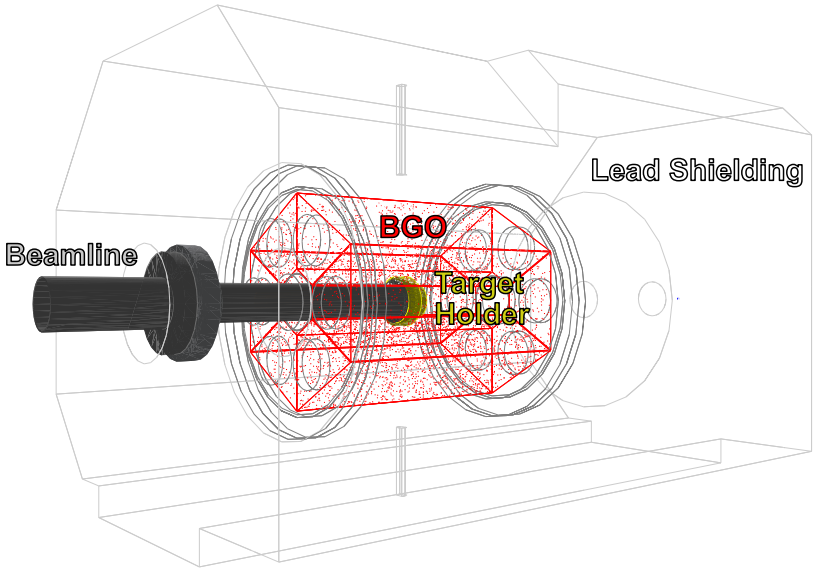

Figure 2.39: The rendering of the BGO setup used in the Geant4 simulations.

A special care had to be put on the analysis method for the γ-peaks. In order to use the simulated efficiency, the method of retrieving counts from a γ-peak should be consistent between the observed spectra and the simulated ones. The BGO crystals are known for their fluctuating gain, which could make the γ-peak to slightly drift on run by run basis. Additionally, the BGO resolution is much worse than the HPGe one and the edges of a γ-peak are not well defined. To overcome these

difficulties, the fitting of the γ-peak was preferred over the histogram integration. In this way the number of counts are much less dependant on the selected ROI. The sum peak was parametrized as follows:

$$f(E_\gamma, \sigma_\gamma, A_{\text{counts}}, A_{\text{back}}) = A_{\text{counts}} \times \mathcal{N}(E_\gamma, \sigma_\gamma) + A_{\text{back}} \times F_{\text{back}}(E_\gamma, \sigma_\gamma) \quad (2.36)$$

where the A_{counts} and A_{back} are, respectively the observed signal and backgrounds events, the $\mathcal{N}(E_\gamma, \sigma_\gamma)$ is the normal distribution and $F_{\text{back}}(E_\gamma, \sigma_\gamma)$ is a Fermi step function. All the parameters were left free to vary.

A Monte Carlo was set up in order to verify the validity of this procedure, where both for the lower and the upper limits of the fitted region were extracted from uniform distributions. For each iteration, the γ-peak was analyzed using both by fitting and by integrating the γ-peak with the assumption of a linear background [33]. The result are shown in Fig. 2.40. As can be seen, the results of the fitting are peaked around a well-defined value, almost independent from the upper and lower limits, whereas the integration method shows quite an extensive distribution, being strongly dependent on the selected region. This confirms that the fitting procedure is the optimal solution to deal with the γ-peaks measured with the BGO.

In order to validate the simulations, both the calibration sources and the ^{27}Al resonance were used. In the Fig. 2.43-2.44 the observed and simulated spectra are shown for, respectively, the ^{137}Cs and the ^{60}Co calibration source. In Tab. 2.10 and in Tab. 2.11 the obtained efficiencies from both observation and simulation are confronted. A good agreement within 2.5 % was found for both the calibration sources.

	$\eta_{ph,\ \text{sim}}$	$\eta_{ph,\ \text{obs}}$
BGO1	0.0746	0.0763 ± 0.0002
BGO2	0.0738	0.0745 ± 0.0002
BGO3	0.0737	0.0745 ± 0.0002
BGO4	0.0740	0.0754 ± 0.0002
BGO5	0.0730	0.0711 ± 0.0002
BGO6	0.0736	0.0732 ± 0.0002
Sum	0.4744	0.479 ± 0.005

Table 2.10: Results for the ^{137}Cs calibration source.

	$\eta_{ph,\ \text{sim}}$	$\eta_{ph,\ \text{obs}}$
BGO1	5.12×10^{-3}	$5.18 \pm 0.05 \times 10^{-3}$
BGO2	5.13×10^{-3}	$5.23 \pm 0.05 \times 10^{-3}$
BGO3	5.01×10^{-3}	$5.56 \pm 0.05 \times 10^{-3}$
BGO4	4.91×10^{-3}	$4.90 \pm 0.05 \times 10^{-3}$
BGO5	4.93×10^{-3}	$4.55 \pm 0.05 \times 10^{-3}$
BGO6	4.84×10^{-3}	$4.84 \pm 0.05 \times 10^{-3}$
Sum	0.2656	0.271 ± 0.004

Table 2.11: Results for the ^{60}Co calibration source. The sum-peak of the two γ-rays has been considered.

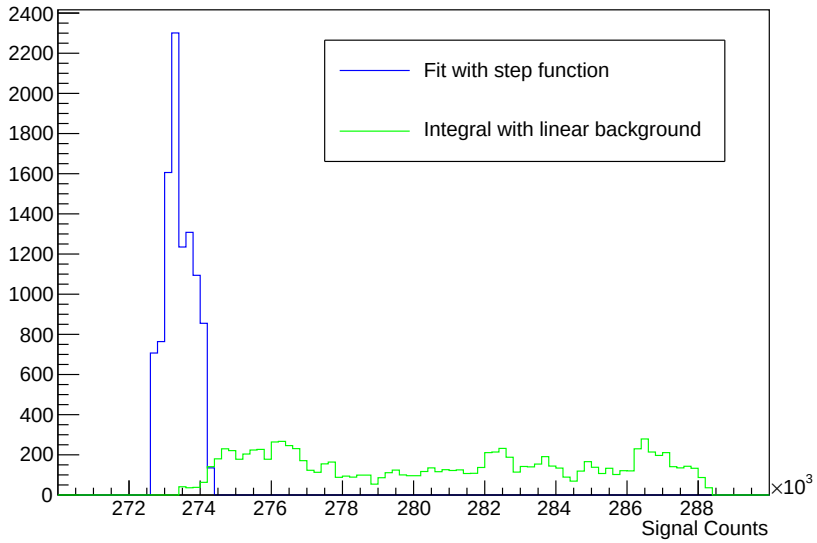

Figure 2.40: The comparison of the results for the Monte Carlo sampling of the ROI for the two methods. The integration presents a wide distribution, being heavily dependant on the ROI, whereas the fit seems to be reproducible within ~ 0.5 %.

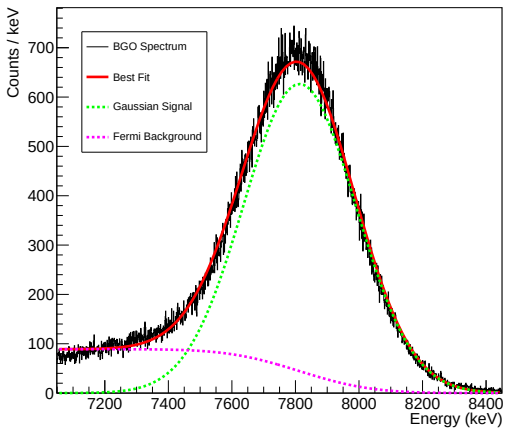

Figure 2.41: An example of the fit of the $^{13}\mathrm{C}(p,\gamma)^{14}\mathrm{N}$ sum peak.

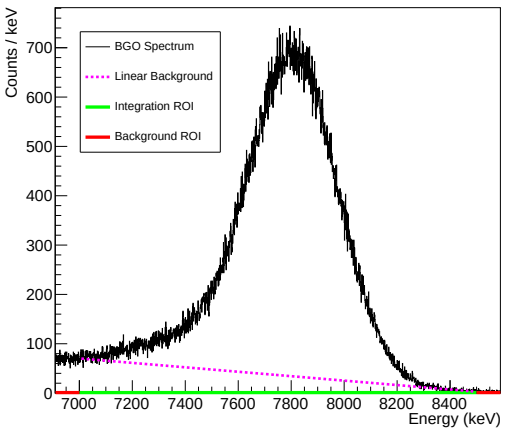

Figure 2.42: An example of the integration of the $^{13}\mathrm{C}(p,\gamma)^{14}\mathrm{N}$ sum peak.

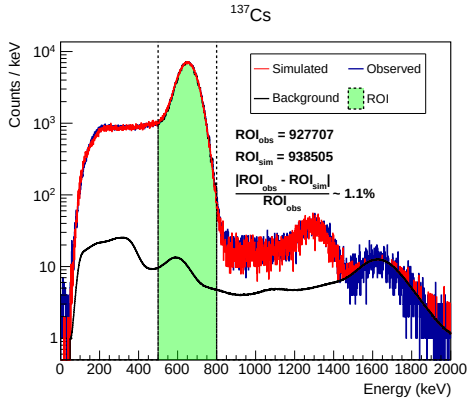

Figure 2.43: The observed and simulated ^{137}Cs spectra for the BGO detector.

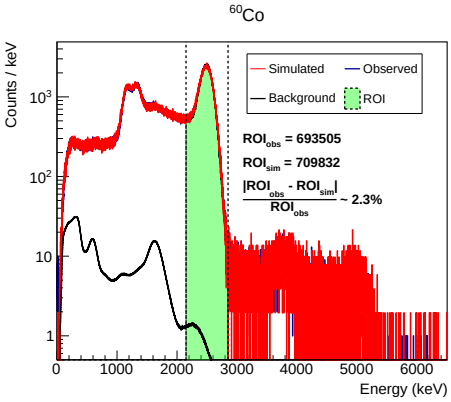

Figure 2.44: The observed and simulated ^{60}Co spectra for the BGO detector.

The calibrations sources were able to validate only the low-energy region. In order to check the efficiency at higher energies the ^{27}Al resonances at 223 keV was used. The higher lying resonances, instead, showed high background due to the ^{19}F contamination and could be not used. The branchings from [34] were used for the simulation. In order to extrapolate the efficiency, the ratio between the 1.8 MeV and 10 MeV γ-peak were calculated for both the observed and the simulated spectra. For the latter, it was necessary to use a double-Gaussian parametrization since at those energies the single-escape γ-peak is not negligible and overlaps with the full-energy one. An example is shown in Fig. 2.46. The results can be seen in Tab. 2.45. An agreement within 4 % has been found for all the crystals.

Crystal	Observed	Simulated
BGO1	0.869 ± 0.09	0.894
BGO2	0.823 ± 0.09	0.826
BGO3	0.856 ± 0.10	0.866
BGO4	0.860 ± 0.08	0.831
BGO5	0.856 ± 0.10	0.837
BGO6	0.875 ± 0.09	0.846

Figure 2.45: Ratios between the 1.8 MeV and 10 MeV γ-peaks for ^{27}Al$(p,\gamma)^{28}$Si resonance. All the results are withing 4 % of discrepancy.

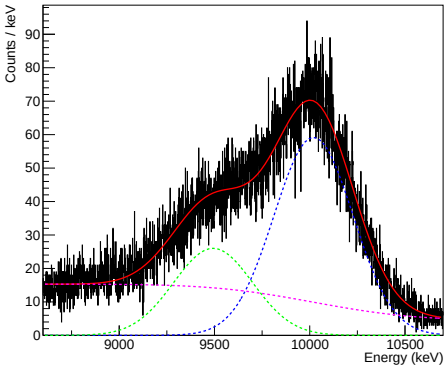

Figure 2.46: An example of the double-Gaussian fit for 10 MeV γ-peak from the ^{27}Al resonance at 223 keV.

2.4.3 $^{13}C(p,\gamma)^{14}N$ - Sum Peak Analysis

In case of the proton capture on the ^{13}C nucleus the total energy of the emitted γ-rays is high due to the high reaction Q-value. Hence, the BGO detector could be used in summing mode to construct the sum γ-spectrum from all the crystals by putting a time coincidence window of 0.2 μs [46]. This meant that that the sum γ-peak of the $^{13}C(p,\gamma)^{14}N$ lied in a background-less region of the BGO spectrum thanks to the cosmic ray reductions provided by the LNGS environment. The observed counts could then be easily calculated with the fitting method explained in the previous section. Once the counts were obtained, the reaction yield was calculated with the following formula:

$$Y_{\text{exp}} = \frac{N_{\text{counts}}}{\eta(E_\gamma)N_p} \tag{2.37}$$

where N_{counts} is the number of signal counts inside the peak, the N_p is the number of incoming protons and $\eta(E_\gamma)$ is the sum peak efficiency obtained with Geant4. In order to simulate the $^{13}C(p,\gamma)^{14}N$ reaction, the direct capture branchings obtained from the HPGe analysis were used. To investigate its impact on the efficiency uncertainty, the reaction was simulated 1000 times with the branchings being drawn from an uniform distribution which had upper and low limits are defined by 3σ interval of the calculated branchings. The obtained distribution can be seen in Fig 2.47. The error due to the branching uncertainty is calculated to be 0.5 % thus the efficiency is faintly dependant on these.

Since the beamspot was observed to be circular with a radius of approximately 3 mm and off-centered, the reaction was simulated 6 mm off center in the region observed on the irradiated targets. To do this, a Gaussian profile of the beam with a σ of 3 mm was assumed from which position of the emitted γ-rays was drawn from. The simulated region is highlighted in Fig. 2.48 where the changes of the detection efficiency is highlighted across all the target. The simulation was then repeated varying the position and the size of the beamspot center. It was observed that changing the radius of the beamspot and shifting it along the θ angle had no impact on the efficiency. The only parameter that affects the detection efficiency is the beamspot center. By assuming that the beamspot position is known within 2 mm, an uncertainty of 1.4 % was calculated for the beamspot uncertainty.

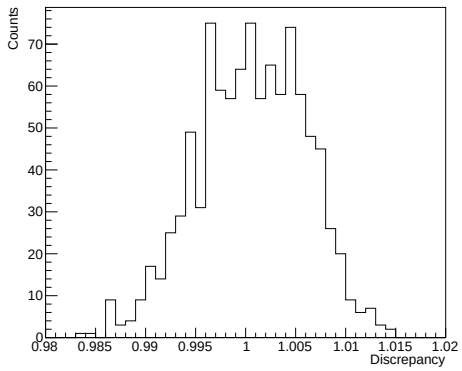

Figure 2.47: The results from the Monte Carlo sampling of the $^{13}C(p,\gamma)^{14}N$ branchings.

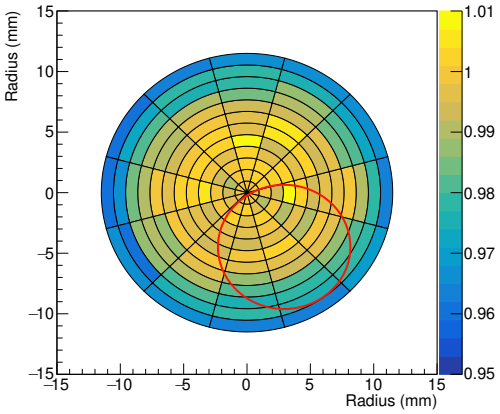

Figure 2.48: The results from beamspot sampling of the $^{13}C(p,\gamma)^{14}N$ reaction. The red circle shows the beamspot observed at LUNA. The obtained efficiencies are normalized to the value at the center of the target.

Target Degradation Since the BGO resolution does not permit to obtain any information about the target thickness, every $\sim$ 10 C of accumulated charge on target a measurement with the HPGe detector at 55° was performed and the Peak Shape Analysis applied. The HPGe was put in far geometry, at approximately 16 cm. No efficiency calibration was needed in this case since the target profile does not depend on it. The stoichiometry, instead, was obtained relatively to the first measurement.

The results for each target can be seen in Fig. 2.49. For one of the targets, the initial irradiation was performed for $\sim$ 5 C of accumulated charge in order to check the target behaviour at the beginning of the irradiation. No major deviations were found.

***S*-factor Calculation** In order to obtain the S-factor from the reaction yields, the Equation 1.6 and Equation 1.4 were used. By assuming the S-factor to be constant inside the range of the target profile, $P(E)$, it was possible to calculate the integral and extract the S-factor. In order to correct for this assumption, the effective energy, E_{eff}, was calculated for each S-factor using the Equation 1.7. Additionally, the extracted S-factors were corrected for the screening effect following the prescriptions from [44].

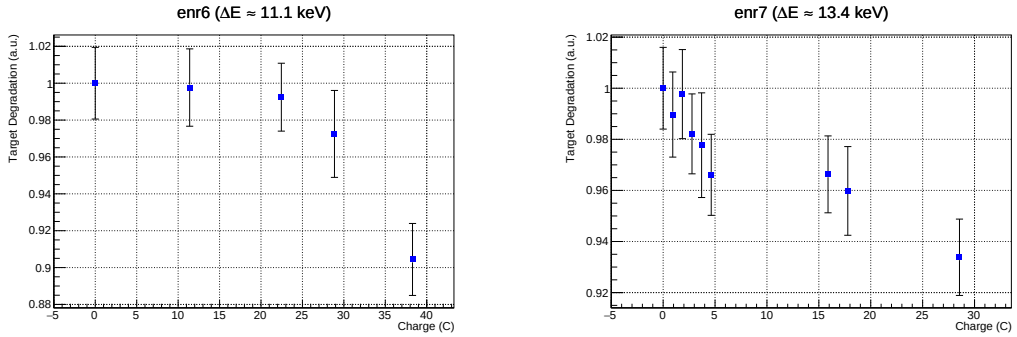

Figure 2.49: The degradation of two different targets that were used with the BGO. The enr7 target presents no unexpected behaviour during the initial prolonged irradiation.

The results are listed in Table 2.13 and can be seen in Fig. 2.50 where they are confronted with the literature and with the previous HPGe dataset. A good agreement was found between the two different approaches. The errors are divided between the statistical ones, given from Poisson counting in the γ-peak, and the systematic one coming from the uncertainty on the target profile. The uncertainties of the target profile were propagated in the Equation 1.6 with the use of the covariance matrix obtained from the fit. All the sources of systematic error are listed in Tab. 2.12.

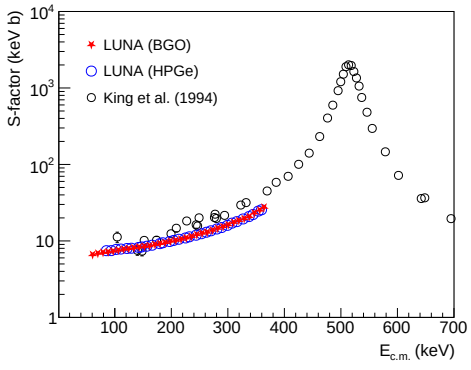

Figure 2.50: The total S-factor of the $^{13}C(p,\gamma)^{14}N$ reaction extracted from the BGO data confronted with the HPGe dataset and the literature. The only available dataset for the total capture is the [27]. Only statistical uncertainties are considered in the plot.

Source	Percentage
Efficiency	4 %
Stopping [43]	6.4 %
Target	$2 - 0.5$ %
Beamspot	1.4 %
Branching	0.5 %
Total	$7.8 - 7.6$ %

Table 2.12: The systematic error sources for the $^{13}C(p,\gamma)^{14}N$ measurement with the BGO.

$E_{\text{eff, c.m.}}$ (keV)	S-factor (keV barn)	$E_{\text{eff, c.m.}}$ (keV)	S-factor (keV barn)
363.9	$27.62 \pm 0.02_{\text{stat}} \pm 0.6_{\text{target}}$	208.0	$10.21 \pm 0.02_{\text{stat}} \pm 0.2_{\text{target}}$
356.5	$25.35 \pm 0.02_{\text{stat}} \pm 0.5_{\text{target}}$	198.6	$9.94 \pm 0.08_{\text{stat}} \pm 0.2_{\text{target}}$
347.0	$23.29 \pm 0.01_{\text{stat}} \pm 0.5_{\text{target}}$	189.5	$9.55 \pm 0.04_{\text{stat}} \pm 0.2_{\text{target}}$
338.0	$20.85 \pm 0.01_{\text{stat}} \pm 0.4_{\text{target}}$	180.1	$9.26 \pm 0.1_{\text{stat}} \pm 0.2_{\text{target}}$
328.9	$19.60 \pm 0.01_{\text{stat}} \pm 0.4_{\text{target}}$	171.1	$9.00 \pm 0.05_{\text{stat}} \pm 0.1_{\text{target}}$
319.4	$18.55 \pm 0.08_{\text{stat}} \pm 0.4_{\text{target}}$	161.7	$8.7 \pm 0.1_{\text{stat}} \pm 0.1_{\text{target}}$
310.3	$17.52 \pm 0.05_{\text{stat}} \pm 0.4_{\text{target}}$	152.6	$8.5 \pm 0.1_{\text{stat}} \pm 0.1_{\text{target}}$
300.3	$16.33 \pm 0.01_{\text{stat}} \pm 0.3_{\text{target}}$	143.2	$8.34 \pm 0.07_{\text{stat}} \pm 0.1_{\text{target}}$
291.5	$15.41 \pm 0.02_{\text{stat}} \pm 0.3_{\text{target}}$	134.0	$8.15 \pm 0.04_{\text{stat}} \pm 0.1_{\text{target}}$
282.1	$14.67 \pm 0.01_{\text{stat}} \pm 0.3_{\text{target}}$	124.7	$7.97 \pm 0.05_{\text{stat}} \pm 0.1_{\text{target}}$
273.0	$13.83 \pm 0.04_{\text{stat}} \pm 0.3_{\text{target}}$	115.8	$7.81 \pm 0.06_{\text{stat}} \pm 0.09_{\text{target}}$
263.6	$13.03 \pm 0.01_{\text{stat}} \pm 0.3_{\text{target}}$	106.5	$7.58 \pm 0.05_{\text{stat}} \pm 0.07_{\text{target}}$
254.5	$12.65 \pm 0.02_{\text{stat}} \pm 0.3_{\text{target}}$	97.2	$7.37 \pm 0.07_{\text{stat}} \pm 0.05_{\text{target}}$
245.0	$12.12 \pm 0.01_{\text{stat}} \pm 0.2_{\text{target}}$	88.3	$7.2 \pm 0.1_{\text{stat}} \pm 0.04_{\text{target}}$
235.7	$11.45 \pm 0.03_{\text{stat}} \pm 0.2_{\text{target}}$	79.1	$7.1 \pm 0.2_{\text{stat}} \pm 0.04_{\text{target}}$
226.5	$11.00 \pm 0.02_{\text{stat}} \pm 0.2_{\text{target}}$	70.0	$6.9 \pm 0.4_{\text{stat}} \pm 0.04_{\text{target}}$
217.2	$10.56 \pm 0.04_{\text{stat}} \pm 0.2_{\text{target}}$	60.7	$6.6 \pm 0.5_{\text{stat}} \pm 0.04_{\text{target}}$

Table 2.13: The extracted S-factors for the $^{13}\text{C}(p,\gamma)^{14}\text{N}$ with its statistical and systematic uncertainty due to the target profile.

2.4.4 $^{12}C(p,\gamma)^{13}N$ - Activation Method

For the measurement of the $^{12}C(p,\gamma)^{13}N$ reaction with the BGO detector the β^+ decay of the unstable ^{13}N daughter was exploited. Due to the fact that the Q-value of the reaction is low, the sum γ-peak lied in a region still affected by the detector intrinsic background. By using the activation technique, i.e. counting the number of ^{13}N decays, the background could be drastically reduced and the measurement sensitivity could be pushed to the limit. During these measurements only thick natural graphite disks were employed.

In the following the technique will be thoroughly explained. Then the calculation and validation of the detection efficiency will be dealt with. Finally the results for the $^{12}C(p,\gamma)^{13}N$ reaction will be presented.

Introduction

The BGO setup at LUNA provides many features suitable for the application of the activation technique. The 511 keV γ-rays that are emitted in a e^+ - e^- annihilation are marked by a very specific signature since they are emitted at 180° from each other. Hence, since the detector is segmented in 6 different crystals, they can be detected in coincidence in opposite sides of the detector. In this way the intrinsic and environmental background are drastically reduced. Additionally, the $^{12}C(p,\gamma)^{13}N$ reaction does not produce high energy γ-rays, thus the γ-ray interaction with the BGO crystals does not produce significant e^+ - e^- that could generate unwanted background events.

The innovative application of the BGO setup permitted to perform an in situ irradiation, meaning that the data were acquired both during the irradiation and the counting periods. On the contrary, literature studies which used the activation technique usually performed the irradiation and the measurement in two different experimental setups. The data were acquired in a devoted counting station. For this purpose, the upstream Faraday cup was connected to an Arduino board that was controlled through self-made scripts that opened and closed the cup according to the previously established schedule.

The differential equation that governs the amount of radionuclide in a sample that is being irradiated is:

$$\frac{dN}{dt} = P(t) - \lambda N(t) \tag{2.38}$$

where $N(t)$ is the number of radioactive nuclei, λ is the decay constant and $P(t)$ is the production rate. In case of a nuclear reaction, the latter can be expressed in terms of the reaction yield, Y, and the rate of incoming protons, $R_p(t)$. Thus:

$$\frac{dN}{dt}(t) = Y \times R_p(t) - \lambda N(t) \tag{2.39}$$

The solution of this differential equation gives the amount of radionuclide present at different points of time, depending only on the initial condition, the reaction yield and the incoming proton rate.

In order to retrieve the information about the reaction yield from the data, an iterative fit procedure was developed. The quantity that is directly observed and then is used for the fitting is the sample activity, $A(t)$, coming from the observed 511 keV radiation. In order to get rate of the 511 keV coincidences, the time window of 0.2 μs was set and an energy window of 511 ± 150 keV were used to search for signals in two opposite BGO crystals. The activity can be then written as follows:

$$A(t) = \eta \times \lambda N(t) + R_{\text{back}} + N_{\text{prompt}} \times R_p \tag{2.40}$$

The first term is the activity of the ^{13}N produced in the reaction multiplied by the detection efficiency. The second term is the rate of the random coincidences due to the environmental background. The last term, instead, parameterizes the background rate due to the the prompt γ-ray produced in the reaction. In fact, both the Compton events and the $e^+ - e^-$ pairs produced during the interaction of high-energy prompt γ-rays the detector can mimic either one or both 511 keV events in coincidence. Since the γ-rays amount are proportional to the proton beam current, the latter depends on the proton rate.

This equation was then used to fit the observed 511 keV coincidence rates. The reaction yield, Y, was left free to vary. The environmental background, R_{back}, was estimated from a 20 days long background rate with a value of (0.0130 ± 0.0002)

evt/s^{-1} and it was used as a nuisance parameter in the fit. The other background parameter, namely the N_{prompt}, was left free to vary.

At each iteration of the fit, the differential equation had to be solved numerically. The initial condition, N_0, was calculated from the first data point. The Poissonian likelihood was then calculated and maximized with the use of MINUIT2 package.

This procedure permits to easily include the presence of others nuclei that can be present inside the target by solving their differential equations and adding their activity to Equation 2.40. Nevertheless, in the case of $^{12}\text{C}(p,\gamma)^{13}\text{N}$ reaction, no other β^+ unstable nuclei was found in the target thus no other contribution was added in the fit.

Finally, a crucial parameter to be fixed in the fitting procedure was the detection efficiency for the 511 keV coincidences, whose determination is described in the next section.

Activation Efficiency

The efficiency calibration was based on the use of the Geant4 simulations. Two different scattering chambers were used: the same one used for all the other measurements, namely with a brass target holder and a steel target chamber, and an aluminum target holder and an aluminum target chamber, used to improve the statistics at low energies due to reduced passive layers. The simulation framework is the same one described in the previous sections.

The β^+ decay simulation, however, is more subtle than the prompt γ-ray one. The generated positron has to annihilate somewhere in the setup, and thus the detection efficiency of the emitted 511 keV γ-rays strongly depends on the geometry of the setup. Additionally, the energy distribution of the emitted positrons have to be taken into account in the simulation since the higher the energy the more probable it is for the positron to escape.

In order to validate the efficiency obtained with the Geant4 simulation, a ^{14}N target was irradiated at the 274 keV resonance, producing the ^{15}O which is β^+ unstable ($T_{1/2} = 2.041 \pm 0.006$ min [47]). The measurement was performed with both target chambers. The obtained efficiencies from the simulation for the brass and aluminum holder are 19.5 % and 29.6 %, respectively. The data were then fitted against the differential equation as explained in the previous section. A sample fit in case of the brass holder can be seen in Fig. 2.51.

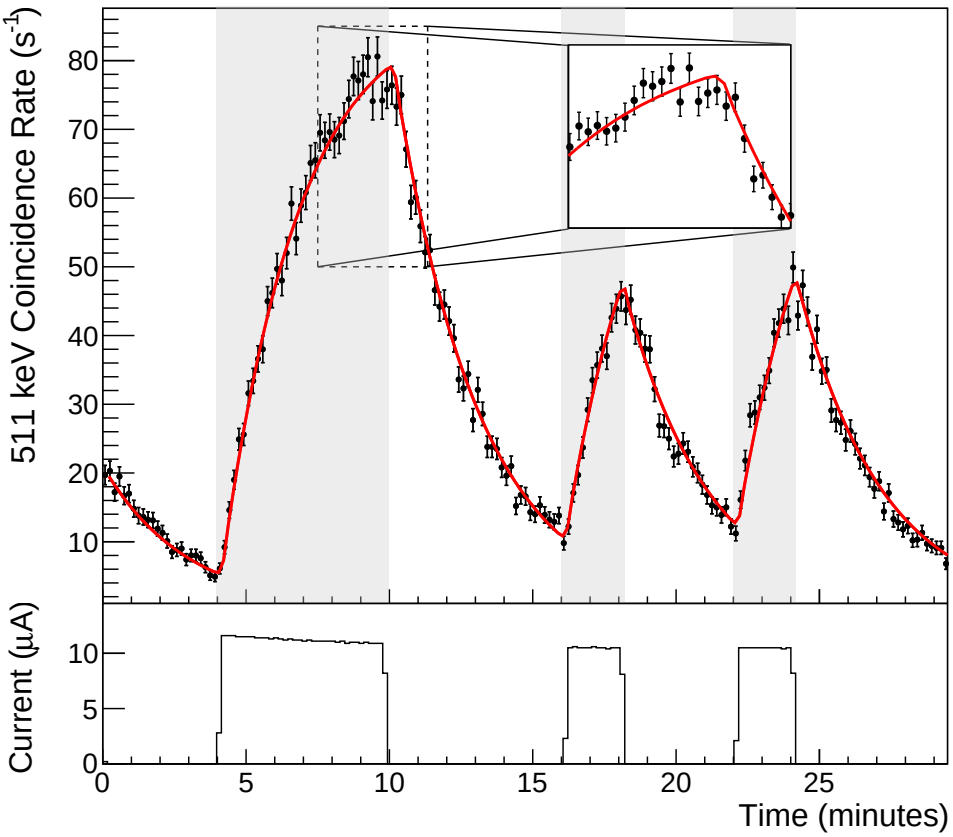

Figure 2.51: (Upper panel) The rate of the 511 keV coincidences for the ^{15}O activation on the 259 keV ^{14}N resonance. The red line is the best-fit. The shaded areas represents the irradiation time slots. (Lower panel) The current on the target.

After the yields were extracted from the activation analysis, the sum γ-peak for the same runs was analyzed and the yields were extracted. In Table 2.14 the comparison between the two analyses can be seen. A good agreement was obtained between the sum γ-peak and activation yields for both the setups.

Setup	Y_{prompt}	Y_{activ}
Brass	$6.70 \pm 0.04 \times 10^{-12}$	$6.64 \pm 0.05 \times 10^{-12}$
Aluminum	$6.60 \pm 0.03 \times 10^{-12}$	$6.68 \pm 0.04 \times 10^{-12}$

Table 2.14: The comparison between the yields obtained with the activation and the prompt-γ methods for the two different target chambers.

While preparing the simulations it was observed that the detection efficiency of two 511 keV γ-rays in coincidence is very sensible to both the position of the beamspot and the depth at which they decay inside the target. The simulated radionuclide was generated slightly off-centered, following observed beamspot, and the depth of the radionuclide was carefully studied through the use of SRIM calculations. Just as an example, the difference on the detection efficiency between the surface of the target and a depth of 1 μm is approximately 2 %, as can be seen in Fig. 2.52. For what regards the beamspot uncertainty, the same procedure as in the $^{13}\text{C}(p.\gamma)^{14}\text{N}$ case was followed. The result is shown in Fig. 2.53. In case of the 511 keV coincidences, the dependency on the beamspot position is much higher than respect to the previous case. In this case, by varying the beamspot within its observed uncertainty, analogously to Section 2.4.2, an error of 3 % can be attributed to this effect.

Once the Geant4 simulations were validated, the efficiencies for both the brass and aluminum setups were calculated, amounting to 22.2 % and 35.6 % for the respective setups. The higher value with respect to the $^{14}\text{N}(p,\gamma)^{15}\text{O}$ simulation is due to the target differences. The ^{14}N was, indeed, deposited on a Ta backing, which can easier absorb the 511 keV γ-rays than the natural graphite. A conservative error of 4 % was additionally attributed to the simulated efficiency as follows from the Section 2.4.2.

An additional check was performed to verify the efficiency value obtained for the brass holder. It consisted in an ex situ counting with the HPGe detector. The ^{12}C target was initially irradiated inside the BGO with a beam energy of $E_p = 400$ keV. The beam was then switched off and the activated target was brought in front of the HPGe detector at a distance of ~ 14 cm. A Ta plate was put on top of the target in order to confine the annihilation of positrons emitted from the

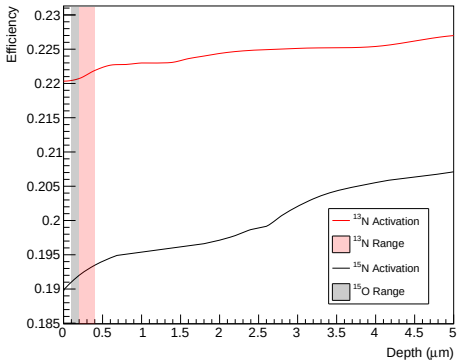

Figure 2.52: The efficiency for the 511 keV coincidences in function of the depth inside the target for both the ^{15}O and ^{13}N activation. The different efficiencies in the two cases lies in the fact that the graphite was 4 mm thick, instead the ^{14}N was directly deposited on Ta backing: the closer the positron emission is to the Ta, the higher the probability for it to annihilate.

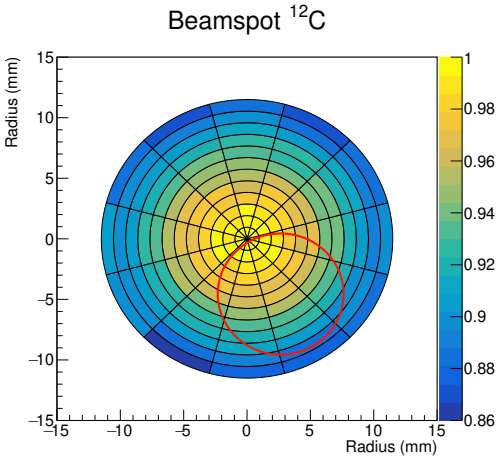

Figure 2.53: The efficiency for the 511 keV coincidences in function of the beamspot position. The red curve shows the position of the observed beamspot.

target surface. After that, the sample was brought back inside the BGO for the finale stage of counting. The HPGe detector was then calibrated in efficiency by the use of radioactive sources that emit γ-rays in region close to 511 keV. During the calibration, the sources were put under the same Ta plate to reproduce the same geometry. Finally, normalized for the respective efficiencies, the data were fitted with an exponential distribution with a fixed half-life that corresponds to the ^{13}N one. The result of the simultaneous fit for both the datasets can be seen in Fig. 2.54 and a picture of the HPGe counting can be seen in Fig. 2.55. A good agreement was found between the BGO and HPGe data.

Finally, it was possible to use the simulation to extract the probability of having prompt γ-rays to mimic the 511 keV coincidence signal inside the BGO. This is done by simulating only the γ-rays of the reaction of interest and applying the same cuts to get the 511 keV coincidences. For the ^{14}N$(p,\gamma)^{15}$O and ^{12}C$(p,\gamma)^{13}$N reactions values of respectively 0.25 % and 0.22 % were found. The value for the former reaction can be cross-checked with the results of the previous fit. The best fit value for the N_{prompt} is 0.13 ± 0.02 μC^{-1}. When multiplied by the beam current, a value of 1.4 ± 0.2 c/s is obtained. Instead, by using the obtained reaction yield, the same current on the target and the probability of having a random coincidence

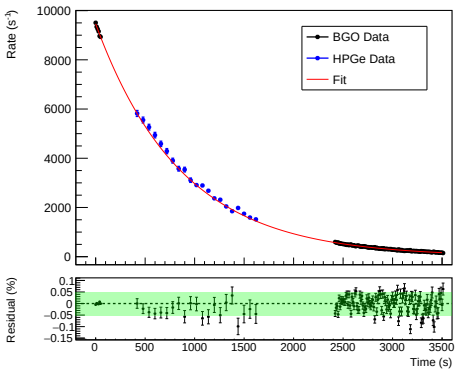

Figure 2.54: Results of the ex-situ calibration with the HPGe. The half-life used for the fit was taken from the literature [47]. In the lower panel the residuals are shown. A good agreement within 5 % has been achieved.

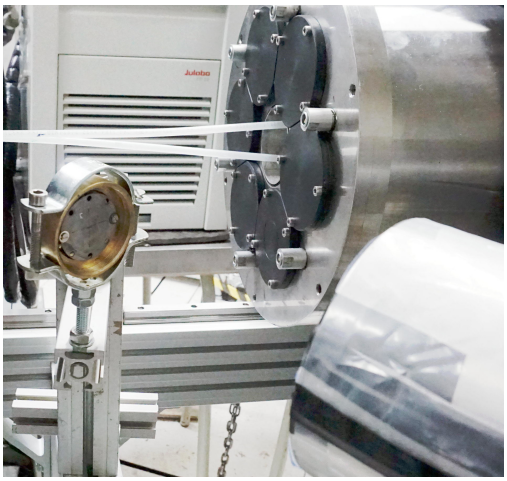

Figure 2.55: Picture of the sample in front of the HPGe used for the ex-situ calibration. The Ta plate was put on the graphite target to increase annihilation probability.

obtained from the simulation, a value of 1.2 c/s is calculated, very close to the previous value.

Hydrogen Implantation

During the measurements with the brass holder, the 380 keV runs were repeated three different times. It was observed that the yield of these runs consistently decreased. The results can be seen Fig. 2.56 and in Table 2.57.

The reason behind it is the fact that by irradiating it with a very intense proton beam, implantation of hydrogen inside the graphite target occurs. The presence of implanted ^{1}H slightly changes the stoichiometry of the target, which then directly affects its yield. It is not a trivial effect to correct for. First of all, the depth of implantation depends on the proton energies, i.e. the highest energies will implant the hydrogen in deeper layers, whereas the low energies will implant nearer the surface. Additionally, the effect on the reaction yield depends on the irradiating energies, e.g. if the protons are implanted with energies of 380 keV and then a 200 keV run is performed, the latter will not be affected since the protons will not reach the implanted layer. Thus the runs that affect the target composition the most are the low energy ones where usually 5 C of charge was accumulated. On the other side, the runs that are the most affected by the implanted layers are the highest energies, e.g. $E_p \geq 250$ keV, since in these protons reach the implanted

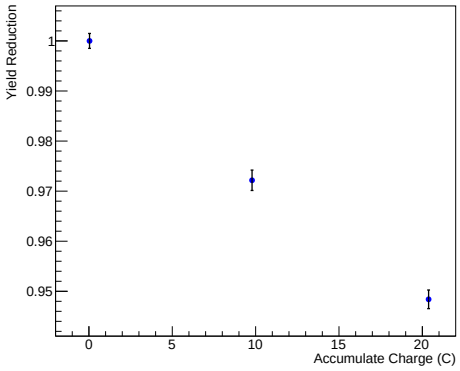

Figure 2.56: The observed yield reduction for the 380 keV runs w.r.t. to the first measurement in function of the accumulated charge.

Q_{acc} (C)	Yield (10^{-11})	Reduction (%)
0.04	1.241 ± 0.002	0
9.79	1.207 ± 0.003	2.8
20.38	1.177 ± 0.002	5.2

Figure 2.57: The observed yields for the 380 keV runs and the respective reduction w.r.t. the first run.

layer with highest energies.

For the purpose of studying the hydrogen implantation effect, the runs with the aluminum target holder were conducted after the main measurements. The material of the setup was changed due to the improvements made for the future LUNA measurements, to get higher efficiencies. Two different datasets were acquired. The first one consisted in measuring all the data points starting from 400 keV down to 250 keV. By going from the highest to the lowest energy, the hydrogen implantation effect could be avoided for these energies. The second dataset consisted in performing a 380 keV run and an overnight run at $90 - 80$ keV several times to accumulate as much charge as possible. The latter served to create a model that could be used to correct the previous measurements and then compare them with the former dataset that should not be affected by the hydrogen.

In order to calculate the correction factor, few assumptions have been made:

- The saturation ratio of H/C in each layer layer is 0.4 [48].
- Only the z-dimension, i.e. the depth of the target, was considered.
- The overabundance of H was redistributed towards the deeper layers of the target. This comes from the fact that the implanted layers will have smaller stopping powers, thus the H nuclei tends to travel slightly deeper.

The implantation profiles for each irradiation energy were simulated within the SRIM framework. Starting from the first run, the target profile was constructed

by summing the calculated H profiles, scaled by the number of incoming protons, N_p. When the H/C limit was reached, the overabundance was redistributed at deeper layers. An example of this can be seen in Fig. 2.58.

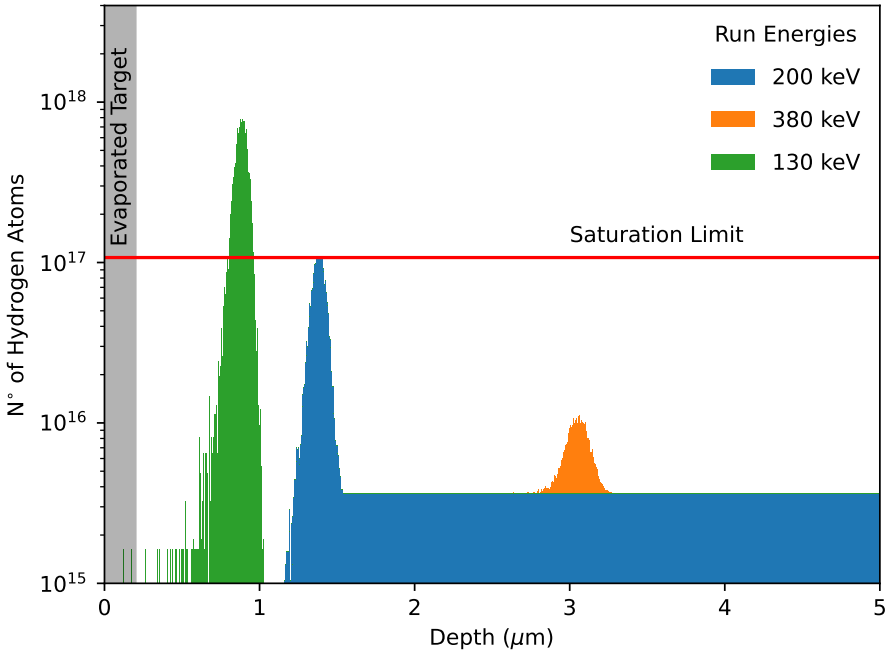

Figure 2.58: An example of the hydrogen profile inside the target after three different experimental runs. The shaded area shows the carbon layer width in case of an evaporated target. The red line indicates the saturation level for the hydrogen inside carbon.

Before calculating the correction for each experimental run, the model was validated by using the data obtained with the aluminum chamber. As previously said, these runs consist in intermittent long runs at $\sim$ 90 keV followed by reference runs at 380 keV. After the hydrogen profiles were obtained for each of theses run, the yield correction was estimated by calculating the effective stopping power with the hydrogen layers included. The results are shown in Fig. 2.59. In the figure two other models are included: one where the hydrogen is redistributed closer to the target edge and one where the hydrogen above the saturation limit is just excluded and not redistributed. As can be seen, an excellent agreement is found in case of the hydrogen being redistributed in deeper layers. Additionally, it can be clearly seen that the yield reduction saturates already at about 10 C of accumulated charge, as expected due to the saturation density reported in [48]. Since

all the corrected yields lies very close to the original ones, a 1 % uncertainty was attributed for this effect.

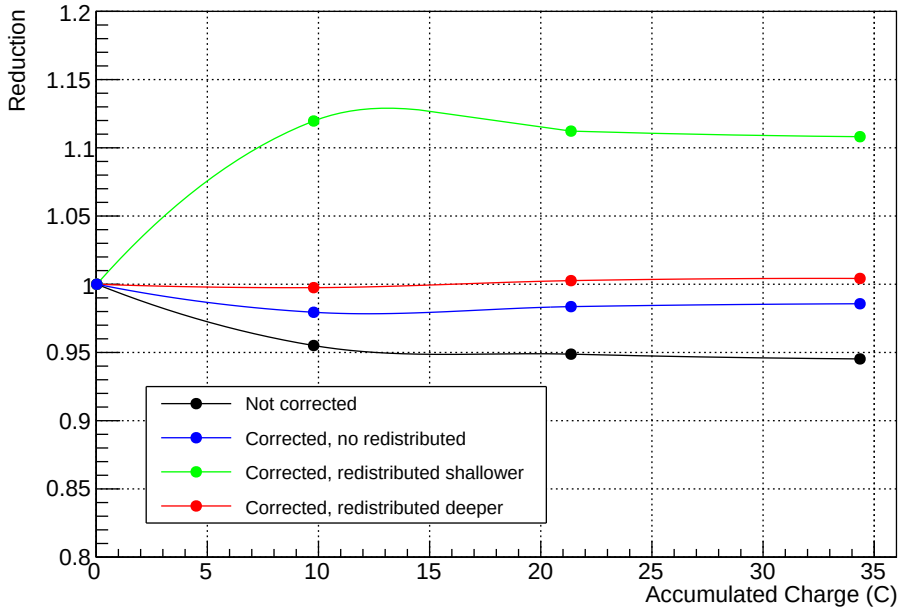

Figure 2.59: The effect of the correction factor for the hydrogen implantation inside the carbon. Three different assumption on the hydrogen redistribution are shown. The one where the hydrogen is redistributed in the deeper layers seems to describe better the data.

Finally, after the model used to correct for the implanted hydrogen was validated, the correction was analogously calculated and applied for each run of the main measurement. All the calculated correcting factors were lower than 5 % and became insignificant for runs at $E_p \leq 300$ keV.

S-factor Calculation

The main measurement of the $^{12}C(p,\gamma)^{13}N$ reaction consisted in using two different graphite disks, one for the brass target holder and one for the aluminum holder, and irradiating it with different beam-on and beam-off cycles. The yield for these runs was obtained as explained in the previous sections, and corrected according to the hydrogen implantation model.

Since the target consisted in an infinitely thick disk, it was not possible to extract the *S*-factor directly from the yield. In fact, it contains the contributions of all the energies since the beam is entirely stopped in the carbon layer. Hence, in

order to simulate a thin target, the yields of consecutive runs in terms of energy were subtracted. This permitted to treat the difference as the yield of a thin target since the runs were done mostly either in 20 keV or 10 keV steps. This permitted to proceed with the S-factor extraction from the yield analogously to the $^{13}C(p.\gamma)^{14}N$ case. The extracted S-factor values were associated to the effective energies which were calculating using the Equation 1.7. For what regards the run at the lowest energy, it was assumed that the S-factor is constant along the entire target thickness and it was accordingly calculated from the yield without any subtraction.

Finally, the S-factor values are reported in the Tab. 2.15 and shown in Fig. 2.60. All the error contributions are reported in Tab. 2.16. The results are in excellent agreement with the S-factors obtained from the HPGe campaign.

$E_{\text{eff, c.m.}}$ (keV)	S-factor (keV barn)
358.9	21.96 ± 0.05
341.7	14.13 ± 0.03
323.3	9.74 ± 0.03
304.8	7.21 ± 0.03
286.4	5.95 ± 0.01
268.0	4.57 ± 0.04
249.6	4.04 ± 0.01
231.2	3.34 ± 0.01
212.9	3.03 ± 0.01
194.5	2.79 ± 0.02
176.2	2.51 ± 0.01
157.9	2.21 ± 0.01
136.9	2.03 ± 0.02
112.6	1.83 ± 0.02
97.1	1.68 ± 0.06
87.8	1.57 ± 0.07
79.2	1.5 ± 0.2
67.9	1.6 ± 0.3

Table 2.15: The extracted S-factors for the $^{12}C(p,\gamma)^{13}N$ measurement with the BGO detector with its statistical uncertainty.

Source	Percentage
Efficiency	4 %
Stopping [43]	6.4 %
Target	1 %
Beamspot	3 %
Total	8.2 %

Table 2.16: The systematic error sources for the $^{12}C(p,\gamma)^{13}N$ activation measurement with the BGO.

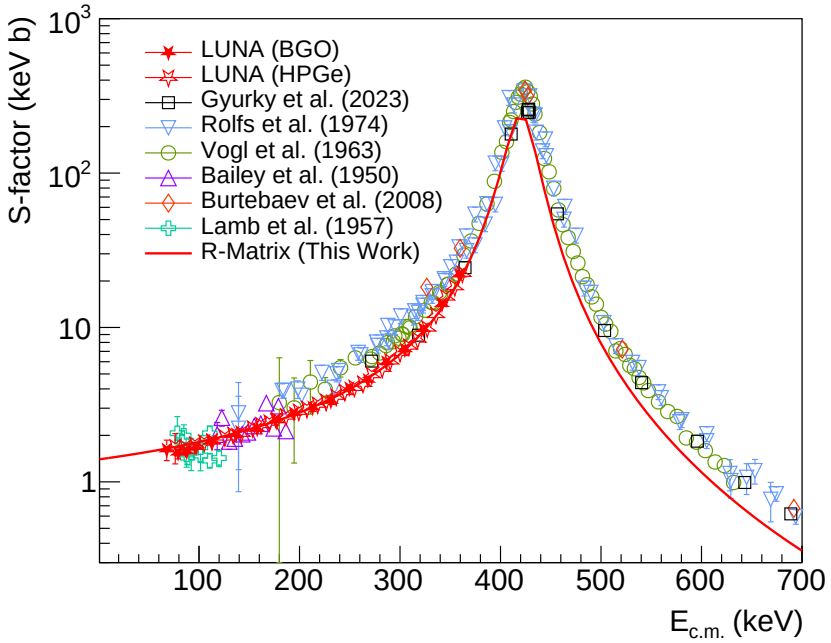

Figure 2.60: The S-factors for the $^{12}C(p,\gamma)^{13}N$ measurement with the BGO detector confronted with the values attained with the HPGe detector and the literature. Only statistical uncertainty is plotted. The R-Matrix extrapolation is taken from the Appendix A.

Sum Peak Check

Since the γ-ray from the $^{12}C(p,\gamma)^{13}N$ reaction could still be observed and well resolved with the BGO detector at proton energies above 200 keV, the same analysis as in the $^{13}C(p,\gamma)^{14}N$ sum γ-peak method was followed. First, the Geant4 simulation was performed and the efficiency value of 49 % was obtained. Then the observed sum γ-peak was analyzed by fitting into with the use of Equation 2.36. An example of the fit can be seen in Fig. 2.61.

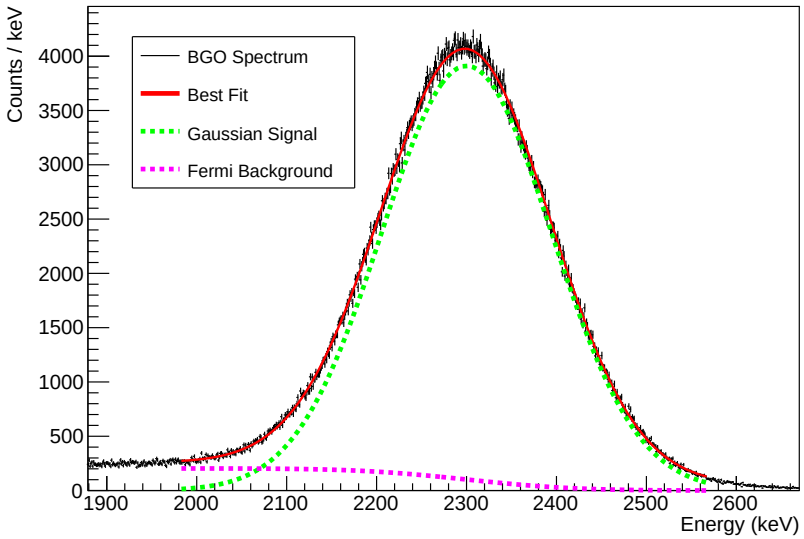

Figure 2.61: An example of the fit for the BGO sum-peak of the $^{12}C(p,\gamma)^{13}N$ reaction at $E_p = 380$ keV.

The yield were then calculated and cross checked with the values obtained from the activation method fit. In Tab. 2.17 the values for all the runs where the $^{12}C(p,\gamma)^{13}N$ γ-peak was still visible are shown. The agreement for all the runs is within 3 %.

E_p (keV)	Yield (Sum-Peak)	Yield (Activation)	Discrepancy (%)
400.0	2.33×10^{-11}	2.40×10^{-11}	-3
380.0	1.30×10^{-11}	1.28×10^{-11}	1
360.0	6.98×10^{-12}	7.09×10^{-12}	-2
340.0	4.16×10^{-12}	4.06×10^{-12}	2
320.0	2.38×10^{-12}	2.34×10^{-12}	1
300.0	1.33×10^{-12}	1.31×10^{-12}	1
280.0	7.41×10^{-13}	7.41×10^{-13}	0
260.0	4.07×10^{-13}	4.00×10^{-13}	2
240.0	2.12×10^{-13}	2.07×10^{-13}	2
220.0	1.00×10^{-13}	1.01×10^{-13}	-1

Table 2.17: Comparison of yield values between the sum-peak and activation methods. The discrepancy between all the values is withing 3 %.

Chapter 3

^{12}C(p, γ)^{13}N at Felsenkeller

The results found at the LUNA experiments suggested a different normalization for the broad resonances of both the $^{12}C(p,\gamma)^{13}N$ and $^{13}C(p,\gamma)^{14}N$ reactions. However, given the limited energy range of the LUNA 400 kV accelerator, it was not possible to cover the energy range of the respective resonances. For this reason, the Felsenkeller laboratories, located in Dresden, Germany, were selected as the best place to investigate the resonance energy range. The laboratory is provided with a 5 MV Pelletron accelerator that can provide proton beam up to 2 MeV in laboratory frame. Additionally, the laboratory is located in a previously abandoned tunnel that provides approximately 45 m of rock shielding that helps to reduce the cosmic background. Only the $^{12}C(p,\gamma)^{13}N$ reaction was investigated given the limited amount of time. The $^{13}C(p,\gamma)^{14}N$ measurements, however, are planned to be performed in the near future.

In the following chapter, the $^{12}C(p,\gamma)^{13}N$ cross section measurement at the Felsenkeller laboratories will be thoroughly explained. First, the Felsenkeller laboratory will be introduced and the experimental setup explained. Then the measurements and the analysis will be d. Finally, the newly obtained cross section will be shown and discussed.

3.1 Felsenkeller Laboratory

The Felsenkeller tunnels, located in Dresden, Germany, were built between 1856-1859 and were initially used to store ice for the Felsenkeller brewery. After the tunnels were abandoned, two experimental bunkers were installed in tunnel VIII and IX, surrounded by 40 cm thick reinforced concrete wall, floor, and ceiling. The

concrete walls were designed to limit both the γ-rays originating from the natural radioactivity of the surrounding rocks and the neutron background produced in the walls by (μ, n) reactions. This, alongside the rock shield, permits to obtain a significant background reduction with respect to the surface. The scheme of the tunnels is shown in Fig. 3.1.

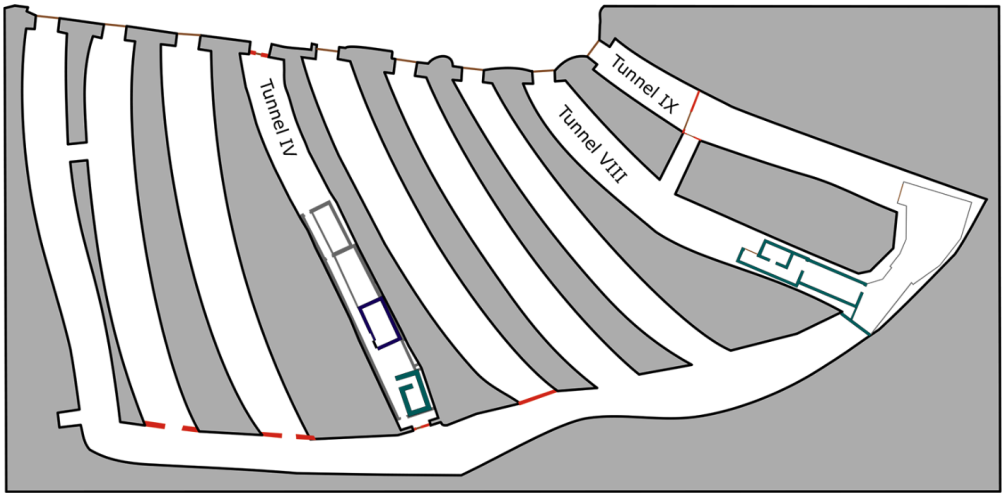

Figure 3.1: The Felsenkeller tunnel system taken from [49]. The nuclear astrophysics laboratory is located in tunnel VIII and IX. The tunnel IV has already been containing a low background counting experiments from 1982.

Subsequently, a 5 MV Pelletron accelerator was installed in between the tunnel VIII and IX. Two different sources can be used for the accelerator. The first one is a cesium sputtering source that can provide ^{12}C beam up to 100 µA. The second one is an internal RF source similar to the LUNA 400 kV one. It can provide both the proton and helium beams ranging between 10 – 100 µA. Thus the accelerator can be used in two different modes depending on the nucleus of interest that has to be accelerated.

In case of the $^{12}\mathrm{C}(p,\gamma)^{13}\mathrm{N}$ experiment, a molecular H_2 beam of about 10 µA was used. This means that at the interaction time the actual proton energy was half of the H_2 one: at the first interaction with the target, the two H nuclei splits in two with, respectively, half of the initial beam energy.

3.2 Experimental Setup

The setup at the Felsenkeller laboratories consists of several different parts. The beamline that drives the beam towards the target consists in a analyzing magnet

and several collimators used to improve the beam quality. The beam then impinges on the target that is mounted on a steel target holder. The target is mounted on a Cu layer that is cooled by liquid nitrogen, in order to prevent the target degradation through diffusion. In front of the target, a Cu pipe is both cooled by liquid nitrogen and put at a voltage of $-200\,\mathrm{V}$ to prevent that the secondary electrons escape from the target and to prevent any build up of contaminants on the target. A permanent magnet was located under the target chamber. It was needed to improve the secondary electron suppression as it was observed that the Cu pipe was not enough and decreasing the voltage had no effect on the acquired current. By placing the magnet underneath, in a way that the electrons were guided back to the target, all the current was to be correctly acquired. The position was selected by searching for a place for which the current reading was at minimum.

Around the target holder, in total 4 different HPGe clusters and one single-crystal HPGe were mounted. Their structure and positions are shown in Table 3.1. Three different clusters were mounted with the BGO crystals around them to permit the reduction of the Compton scattering by vetoing the HPGe events.

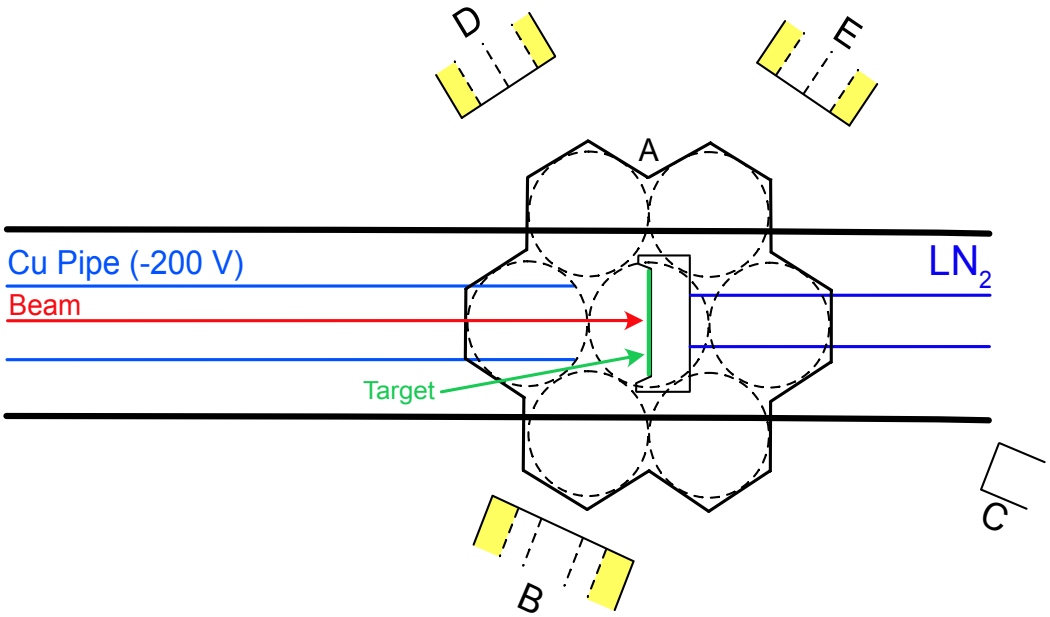

Figure 3.2: Schematic top view of the present setup. The detector main features are summarized in Tab. 3.1. The yellow regions indicate the BGO crystals around the clusters.

For the DAQ, four different CAEN V1724 boards were used. Two of them were set with a low gain, the other two, instead, with a high one. Since all of the detectors

Detector ID	Cluster Type	Relative Efficiency %	Angle (°)	Distance (cm)
A	7 crystals	7×60	90	6.1
B	7 crystals	7×60	114	19.2
C	single crystal	100	22	28.7
D	3 crystals	3×60	122	44.1
E	3 crystals	3×60	55	42.8

Table 3.1: Detectors used, their types, size, angle to the target normal (uncertainty 2°), and distance from detector endcap to target center (uncertainty 0.2 cm).

had two identical outputs, it was possible to connect one detector to two different boards. This configuration permitted to look at the high energy γ-rays without the need of changing the DAQ settings.

Finally, the current was acquired in list mode by collecting the accumulated charge with ORTEC Model 439 Digital Current Integrator that emitted one pulse for each 1 µC of accumulated charge. This was made both for the current on the target and the current on the Cu pipe. The pulses were then injected into the DAQ.

3.2.1 Targets

Three different targets were used for the experimental campaign: two evaporated ^{12}C powders on the Ta backings and one 6 mm thick graphite disk. The former were made at the ATOMKI facility analogously to the ones used for the LUNA campaign. The latter was bought from the Sigma-Aldrich which reported 99 % isotopic purity and was used to check the normalization of the evaporated targets.

The evaporated targets were characterized directly at the Felsenkeller laboratory. The atomic $^{+}$H beam was used to scan the 1.7 MeV narrow resonance of the $^{13}\mathrm{C}(p,\gamma)^{14}\mathrm{N}$ reaction. This was done twice: just after the target was mounted in the target chamber and just before dismounting it. Only 11 C and 4 C of charge was accumulated on the respective targets. The NRRA scans were then fitted with the use of the double Fermi function (Equation 2.15). The straggling effect was included in the analysis due to the high proton energies, as described in Section 2.3.3. The NRRA scans for one of the targets is shown in Fig. 3.3. No degradation has been observed for the evaporated targets.

Additionally to the NRRA scans, the γ-peak of the central crystal of the A detector

Target	NRRA (keV)	Peak Shape (keV)
L1	13.3 ± 0.8	13.8 ± 0.7
L4	15.4 ± 0.8	15.9 ± 0.7

Table 3.2: The target thicknesses (at $E_p = 380$ keV) obtained from both the NRRA scans and the Peak Shape Analysis. Both values lies withing 1σ.

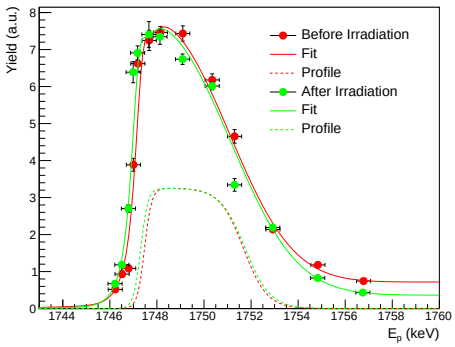

Figure 3.3: The NRRA scans for the evaporated target labeled L1 ($Q_{\text{acc}} = 11.3$ C) both at the mounting (red) and dismounting (green) time. No degradation has been observed.

was used to perform the Peak Shape Analysis to retrieve the target thickness information. As in the case of the LUNA experiments, the runs at $E_p = 380$ keV were constantly repeated during the irradiation. Also in this case no degradation has been observed for neither target. In Tab. 3.2 the results are shown for both the analyses. The thicknesses shows good agreement between the two techniques.

3.3 Analysis

During the experiments several different data were acquired. First, the detection setup efficiency was calibrated with the use of well-known calibration sources and the 992 keV resonance in the $^{27}\text{Al}(p,\gamma)^{28}\text{Si}$ reaction [50]. Then two different goals were pursued. The first one involved the absolute measurement of the $^{12}\text{C}(p,\gamma)^{13}\text{N}$ cross section, with proton energies ranging from 340 – 640 keV in approximately 10 keV steps. The second one, instead, consisted in measuring the angular distribution of the γ-ray emitted in the reaction at three different energies (below, on and above the 421 keV resonance). Finally, the thick graphite target was irradiated to check the normalization given by the finite thickness of the evaporated targets.

In the following the analysis procedure of the acquired data will be explained. First the efficiency calculation for all the HPGe detectors will be illustrated. Then the reaction yield calculation and the angular distribution will be discussed. Then the S-factor extraction will be explained. Finally, the data normalization check with the thick graphite target will be discussed.

3.3.1 Efficiency

In order to calibrate the efficiency of all the detectors the ^{137}Cs, ^{60}Co and ^{22}Na radioactive sources available at the Felsenkeller laboratory were used. Additionally, a run on a ^{27}Al target on Ta backing was performed by using a H^+ beam at approximately 1 MeV to exploit the 992 keV resonance in the $^{27}\mathrm{Al}(p,\gamma)^{28}\mathrm{Si}$ [50] reaction and extend the calibration curve up to 10 MeV.

The procedure was analogous to the one described in Section 2.3.2, with the only difference that the $D(d, E_\gamma)$ term was neglected. This is due to the fact that only one configuration was possible without changes of the detector distances. The yields were extracted from all the γ-peaks of the radioactive sources. In case of the $^{27}\mathrm{Al}(p,\gamma)^{28}\mathrm{Si}$, only the 1.7 MeV and the 10.7 MeV γ-rays were considered being the ones from the dominant γ-cascade. The other transitions were either poorly visible in the spectra or the high branching uncertainty made then unsuitable for the efficiency calibration.

In case of the ^{22}Na source, the equations taken from [51] were used. The ^{22}Na nucleus decays by through β^+ radiation to an excited state of ^{22}Ne which then de-excites by emitting the 1.2 MeV γ-ray. Hence, the prompt γ-ray is effectively emitted in coincidence with an annihilating positron that immediately creates two 511 keV γ-rays. These, being produced in pairs and having low energies, efficiently reduce the observed counts in the 1.2 MeV γ-peak because of the summing effects, and thus need special treatment with respect to all the other cases.

Each crystal of the detector was independently calibrated except the crystal 4 and the crystal 2 of, respectively, detector A and E because they broke during the experiment and thus were not used in the analysis.

The result for the central crystal of the detector A is shown in Fig. 3.4. The comparison between all the detectors is shown in Fig. 3.5. The efficiency is not well constrained in the region above 3 MeV given the limited number of high energy γ-rays in that region. Nevertheless, the uncertainty in the 2 – 2.5 MeV region, where the $^{12}\mathrm{C}(p,\gamma)^{13}\mathrm{N}$ γ-ray is effectively observed, ranges from 5 % up to 6.5 %.

3.3.2 Yield and Angular Distribution

The yield calculation for the $^{12}\mathrm{C}(p,\gamma)^{13}\mathrm{N}$ was achieved by integrating the only γ-peak of the reaction and using the Equation 1.6. A step-like background was assumed since tails on the low-energy side of the γ-peak were observed in some of

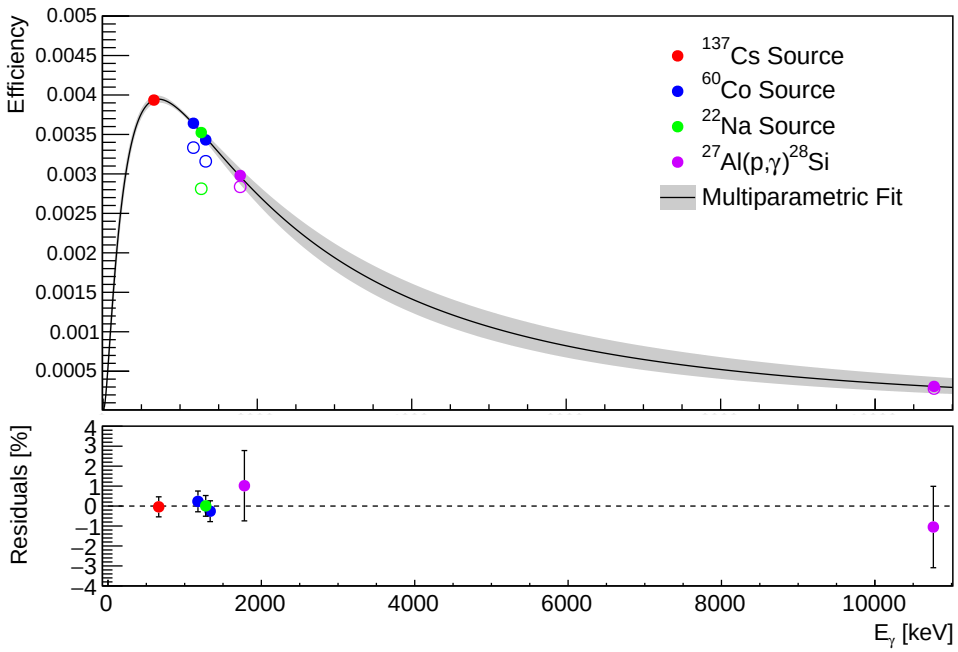

Figure 3.4: The efficiency fit result for the central crystal of the detector A. The grey band represent the 1σ uncertainty. The not filled markers shows the data without the summing correction.

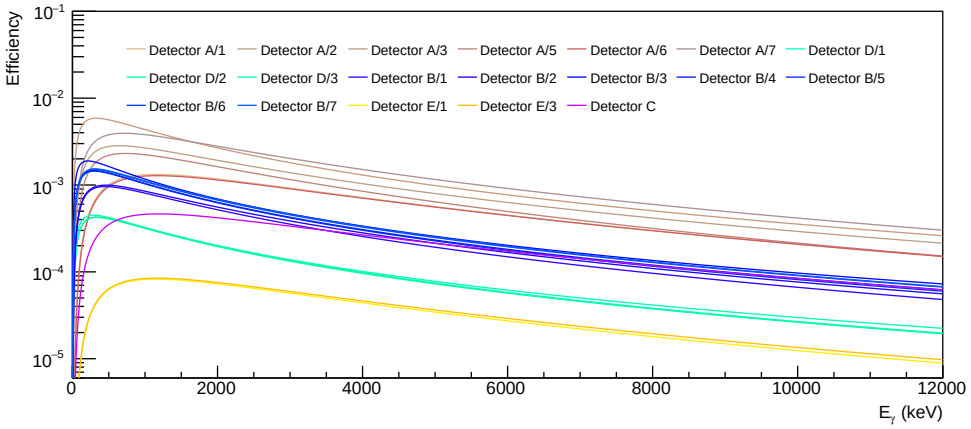

Figure 3.5: The obtained efficiencies for all the detectors used during the experiment. One crystal for both the detector A and E are not included because they were turned off.

the detectors. No other contaminants other than the nominal 1 % of ^{13}C and the ^{19}F where found inside the targets after carefully inspecting all the spectra, that are shown in Fig. 3.6 at two different proton energies. The γ-peak at 3090 keV was identified as coming from the $^{12}\mathrm{C}(d,p)^{13}\mathrm{C}$ reaction. Since a molecular beam was used for the experiment, some of the H_2 can be mixed with the deuterium due to the same charge and almost identical mass. By extracting the yield from the γ-peak and using the cross section from [52], it was possible to derive the amount of deuterium contamination inside the beam, obtaining a value of (0.07 ± 0.01) %.

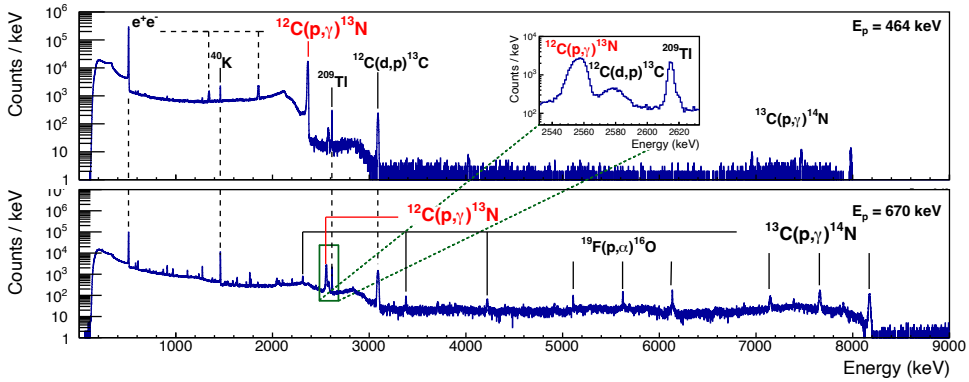

Figure 3.6: Two different γ-spectra at two different energies acquired at the Felsenkeller laboratory. No unexpected contaminant was observed from the γ-rays.

For all the runs, only the Detector A was used, since the counting statistics was poor in all the others detectors. A weighted mean was used to calculate the mean yield from all crystals.

For what regards the angular distribution, four different long runs were performed at four different beam energies where high statistics were accumulated in all the detectors. The Detector A, located very close the target and thus covering a large portion of the solid angle, was not considered in this case. Unfortunately, only first long run could be used for the Detector C since it was mispositioned during the other ones. Hence, the angular distribution check was made by calculating the yield ratio of the observed γ-ray w.r.t. the Detector B, located at 114°. The results are showed in Fig. 3.7 indicating an isotropic distribution as expected from the literature [22]. The error on the angle was calculated by considering the solid angle subtended by each detector.

Additionally to the $^{12}\mathrm{C}(p,\gamma)^{13}\mathrm{N}$ reaction, the yield was calculated also for the $^{13}\mathrm{C}(p,\gamma)^{14}\mathrm{N}$ reaction on top of the 1.7 MeV resonance, used for the target scans.

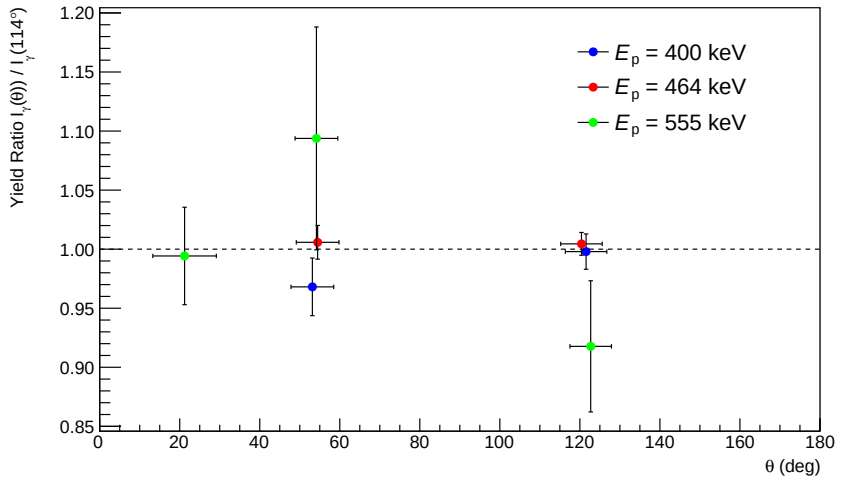

Figure 3.7: The obtained yield ratios w.r.t. the Detector B at three different proton energies. The data indicate uniform distribution of the emitted γ-ray.

Only the 8.5 MeV γ-ray was used in this case, since the other transitions were not clearly visible in the γ-spectra. The following equation was used to calculate the expected reaction yield:

$$Y = \frac{\lambda^2}{2}\frac{\omega\gamma}{\epsilon_{\text{eff}}} \tag{3.1}$$

where λ^2 is the DeBroglie wavelength, $\omega\gamma$ is the resonance strength ((7.2 ± 0.4) eV taken from [28]) and the ϵ_{eff} is the effective stopping power for a target made by 1 % of ^{13}C and 99 % of ^{12}C. By confronting the expected value with the one obtained experimentally, it was found that the nominal 1 % contamination of ^{13}C does agree well with the observation.

3.3.3 Astrophysical S-factor

Once the yields for each of the runs were obtained, the astrophysical S-factor was calculated with the use of Equation 1.6. The target profiles for each target were taken from the NRRA scans. The effective stopping power was calculated with the use of SRIM tables considering a 99 % pure ^{12}C target with 1 % of ^{13}C.

Once the S-factor was calculated, it was necessary to calculate the effective energy, E_{eff}, to associate to it. Since the data covered the whole broad resonance,

which cross section strongly depends on the energy, special care was took for this part. First, since the measured points were rather dense on the resonance peak, the points were fitted with a polynomial line. This was then used to iteratively calculate the effective energy using the following algorithm:

1. Calculation of the E_{eff} for each point with Equation 1.7.
2. Updating the polynomial line with the new E_{eff} values.
3. Checking the difference of E_{eff} with the previous values.

If the change in the E_{eff} was lower than 0.01 keV, the calculation was stopped. In order to check this procedure, the E_{eff} was in parallel calculated by using the literature cross sections. The difference in the calculated energies with respect to the previous method was less than 0.1 keV.

Additionally, it was possible to test the energy calculation even further with the use of the Peak Shape Analysis. All the information on the procedure are reported in Section 2.3.3. Only the central crystal of Detector A was used. Its energy resolution was calibrated with the use of the γ-peaks from the calibrations sources. The result can be seen in Fig. 3.8. For the fit, the polynomial line made from the previously calculated S-factor points was used. The target profile was left free to vary within the uncertainties of the NRRA profile. In this way, the only free parameter was the scaling factor w.r.t. the previously extracted S-factor curve. This permitted to both check the S-factor values and its trend with an another technique. The result for all the fits is reported in Fig. 3.9. The 95 % confidence interval was calculated that indicates an accordance of 5 % between the calculated S-factor curve and the γ-peak shape analysis.

Finally, the obtained S-factors are shown in Fig. 3.10. The obtained results do agree very well with the cross sections found in the previous LUNA experiment. In Tab. 3.3 all the systematic uncertainties are reported.

3.3.4 Thick Target Test

After the main measurement, the 6 mm thick graphite targets was mounted in the target chamber, which was then irradiated with the H_2 beam at several energies. Since all the beam is stopped inside the target itself, the data could be used to the test the target normalization of the evaporated targets.

The reaction yield was calculated from the observed counts in the $^{12}\mathrm{C}(p,\gamma)^{13}\mathrm{N}$ γ-

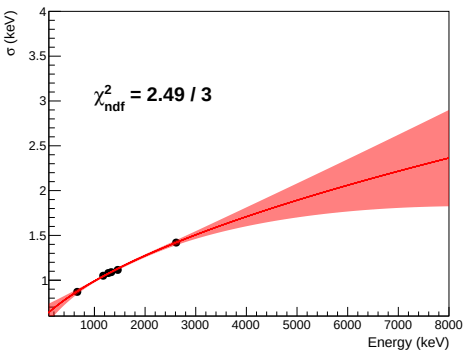

Figure 3.8: The resolution calibration of the central crystal of the Detector A. The ^{60}Co, ^{136}Cs and ^{22}Na sources were used. The colored region indicates the 3σ uncertainty.

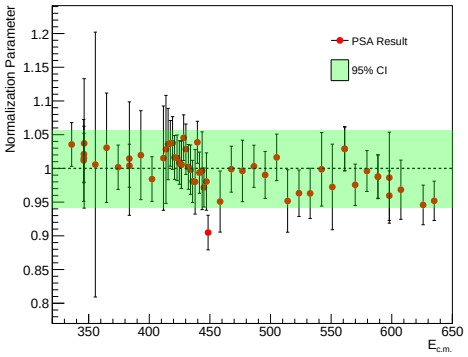

Figure 3.9: The Peak Shape Analysis result of the scaling factor for the S-factor. The calculated 95 % confidence interval indicates that all the points lies within 5 % indicating a well reproduced energy dependence of the cross section.

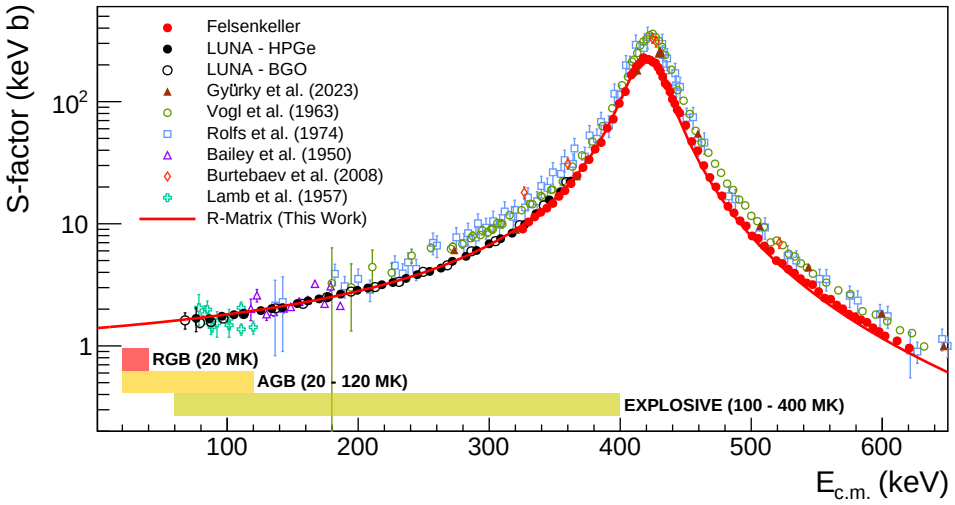

Figure 3.10: The obtained S-factors for the ^{12}C$(p,\gamma)^{13}$N reaction at the Felsenkeller confronted with the literature and with the LUNA experiment. Three regions for three different astrophysical scenarios are highlighted. The results seems to agree with the different data normalization found at LUNA.

Source	Percentage
Efficiency	6.5 %
Stopping [43]	3.5 %
Target	3 %
Charge	1.5 %
Total	8.5 %

Table 3.3: The systematic error sources for the $^{12}\mathrm{C}(p,\gamma)^{13}\mathrm{N}$ measurement at Felsenkeller. The stopping power uncertainty is lower than in LUNA case since the measured energy range is different.

$E_{\mathrm{c.m.}}$ (keV)	S-factor (keV b)	$E_{\mathrm{c.m.}}$ (keV)	S-factor (keV b)
325.6	9.05 ± 0.03	445.4	80.7 ± 0.5
330.2	10.36 ± 0.04	449.9	64.0 ± 0.4
334.8	11.40 ± 0.04	454.6	47.2 ± 0.2
339.4	12.42 ± 0.03	459.2	39.6 ± 0.2
344.0	13.42 ± 0.08	463.8	30.0 ± 0.2
348.6	14.7 ± 0.1	468.4	23.9 ± 0.2
353.2	16.8 ± 0.1	473.0	20.0 ± 0.1
357.8	18.7 ± 0.1	477.6	16.9 ± 0.1
362.4	21.30 ± 0.04	482.3	13.89 ± 0.07
367.0	24.7 ± 0.1	486.9	12.27 ± 0.08
371.6	28.8 ± 0.1	491.5	10.58 ± 0.06
376.2	33.5 ± 0.2	496.1	9.60 ± 0.08
380.9	40.8 ± 0.2	500.7	7.95 ± 0.04
385.5	46.2 ± 0.3	505.3	7.59 ± 0.05
390.1	60.6 ± 0.3	509.9	6.57 ± 0.05
394.7	71.9 ± 0.2	514.5	6.01 ± 0.05
399.3	96.7 ± 0.3	519.1	4.99 ± 0.03
403.9	120.8 ± 0.5	523.8	4.73 ± 0.04
408.5	165.4 ± 0.9	528.4	4.24 ± 0.03
410.3	174 ± 1	533.0	3.94 ± 0.03
412.1	192 ± 1	537.6	3.55 ± 0.02
414.0	201.2 ± 0.8	542.2	3.27 ± 0.02
415.9	210.7 ± 0.6	546.8	3.17 ± 0.03
417.7	229.1 ± 0.4	551.4	2.78 ± 0.02
419.6	221.9 ± 0.7	556.0	2.46 ± 0.01
421.4	222.0 ± 0.2	560.6	2.41 ± 0.02
423.3	218 ± 1	565.3	2.16 ± 0.01
425.1	210.3 ± 0.8	569.9	2.01 ± 0.02
426.9	207 ± 1	574.5	1.82 ± 0.01
428.8	191.4 ± 0.8	579.1	1.73 ± 0.01
430.6	176.9 ± 0.9	583.7	1.63 ± 0.01
432.5	159.5 ± 0.8	588.3	1.56 ± 0.01
434.3	141.0 ± 0.6	592.9	1.41 ± 0.01
436.2	134.1 ± 0.4	597.5	1.31 ± 0.01
438.0	120.5 ± 0.7	602.1	1.21 ± 0.01
439.8	104.7 ± 0.6	611.4	1.10 ± 0.01
441.7	96.1 ± 0.5	620.6	0.96 ± 0.01
443.5	85.6 ± 0.5		

Table 3.4: The extracted S-factor value of the $^{12}\mathrm{C}(p,\gamma)^{13}\mathrm{N}$ measurement at Felsenkeller. Only statistical uncertainty is included.

E_{beam} (keV)	Y_{obs}	Y_{cal}
360	$(5.04 \pm 0.09) \times 10^{-12}$	5.17×10^{-12}
380	$(1.22 \pm 0.03) \times 10^{-11}$	1.20×10^{-11}
387	$(1.47 \pm 0.03) \times 10^{-11}$	1.47×10^{-11}
393	$(1.72 \pm 0.03) \times 10^{-11}$	1.76×10^{-11}
400	$(2.20 \pm 0.04) \times 10^{-11}$	2.21×10^{-11}
407	$(2.74 \pm 0.04) \times 10^{-11}$	2.78×10^{-11}
413	$(3.47 \pm 0.05) \times 10^{-11}$	3.43×10^{-11}
420	$(4.49 \pm 0.09) \times 10^{-11}$	4.44×10^{-11}
429	$(6.7 \pm 0.1) \times 10^{-11}$	6.41×10^{-11}
436	$(8.9 \pm 0.1) \times 10^{-11}$	8.78×10^{-11}
443	$(1.26 \pm 0.02) \times 10^{-10}$	1.24×10^{-10}
450	$(1.86 \pm 0.02) \times 10^{-10}$	1.80×10^{-10}
460	$(2.96 \pm 0.02) \times 10^{-10}$	2.96×10^{-10}

Figure 3.11: The observed and calculated reaction yields for the thick graphite disks.

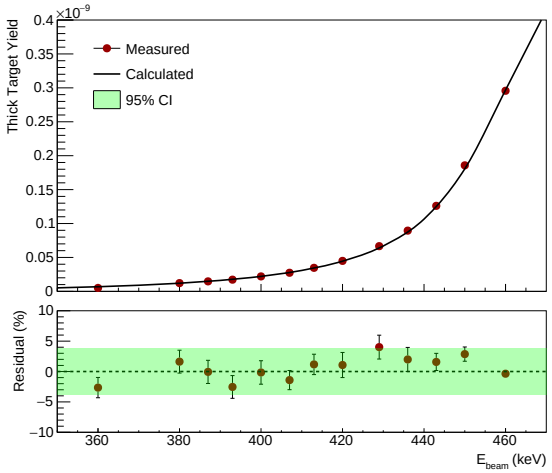

Figure 3.12: (Upper panel) The measured and the calculated reaction yields for the infinitely thick graphite disk. (Lower panel) The residuals between the calculated and the measured values and the 95 % CI.

peak. Only the central crystal of the Detector A was used. No efficiency correction was applied since the solid angle covered by the detector remained unchanged. The expected yield was then calculated using the Equation 1.6 and using the S-factor values obtained from the evaporated targets data.

In Fig. 3.12 the results are shown. By calculating the 95 % confidence interval, it was derived that the measured yields agrees with the previous results within 4 %, which is lower than the reported systematic error for the S-factors. Hence, an excellent agreement was found.

Chapter 4

Conclusions

This PhD. thesis has undertaken a comprehensive investigation into the $^{12}C(p,\gamma)^{13}N$ and $^{13}C(p,\gamma)^{14}N$ cross sections, essential for understanding of the $^{12}C/^{13}C$ ratio in astrophysical scenarios. The experimental data obtained from rigorous experiments conducted at both the LUNA and Felsenkeller laboratories have provided new precise cross section values for both the reactions. Several different additional measurements were undertaken and analyzed in order to reduce the systematic effects as much as possible. The results for both the reactions indicates a significant normalization problem of the literature values. The deviation ranges between 25 % and 30 % and was recently confirmed for the $^{12}C(p,\gamma)^{13}N$ in [53]. The reason of the different normalization seems to lie in the different stopping power values used in the literature studies.

Finally, in order to calculate and provide new $^{12}C/^{13}C$ ratios that can be used in the stellar models, it was necessary to extrapolate the cross section in the energy range of the astrophysical scenarios. For this purpose, the phenomenological R-matrix approach was followed, which calculations are explained in Appendix A, where additionally the new reaction rates for both reactions are calculated and compared with the literature ones.

After obtaining the new extrapolation curves and calculating the reaction rates, it was possible to extract the carbon isotopic ratios, $^{12}C/^{13}C$, that are reached in stellar regions where the CNO cycle is in equilibrium. For this, the Bayesian fits in Appendix A were taken as reference since their uncertainty estimation is more reliable than the one of the frequentist approach. The Fig. 4.1 shows the isotopic ratio in the temperature range of interest.

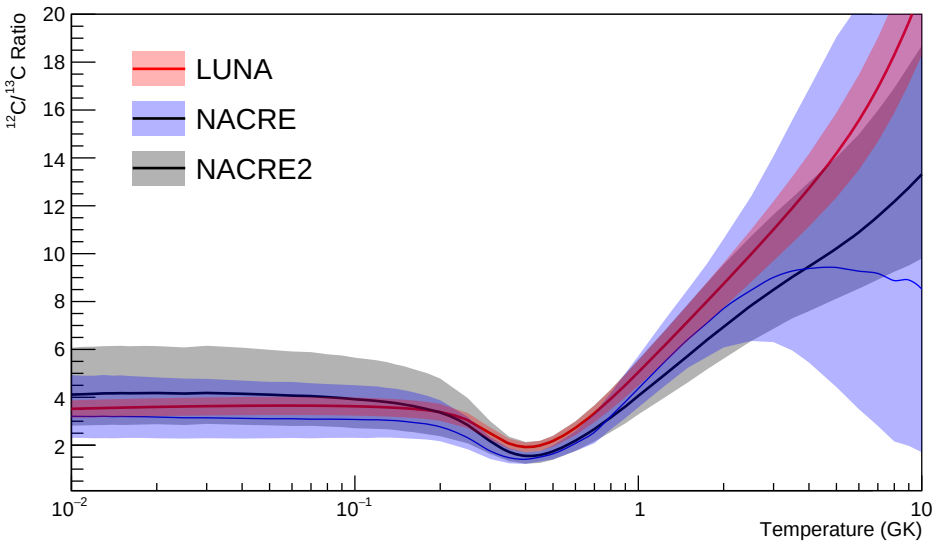

Figure 4.1: The $^{12}C/^{13}C$ ratio in function of the temperature. The new values are compared with the NACRE and NACRE2 compilations. The new ratio agrees within big uncertainties present in literature, but provide a much more precise value.

The calculated isotopic ratio is much more precise with respect to the literature ones. In the temperature region of interest ($T9 = 20 - 120$ MK), the ratio can be considered constant within the uncertainty. This is due to the fact that in this region the extrapolations are only dominated by the DC without any significant resonant contributions. The estimated value for the carbon isotopic ratio in that region is (3.5 ± 0.3). With an improved uncertainty of only 10 %, this value can be used to help constraining the RGB and AGB mixing models. Nevertheless, the impact of these values is currently under study and will be evaluated in the future.

Appendix A

R-matrix Analysis

The R-matrix theory is a quantum physics tool used to describe scattering states resulting from the interaction of particles or systems of particles such as nucleons, nuclei, electrons, atoms and molecules. The initial aim of the theory was to characterized the resonances in the nuclear reactions. The full R-matrix theory is well-established in the literature [54, 55] and its detailed procedure is out of the scope of this work. Its nature lies in the solving of coupled-channel Schrödinger equations in the continuum. First, the theory divides the configuration space into two regions, the internal and external regions. Secondly, the scattering wave function in the external region is approximated with its known asymptotic expression. The R-matrix is then calculated as the inverse of the logarithmic derivative of the wave function at the boundary and is used to match with the solution in the external region to provide the scattering matrix. From information on bound states and low-energy resonances, the R-matrix theory can accurately parametrize both resonant and non-resonant parts of low-energy cross sections using only a small number of physical parameters. Since nuclear models are still unable to reliably calculate the cross sections for capture reaction at astrophysical energies, the R-matrix approach is particularly useful and frequently used for extrapolating the cross sections at low-energies. It offers the possibility of exploiting all the experimental information about the reaction, such as cross sections, ANCs, angular distribution and resonance proprieties in a meaningful way and thus having a robust and reliable way of estimating the uncertainties.

In the following the R-matrix analysis for both the $^{12}\mathrm{C}(\mathrm{p},\gamma)^{13}\mathrm{N}$ and $^{13}\mathrm{C}(\mathrm{p},\gamma)^{14}\mathrm{N}$ reactions will be presented. First the R-matrix analysis will be described. Then the $^{12}\mathrm{C}(\mathrm{p},\gamma)^{13}\mathrm{N}$ and the $^{13}\mathrm{C}(\mathrm{p},\gamma)^{14}\mathrm{N}$ analysis will be showed. Finally, the newly

obtained uncertainties for the reaction rates will be discussed and the new $^{12}C/^{13}C$ isotopic ratios illustrated.

A.1 Analysis Approach

The R-matrix analysis is a complex subject that can be dealt with in several different ways, which can result in quite different results. Thus it is of fundamental importance to clearly lay out the procedure that was followed and the choices that have been made.

First of all, the excited states in the compound nucleus of interest has to be selected. In fact, due to both the computational limit and the lack of knowledge for the highest lying states that approach the continuum, it is not possible to include them all. This limit, however, can be bypassed by including artificial resonances, called poles, far from the energy range of interest when necessary, i.e. when the included states are not enough to describe the data. In this way, the effect of all the resonances of a given J^π can be summed up in the pole. Secondly, the reaction channels that involve the compound nuclei of interest must be included. In the case of the two reactions under study, only the (p, γ) and the (p, p) channels are considered since there are no other open channels. Then, all the literature information has to be collected and included in the analysis, which involves not only the cross section data but also the resonance parameters and the asymptotic normalization constants (ANC) that governs the direct capture contribution and can be indirectly measured in different ways [56]. Finally, the R-matrix framework should include a possibility of fitting the cross section data against the theoretical calculation, which can be done with two different approaches, either the frequentist or the Bayesian one.

The software that includes all of the aforementioned features is AZURE2 [57]. It manages both the model construction and R-matrix calculations. In principle, it can also be used to fit the data. Nevertheless, in the following analysis the AZURE2 installation was controlled by hand made scripts that use the BRICK package [58]. In this way it was possible to use AZURE2 only to do the R-matrix calculation and construct the model, whereas all the other task could have been performed with independent packages. This ensured great flexibility in establishing the fitting procedure and in evaluating the uncertainties and permitted to easily use Monte Carlo methods to check the impact of all the different parameters. As said previously, two different methodologies were used for the fitting:

Frequentist The best-fit parameters were found with the use of Minuit2 [42] package by building the following cost function [59]:

$$\chi^2 = \sum_{i,j} \left(\frac{f_j y_{\text{obs,i}} - y_{\text{theo}}}{f_j \sigma_{\text{stat},i}} \right)^2 + \left(\frac{1 - f_j}{\sigma_{\text{sist}}} \right)^2 \tag{A.1}$$

where the $y_{\text{obs,i}}$ are the observed values, y_{theo} is the theoretical prediction, $\sigma_{\text{stat},i}$ is the statistical error, σ_{sist} is the systematic error and the f_j is the normalization factor. The i-index runs over all the points in a given j-index dataset. The second term is necessary for the simultaneous fit of different datasets which might disagree and abnormally increase the χ^2 value. The error estimate for the frequentist approach, indeed, depends heavily on the assumption that the reduced chi-squared, χ^2_{dof}, is close to 1. This due to the following definition of the σ_p of the parameters set p:

$$\chi^2_{\text{dof}}\left(p_{\text{best}} + \sigma_p\right) = \chi^2_{\text{dof}}\left(p_{\text{best}}\right) + 1 \tag{A.2}$$

Thus, if the χ^2_{dof} is bigger than 1, a small variation of the parameters is enough to increase the reduced chi-squared by 1. The opposite happens when the reduced chi-squared is lower than 1. Usually it is noted that in the former case the uncertainties of the data are underestimated, and in the latter they are overestimated [60]. Since in most of the cases the introduction of the normalization factor is not enough to bring the reduced chi-squared down, because of the data scattering inside of each individual dataset, the errors are inflated in a way to bring the reduced chi-squared to 1. Then the uncertainties are evaluated [61] and the error on the extrapolations is obtained by sampling the parameters assuming that they are gaussianly distributed.

Bayesian The following log-likelihood function was defined:

$$\log \mathcal{L} = \sum_i -\frac{1}{2} \log\left(2\pi\sigma^2_{\text{stat,i}}\right) - \frac{1}{2} \left(\frac{f_j y_{\text{obs,i}} - y_{\text{theo}}}{f_j \sigma_{\text{stat},i}} \right) \tag{A.3}$$

It was then maximized with the use of the Markov chain Monte Carlo technique (MCMC) provided by the emcee package [62]. Uninformative priors were defined for all the parameters, apart from the ANCs and the normalization factors. For the former, gaussian distributions were assumed given that the values were independently measured with the use of indirect techniques. For the latter, the log-normal distribution were used due to the fact that the data normalization and its systematic uncertainty depends on number of factors, e.g. the detection efficiency, the

target and the stopping power, making it a multiplication of stochastic factors, for which the log-normal distribution is a good approximation. The number of walkers, i.e. parallel minimizations with different starting points, was equal to the number of parameters to prevent any correlation issue. This method is much more flexible and does not require the inflation of the uncertainties. For instance, the normalization parameters are naturally included by the use of their prior distribution. Additionally, the uncertainty on the energy and the energy shifts can be easily handled by introducing gaussian prior distributions peaked at 0 and with σ taken as the energy precision reported in each study.

Finally, the procedure that was followed to obtain a reliable R-matrix calculation consisted in four different steps:

1. The literature data and the literature parameters for all the excited state of interest are discussed and collected. This ensured to use R-matrix models and parameters that are well established in the literature.

2. The parameters reported in the newest studies are sampled within the stated uncertainties to assess both the literature consistency and the used R-matrix tools.

3. Finally, the new cross section data are added and the model is fitted against the data.

At all steps the reaction rate is calculated from the cross section curve, using Equation 1.3, and compared with the NACRE and NACRE2 reaction rates compilations [63, 64] to clearly underline the impact of the different values.

A.2 $^{12}\mathrm{C}(\mathrm{p},\gamma)^{13}\mathrm{N}$ Reaction

The $^{12}\mathrm{C}(\mathrm{p},\gamma)^{13}\mathrm{N}$ reaction cross section is dominated by the presence of two broad resonances at approximately 462 keV and 1700 keV. These corresponds to the (2364.9 ± 0.6) keV and (3502 ± 2) keV states, respectively, in the $^{13}\mathrm{N}$ nuclei [47].

The low-lying resonance was measured and thoroughly studied in Rolfs and Azuma [21] and Vogl [20] studies. In the first one Breit-Wigner functions were used to parametrize the resonance, whereas the second one used the R-matrix approach. Discrepancy of 5 keV exists between the reported positions of the resonance in the two studies and both studies lack details about the systematic uncertainties that affects the data and thus the reported parameters. Additionally, it is not trivial

to extract the obtained Γ_γ which governs the normalization of the resonance. Its normalization, in fact, is not well fixed. In [65] the $^{12}\mathrm{C}(\mathrm{p},\gamma)^{13}\mathrm{N}$ literature data are discussed and the renormalization by a factor of 30% of the Vogl [20] and Rolfs and Azuma [21] data is proposed in order to reproduce the Γ_γ of 0.45 eV obtained by Riess et al. [66] from a lifetime measurement. This normalization factor, however, was not followed in most of the reaction rate compilations [63, 64].

Regarding the other resonances, the only detailed study of the 1700 keV one is given by Rolfs and Azuma [21]. Nonetheless, it seems that the position of the resonance is not well known. This was pointed out by several studies [57, 64] and is evident by comparing the Rolfs and Azuma [21] results with the precise elastic scattering data of protons on ^{12}C reported in Meyer et al. [67] and Mazzoni et al. [68]. These studies were able to cover a wide energy range and give both a precise estimate for the proton width, Γ_p, and the location of both the resonances. Additionally, they points out the presence of a state at (3547 ± 4) keV that has little impact on the (p,γ) channel but is rather important to reproduce the (p,p) data [21, 67].

Reference	E_r (keV)	Γ_p (keV)	Γ_γ (eV)
Vogl [20]	462	33	
Rolfs and Azuma [21]	457 ± 1	36 ± 2	
Meyer et al. [67]	460	33	
Ajzenberg-Selove [47]	456.8 ± 0.5	31.7 ± 0.8	0.50 ± 0.04
Zhengmin et al. [69]	471 ± 5		
Burtebaev et al. [22]	456	35 ± 1	0.65 ± 0.07
Azuma et al. [57]	461 ± 3	34.1 ± 0.8	0.50 ± 0.125
Artemov et al. [70]	461	33.5 ± 1	0.63 ± 0.07

Table A.1: Literature parameters for the state at 2365 keV.

Reference	E_r (keV)	Γ_p (keV)	Γ_γ (eV)
Rolfs and Azuma [21]	1699 ± 2	62 ± 2	
Meyer et al. [67]	1688	55	
Ajzenberg-Selove [47]	1689 ± 2	62 ± 4	0.64
Burtebaev et al. [22]	1702	62	
Azuma et al. [57]	1686 ± 1	57.9 ± 1.7	
Artemov et al. [70]	1706	46.0 ± 3.4	0.35 ± 0.08

Table A.2: Literature parameters for the state at 3502 keV.

Reference	E_r (keV)	Γ_p (keV)
Meyer et al. [67]	1739	50
Ajzenberg-Selove [47]	1734 ± 6	50
Zhengmin et al. [69]	1735 ± 2	62 ± 4
Azuma et al. [57]	1735 ± 2	48.3 ± 1.9

Table A.3: Literature parameters for the state at 3545 keV.

Reference	ANC ($\mathrm{fm}^{-1/2}$)
Azuma et al. [57]	1.87 ± 0.24
Li et al. [71]	1.64 ± 0.11
Artemov et al. [70]	1.63 ± 0.12

Table A.4: Literature parameters for the state at 0 keV.

The most recent studies, namely Azuma et al. [57] and Artemov et al. [70], reevaluated the resonance parameters with the use of the modern R-matrix formalism and provided some valuable insights. The former used only the 462 keV resonance which, indeed, dominates the reaction rate at the astrophysical energies. The lat-

ter, instead, reports a new independent value for the ANC parameter that governs the direct capture contribution of the cross section and recalculates the other parameters accordingly. Additionally, it is stressed that the region in between the resonances, which is dominated by interference effects, is still poorly constrained by the data.

All the literature values are reported in Tab. A.1 and Tab. A.2 for, respectively, the first and the second resonance. In Tab. A.3 the values for a third resonance is listed, which contribution have not been observed for the (p,γ)channel. Finally, the ANC values, obtained from indirect techniques and R-matrix fits, are listed in Tab. A.4.

A.2.1 Literature Sampling

All the resonance parameters and the ANC values were taken from Artemov et al. [70], being the newest study. Since no uncertainty is reported on the energy of the resonances, these were taken from the Azuma et al. [57] study. In the sampling, Gaussian distributions were assumed for all the parameters and these were treated as independent, i.e. no covariant terms were used. The results can be seen in Fig. A.1 - A.3. The only prominent feature is the lack of agreement for the second resonance both in the (p,p) and in the (p,γ) channels. For the former, it seems that the energy of the resonance is shifted with respect to the data. For the latter, the normalization of the data seems not to agree well with the model. Nonetheless, these are well-know problems as stated in the previous section.

Finally, we used the extrapolation to calculate the reaction rate and compare it with the NACRE and NACRE2 values in [63, 64]. The results are shown in Fig. A.4. As can be seen, at the lowest energy the trend and the uncertainty is different with respect to the literature. This is due to the new ANC value provided by [70] that changes the shape of the cross section at the lowest energies. Nevertheless, an agreement within the reported uncertainties is found over the whole temperature range.

A.2.2 Fit

The newly obtained data both from the LUNA experiments and the Felsenkeller one were added to the fit. In the frequentist method, all the literature errors were inflated in order to keep their reduced χ^2 at 1 since it was observed that their large scattering did not permit to have a consistent χ^2. This permitted to leave

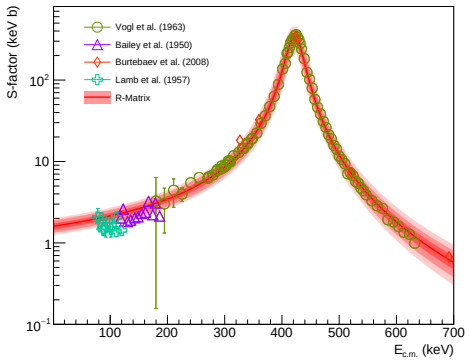

Figure A.1: The literature S-factor with the extrapolation obtained by sampling the literature parameters.

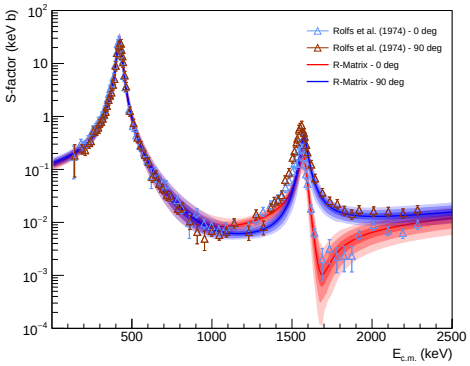

Figure A.2: The differential S-factor from [21] with the extrapolation obtained by sampling literature parameters.

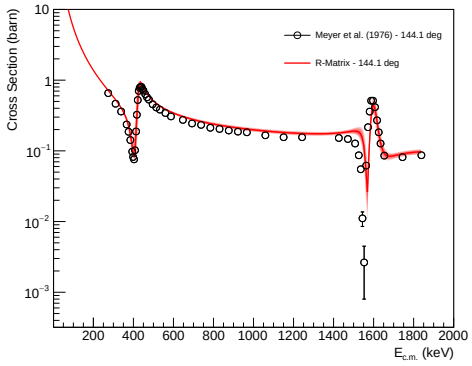

Figure A.3: The elastic scattering cross-section from [67] with the extrapolation obtained by sampling the literature parameters.

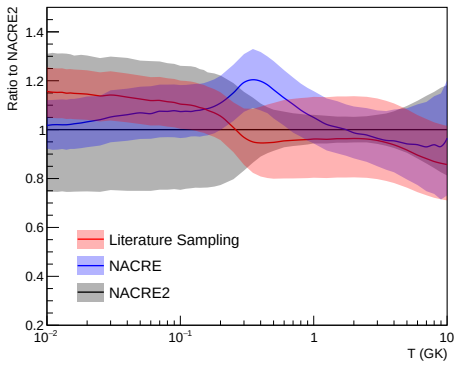

Figure A.4: The calculated reaction rate by sampling the literature parameters compared with NACRE and NACRE2 values.

the errors of the new datasets unchanged, which does not present large scattering and thus has low impact on the χ^2. A nuisance parameter was added in order to parametrize the energy shift of the Rolfs and Azuma [21] data above 1 MeV. In case of the Bayesian procedure, the prior for the Rolfs high energy data was uniform between -100 keV and 100 keV. Additionally, for normalization factors of the Vogl [20] and Rolfs and Azuma [21] datasets the priors were set uniform as well. In this way they were treated as shape data and the normalization was dominated by the present work.

In Fig. A.5 - A.8 the results for the frequentist and Bayesian approaches, respectively, are showed. In Tab. A.5 - A.8 the best fit parameters are compared. In the Appendix (Fig. A.10 and Fig. A.9) the correlation matrices are shown for Bayesian and frequentist methods, respectively.

Source	E_r (keV)	Γ_p (keV)	Γ_γ (eV)
Literature	461 ± 1	33.5 ± 1	0.63 ± 0.07
Frequentist	460.6 ± 0.2	34.5 ± 0.2	0.46 ± 0.02
Bayesian	458.9 ± 0.3	33.5 ± 0.2	0.43 ± 0.02

Table A.5: The 2365 keV resonance parameters for the fit of the $^{12}C(p,\gamma)^{13}N$.

Source	E_r (keV)	Γ_p (keV)	Γ_γ (eV)
Literature	1706 ± 1	46.0 ± 3.4	0.35 ± 0.08
Frequentist	1689.9 ± 0.3	54.2 ± 0.9	0.37 ± 0.05
Bayesian	1688.6 ± 0.4	54.1 ± 0.4	0.36 ± 0.02

Table A.6: The 3502 keV resonance parameters for the fit of the $^{12}C(p,\gamma)^{13}N$.

Source	E_r (keV)	Γ_p (keV)
Literature	1735 ± 2	48.3 ± 1.9
Frequentist	1737.0 ± 0.4	49.0 ± 0.9
Bayesian	1735.7 ± 0.5	48.9 ± 0.6

Table A.7: The 3545 keV resonance parameters for the fit of the $^{12}C(p,\gamma)^{13}N$.

Source	ANC ($fm^{-1/2}$)
Literature	1.64 ± 0.11
Frequentist	1.67 ± 0.04
Bayesian	1.80 ± 0.03

Table A.8: The ANC parameters for the fit of the $^{12}C(p,\gamma)^{13}N$.

Source	n_{Meyer}	n_{Vogl}	n_{Bailey}	$n_{\text{Burtebaev}}$	n_{Lamb}	$n_{\text{Rolfs Low}}$	$n_{\text{Rolfs High}}$	$n_{\text{LUNA HPGe}}$	$n_{\text{LUNA BGO}}$	$n_{\text{Felsenkeller}}$
Frequentist	1.00 ± 0.01	0.74 ± 0.03	1.01 ± 0.06	0.73 ± 0.07	1.12 ± 0.09	0.74 ± 0.04	0.61 ± 0.04	0.98 ± 0.04	0.98 ± 0.04	1.05 ± 0.05
Bayesian	1.01 ± 0.01	0.70 ± 0.03	1.04 ± 0.05	0.67 ± 0.04	1.17 ± 0.07	0.70 ± 0.03	0.68 ± 0.03	1.00 ± 0.04	0.99 ± 0.04	0.97 ± 0.04

Table A.9: The normalization parameters for the fit of the $^{12}C(p,\gamma)^{13}N$.

Source	χ^2_{dof}	Source	χ^2_{dof}
Meyer	0.13	Rolfs Low	0.09
Vogl	0.11	Rolfs High	0.19
Bailey	0.03	LUNA HPGe	0.08
Burtebaev	0.01	LUNA BGO	0.03
Lamb	0.01	Felsenkeller	0.16

Table A.10: Reduced χ^2 values for the fit of the $^{12}C(p,\gamma)^{13}N$.

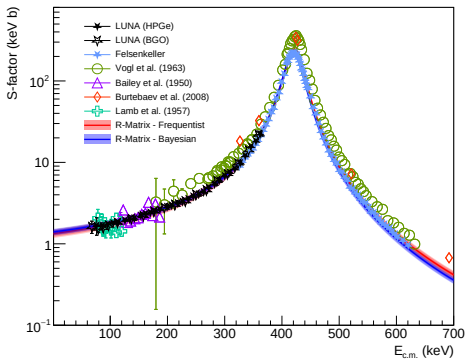

Figure A.5: The S-factor with the R-matrix fit obtained with both the approaches.

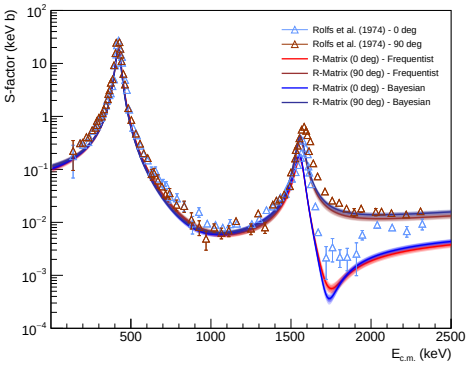

Figure A.6: The differential S-factor with the R-matrix fit obtained with both the approaches.

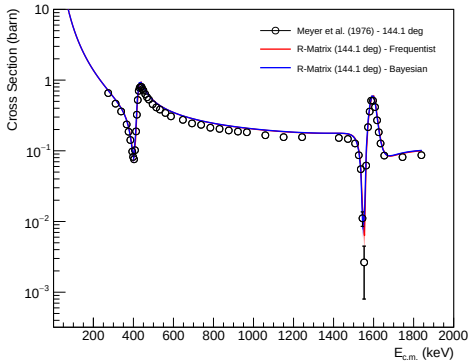

Figure A.7: The elastic scattering cross-section with the R-matrix fit obtained with both the approaches.

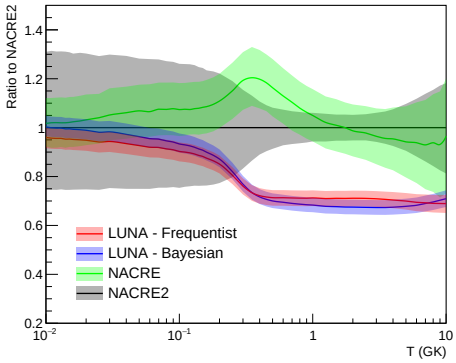

Figure A.8: The calculated reaction rate for the fit with both the approaches compared with NACRE and NACRE2 values.

The results for both the methods are quite similar. The reduced χ^2 for the final fit amounts to 0.84, which indicates that the new data are very well described by the R-matrix model. The $\Delta E_{\text{Rolfs High}}$ in each procedure is found to be (24 ± 1) keV. By using the correlation matrix it is possible to observe how the different datasets influence the results. More importantly, the γ-width, Γ_γ, of the first resonance is dominated by the new datasets. All the normalization factors are highly correlated with each other. The energy of the resonances are highly driven by both the proton scattering data and the new dataset. On the contrary the Rolfs and Azuma [21] data have rather low effect on it. Additionally, there is one striking difference between the two methods. In the Bayesian procedure the energies of the second and third resonance seems highly correlated, which is not true in the frequentist approach. In general, many of the correlations are lower in the frequentist case due probably to the fact that the minimization stuck in one minimum instead the Bayesian approach seems to explore much better all the parameter space. Finally, the reaction rate uncertainty is drastically reduced with respect to the literature values for both the methods.

A.3 $^{13}\mathbf{C}(\mathrm{p},\gamma)^{14}\mathbf{N}$ Reaction

In case of the $^{13}\mathrm{C}(\mathrm{p},\gamma)^{14}\mathrm{N}$ reaction, the situation is more complicated. There are six different γ-ray transitions to be considered and two broad resonances at approximately 550 keV and 1342 keV which corresponds, respectively, to the (8062 ± 1) keV and (8776 ± 7) keV excited states in ^{14}N nuclei. The only complete study of all the transitions has been done by King et al. [27] where the data covers only the first resonance. All the other studies concentrated on the transition to the ground state, being the dominant one. Of these, only the Genard et al. [29] study reports a slightly different normalization, approximately 15 % lower. For what regards the resonance energy, a small offset is present between the King et al. [27] study and the Vogl [20] one. The literature values for the state at 8062 keV are reported in Tab. A.11. The second broad resonance at around 1342 keV was studied only in Zeps et al. [28], but the data are not normalized and must be used as shape data only. The literature values are reported in Tab. A.12. At higher energies, there are present many narrow resonances, which contribution seems not to be dominant on the reaction rate. Their values are reported in Tab. A.13. For what regards the ANC parameters, two extensive studies have been made, namely the Artemov et al. [72] and Mukhamedzhanov et al. [73], mostly in agreement with each other, shown in Tab. A.14. These were used in the most recent R-matrix

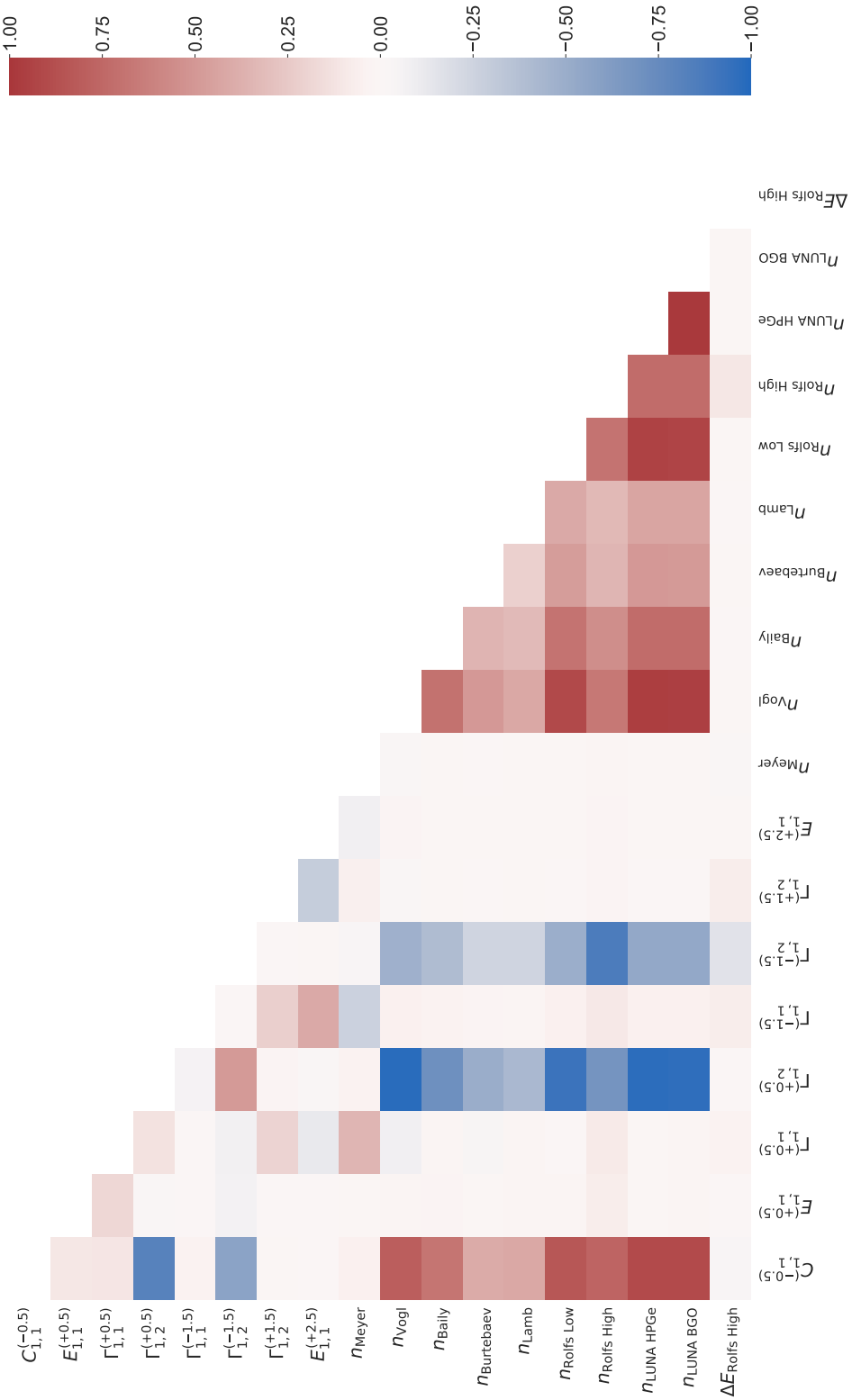

Figure A.9: The correlation matrix for the $^{12}C(p,\gamma)^{13}N$ R-matrix fit with the frequentist approach.

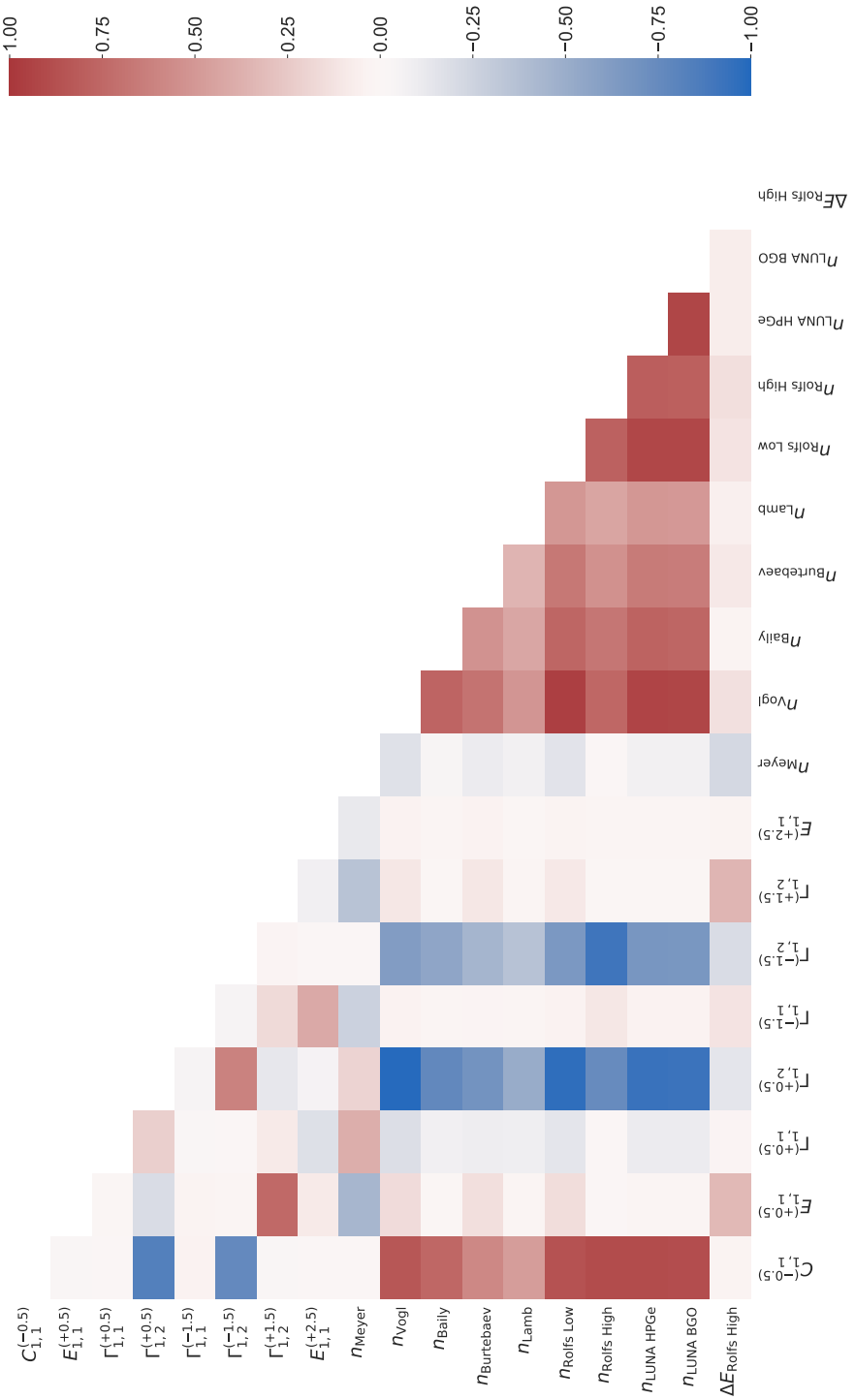

Figure A.10: The correlation matrix for the $^{12}C(p,\gamma)^{13}N$ R-matrix fit with the Bayesian approach.

analysis done in Chakraborty et al. [74], where two different background poles (0^- and 1^-) had to be included to reproduced the ANC values from the literature. Finally, the elastic scattering data are scarce: the only ones that cover the low energy resonance are the Hebbard and Vogl [75] and Milne [76] ones. The most recent study, namely Latorre and Irvine [77], only covers the energy range above 1 MeV, whereas it is the low lying resonance that dominates the reaction rate.

Reference	E_r (keV)	Γ_p (keV)	Γ_γ (eV)						
			R → Total	R → 0 keV	R → 2312 keV	R → 3948 keV	R → 4915 keV	R → 5105 keV	R → 5691 keV
Seagrave [24]	550 ± 1	32.5 ± 1							
Hebbard and Vogl [75]	550 ± 1								
Vogl [20]	555 ± 1.5								
Galster et al. [78]	551.5 ± 1.2	33.8 ± 1.2	11.3 ± 1.6	9.0 ± 1.3					
Ajzenberg-Selove [47]	551 ± 1	23 ± 1	12.3						
King et al. [27]	557.6 ± 0.5	40 ± 1							
Artemov et al. [72]	556	33.5 ± 1	11.67	9.2	0.22	1.53	0.265	0.077	0.6
Genard et al. [29]	557.5 ± 0.5	34.5 ± 1.1							
Chakraborty et al. [74]	557 ± 3	37.2 ± 0.3	11.80 ± 0.07	9.09 ± 0.05	0.22 ± 0.04	1.544 ± 0.009	0.26 ± 0.01	0.074 ± 0.008	0.612 ± 0.006

Table A.11: Literature parameters for the state at 8062 keV.

Reference	E_r (keV)	Γ_p (keV)	Γ_γ (eV)				
			R → Total	R → 0 eV	R → 3948 eV	R → 5105 eV	R → 5691 eV
Ajzenberg-Selove [47]	1320 ± 7	410 ± 20	51.2				
Zeps et al. [28]	1347 ± 7	440 ± 8	25.2 ± 2				
Chakraborty et al. [74]	1347	460	41.97	40.96	0.556	0.23	0.23

Table A.12: Literature parameters for the state at 8776 keV.

A.3.1 Literature Sampling

The parameters from the Chakraborty et al. [74] study were used and sampled considering normal distributions for each parameter. Since no uncertainty for the ANCs is reported, the values from Mukhamedzhanov et al. [73] were used by converting the data from *JJ* coupling scheme to *LS* one with the Wigner's 6-*j* symbols. Additionally, since the reported resonance values do not include the systematic uncertainty, i.e. during the fitting procedure the data normalization was not varied, the 11.3 % reported by the King et al. [27] was added to each resonance parameter, analogously to what have been done in Chakraborty et al. [74]. All the narrow resonances were excluded from the fit, assuming that their effect on the extrapolation is negligible and that their contribution to the reaction rate, R_i, can be calculated with their resonance strength, $\omega\gamma_i$, as follows:

$$R_i = \frac{1.54 \times 10^{11}}{T_9^{3/2}} \left(\frac{M_p + M_{^{13}\mathrm{C}}}{M_p M_{^{13}\mathrm{C}}} \right)^{3/2} \omega\gamma_i \exp\left(-11.605 \frac{E_i}{T_9} \right) \tag{A.4}$$

Reference	E_r (keV)	Γ_p (keV)	$\omega\gamma$ (eV)
Ajzenberg-Selove [47]	448.5 ± 0.5	< 0.37	0.022
	1012 ± 2	< 0.2	0.01
	1152 ± 2	3.8 ± 0.3	1.3
	1462 ± 3	16.2 ± 2	0.67 ± 0.07
	1523 ± 2	< 1	0.003
	1540 ± 3	8 ± 2	0.13
	1700.5 ± 1	< 1	
	1747.6 ± 0.9	0.135 ± 0.008	9.1 ± 0.5
	1980 ± 3	13 ± 3	
	2110 ± 3	41 ± 2	7 ± 1
	2319 ± 4	15 ± 3	0.11 ± 0.01
	2743	12 ± 3	0.37 ± 0.03
	3105 ± 5	33 ± 3	22.8 ± 1.3
Zeps et al. [28]	1156 ± 2	4.0 ± 0.3	1.03 ± 0.07
	1462 ± 3	16.2 ± 2	0.72
	1523 ± 2	8 ± 2	0.13
	1747.6 ± 0.9	0.135 ± 0.008	9.2 ± 0.6

Table A.13: Literature parameters for narrow resonances.

Reference	ANC ($\mathrm{fm}^{-1/2}$)								
	0 keV ($s=0$)	0 keV ($s=1$)	2312 keV	3948 keV ($s=0$)	3948 keV ($s=1$)	4915 keV	5105 keV ($s=0$)	5105 keV ($s=1$)	5691 keV
Mukhamedzhanov et al. [73][a]	1.68 ± 0.12	4.03 ± 0.13	2.98 ± 0.15	0.98 ± 0.03	1.39 ± 0.04	5.74 ± 0.33	0.49 ± 0.02	0.40 ± 0.02	3.21 ± 0.11
Artemov et al. [72][a]	1.61 ± 0.24	3.84 ± 0.30	3.49 ± 0.27	0.84 ± 0.06	1.19 ± 0.09	3.69 ± 0.16	0.59 ± 0.04	0.49 ± 0.03	
Chakraborty et al. [74][b]	1.37 (1.98)	3.99 (1.78)	2.97 (3.32)	0.85 (0.81)	1.24 (1.01)	6.03 (5.26)	0.69 (0.74)	0.34 (0.01)	4.71 (6.04)

[a] The ANC are provided in JJ scheme, they were converted to LS scheme
[b] The values correspond to the fit with (without) background poles

Table A.14: Literature ANC parameters.

where T_9 is the temperature in giga Kelvin, M_p and $M_{^{13}C}$ are respectively the proton and ^{13}C masses in amu unit, and E_i is the energy of the resonance.

The results of the sampling are showed in Fig. A.11 - A.14. A good agreement, within the uncertainties, was found for both the extrapolation and the reaction rate. The slightely difference in the latter is due to the new ANCs values, as observed in the Chakraborty et al. [74].

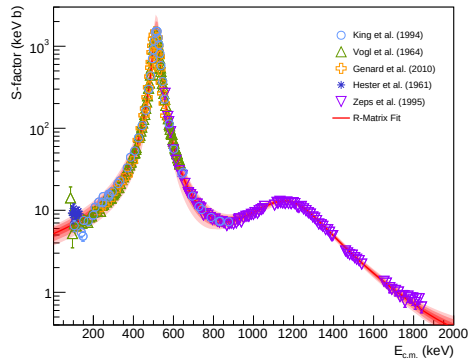

Figure A.11: The literature S-factor for the transition to the gs state and the extrapolation obtained with the literature parameters.

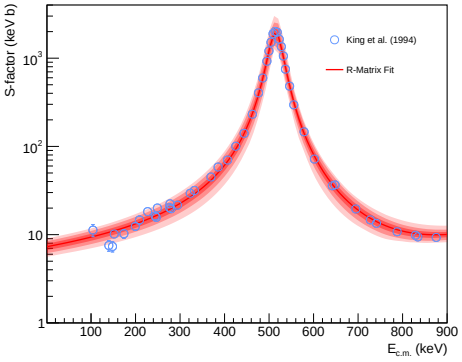

Figure A.12: The total literature S-factor and the extrapolation obtained with the literature parameters.

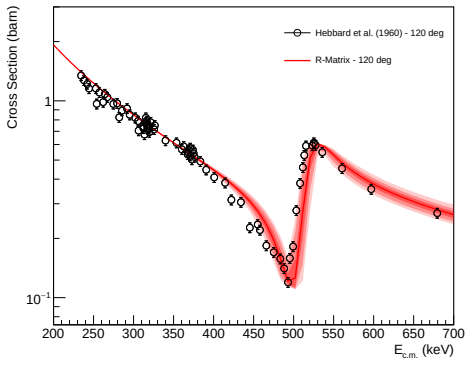

Figure A.13: The literature elastic scattering cross-section and the extrapolation obtained with the literature parameters.

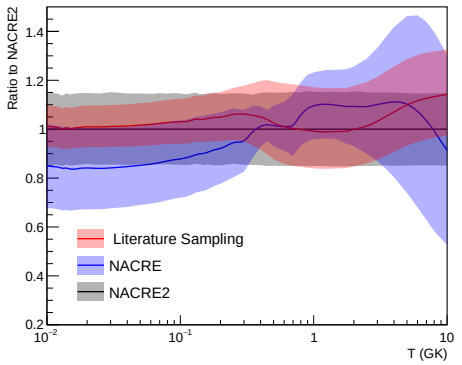

Figure A.14: The calculated reaction rate for the literature parameters compared with NACRE and NACRE2 values.

A.3.2 Fit

The new LUNA data were added and the fit was constructed. First of all, only the [27] and [28] data were considered for the (p,γ) channel. The former one represent

the only comprehensive study for all the transitions. The latter, instead, is the only measurement above the lowest lying resonance. In the fit, no background pole was considered. This is due to the fact the data are well described without them and the resonance at 1347 keV is quite sensitive to their presence by interfering: since the [28] are shape-only, when adding the background poles a value close to the [74] is found for the γ-width for the resonance, which is almost double of what the original study reports.

The results can be seen in Fig. A.15 - A.18 and the best-fit parameters are showed in Tab. A.15 - A.19. The correlation matrices can be seen in Fig. A.19 - A.20. In case of the Bayesian procedure no energy shift was considered due to the fact that it implies the recalculation of external capture integrals at each step of the minimization. This is computationally expensive given the much higher number of transitions being considered with respect to the $^{12}\mathrm{C}(\mathrm{p},\gamma)^{13}\mathrm{N}$ case. For the frequentist fit, the uncertainty of the literature data was inflated according to their contribution to the reduced χ^2 given in the literature fit, since the [27] data always resulted with reduced χ^2 higher than 1. On the other hand, the new datasets did not increased the χ^2 significantly.

Both the approaches seems to give consistent results. The Bayesian procedure seems to show slightly lower rate at the lowest temperatures because the normalization constants for the LUNA data are lower, ie. it prefers to give more importance to the new data. In the frequentist approach, instead, the normalizations are slightely closer to [27] values. Nevertheless, the two results are still in agreement within the uncertainty and much improved w.r.t. the literature values. Moreover, the reduced χ^2 values for the new datasets confirms the quality of the new data and their power in describing the theory. The 1342 keV resonance gives much more similar values to what was reported in [28] with respect to the Chakraborty et al. [74] value. Finally, as in the $^{12}\mathrm{C}(\mathrm{p},\gamma)^{13}\mathrm{N}$ case, the Bayesian approach shows higher correlation between the parameters with respect to the frequentist approach.

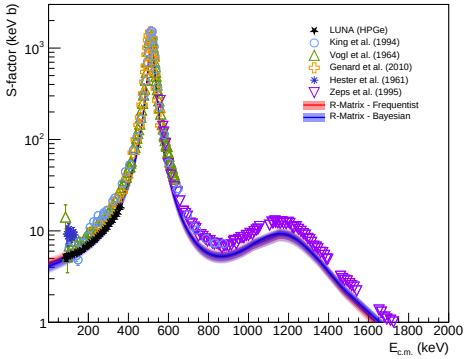

Figure A.15: The S-factor for the transition to the gs state and the fit result with both the approaches.

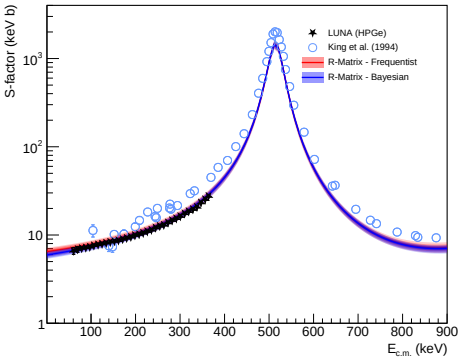

Figure A.16: The total literature S-factor and the fit result with both the approaches.

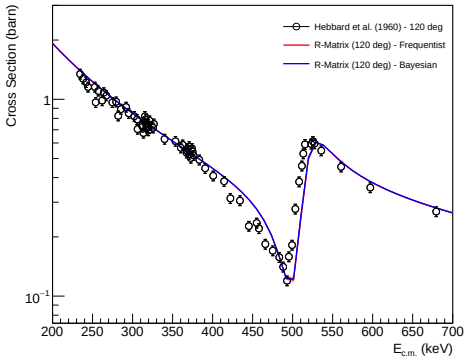

Figure A.17: The literature elastic scattering cross-section and the fit result with both the approaches.

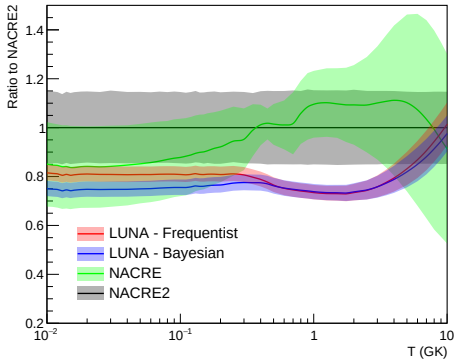

Figure A.18: The calculated reaction rate for the fit both the approaches compared with NACRE and NACRE2 values.

Reference	E_r (keV)	Γ_p (keV)	Γ_γ (eV)					
			R $\to$ 0 keV	R $\to$ 2312 keV	R $\to$ 3948 keV	R $\to$ 4915 keV	R $\to$ 5105 keV	R $\to$ 5691 keV
Literature	557 ± 3	37.2 ± 0.3	9.09 ± 0.05	0.22 ± 0.04	1.544 ± 0.009	0.26 ± 0.01	0.074 ± 0.008	0.612 ± 0.006
Frequentist	557.2 ± 0.2	36.5 ± 0.3	6.26 ± 0.32	0.14 ± 0.02	1.36 ± 0.08	0.26 ± 0.02	0.047 ± 0.004	0.51 ± 0.03
Bayesian	557.3 ± 0.1	36.7 ± 0.2	6.31 ± 0.36	0.14 ± 0.01	1.40 ± 0.09	0.23 ± 0.01	0.050 ± 0.006	0.49 ± 0.03

Table A.15: The 8062 keV resonance parameters for the fit of the $^{13}C(p,\gamma)^{14}N$.

Reference	E_r (keV)	Γ_p (keV)	Γ_γ (eV)			
			R $\to$ 0 eV	R $\to$ 3948 eV	R $\to$ 5105 eV	R $\to$ 5691 eV
Literature	1347	460	40.96	0.556	0.23	0.23
Frequentist	1380 ± 6	500 ± 13	30 ± 2	4.8 ± 2.4	0.7 ± 0.7	2.5 ± 0.9
Bayesian	1371 ± 8	500 ± 6	30 ± 2	0.6 ± 0.4	0.8 ± 0.3	1.8 ± 0.02

Table A.16: The 8776 keV resonance parameters for the literature fit of the $^{13}C(p,\gamma)^{14}N$.

Source	ANC ($fm^{-1/2}$)								
	0 keV ($s=0$)	0 keV ($s=1$)	2312 keV	3948 keV ($s=0$)	3948 keV ($s=1$)	4915 keV	5105 keV ($s=0$)	5105 keV ($s=1$)	5691 keV
Literature	1.68 ± 0.12	4.03 ± 0.13	2.98 ± 0.15	0.98 ± 0.03	1.39 ± 0.04	5.74 ± 0.33	0.49 ± 0.02	0.40 ± 0.02	3.21 ± 0.11
Frequentist	3.33 ± 0.27	3.03 ± 0.19	2.82 ± 0.17	2.61 ± 0.34	1.16 ± 0.09	4.26 ± 0.16	0.67 ± 0.12	0 ± 3	3.28 ± 0.11
Bayesian	2.50 ± 0.23	2.70 ± 0.14	2.62 ± 0.13	0.85 ± 0.39	1.20 ± 0.06	4.58 ± 0.06	0.57 ± 0.07	0.25 ± 0.07	3.34 ± 0.11

Table A.17: The ANC parameters for the literature fit of the $^{13}C(p,\gamma)^{14}N$.

Source	n_{Hebbard}	$n_{\text{King 0}}$	$n_{\text{King 2312}}$	$n_{\text{King 3948}}$	$n_{\text{King 4915}}$	$n_{\text{King 5105}}$	$n_{\text{King 5691}}$	n_{Zeps}	$n_{\text{LUNA 0}}$	$n_{\text{LUNA 2312}}$	$n_{\text{LUNA 3948}}$	$n_{\text{LUNA 4915}}$	$n_{\text{LUNA 5105}}$	$n_{\text{LUNA 5691}}$	$n_{\text{LUNA Tot}}$
Frequentist	1.04 ± 0.02	0.69 ± 0.04	0.75 ± 0.07	0.89 ± 0.05	0.93 ± 0.06	0.83 ± 0.08	0.83 ± 0.05	0.037 ± 0.002	1.06 ± 0.06	1.07 ± 0.06	1.03 ± 0.06	1.03 ± 0.06	1.05 ± 0.07	1.05 ± 0.06	1.05 ± 0.04
Bayesian	1.04 ± 0.02	0.69 ± 0.04	0.65 ± 0.05	0.92 ± 0.06	0.86 ± 0.04	0.73 ± 0.06	0.81 ± 0.06	0.038 ± 0.002	1.03 ± 0.06	0.99 ± 0.06	1.00 ± 0.06	1.04 ± 0.04	1.04 ± 0.07	1.05 ± 0.07	1.03 ± 0.04

Table A.18: The normalization parameters for the literature fit of the $^{13}C(p,\gamma)^{14}N$.

Source	χ^2_{dof}	Source	χ^2_{dof}
Hebbard	0.15	LUNA 0	0.01
King 0	0.09	LUNA 2312	0.02
King 2312	0.01	LUNA 3948	0.02
King 3948	0.11	LUNA 4915	0.04
King 4915	0.11	LUNA 5105	0.03
King 5105	0.02	LUNA 5691	0.01
King 5691	0.02	LUNA Total	0.01
Zeps	0.07		

Table A.19: Reduced χ^2 values for the fit of the $^{13}C(p,\gamma)^{14}N$.

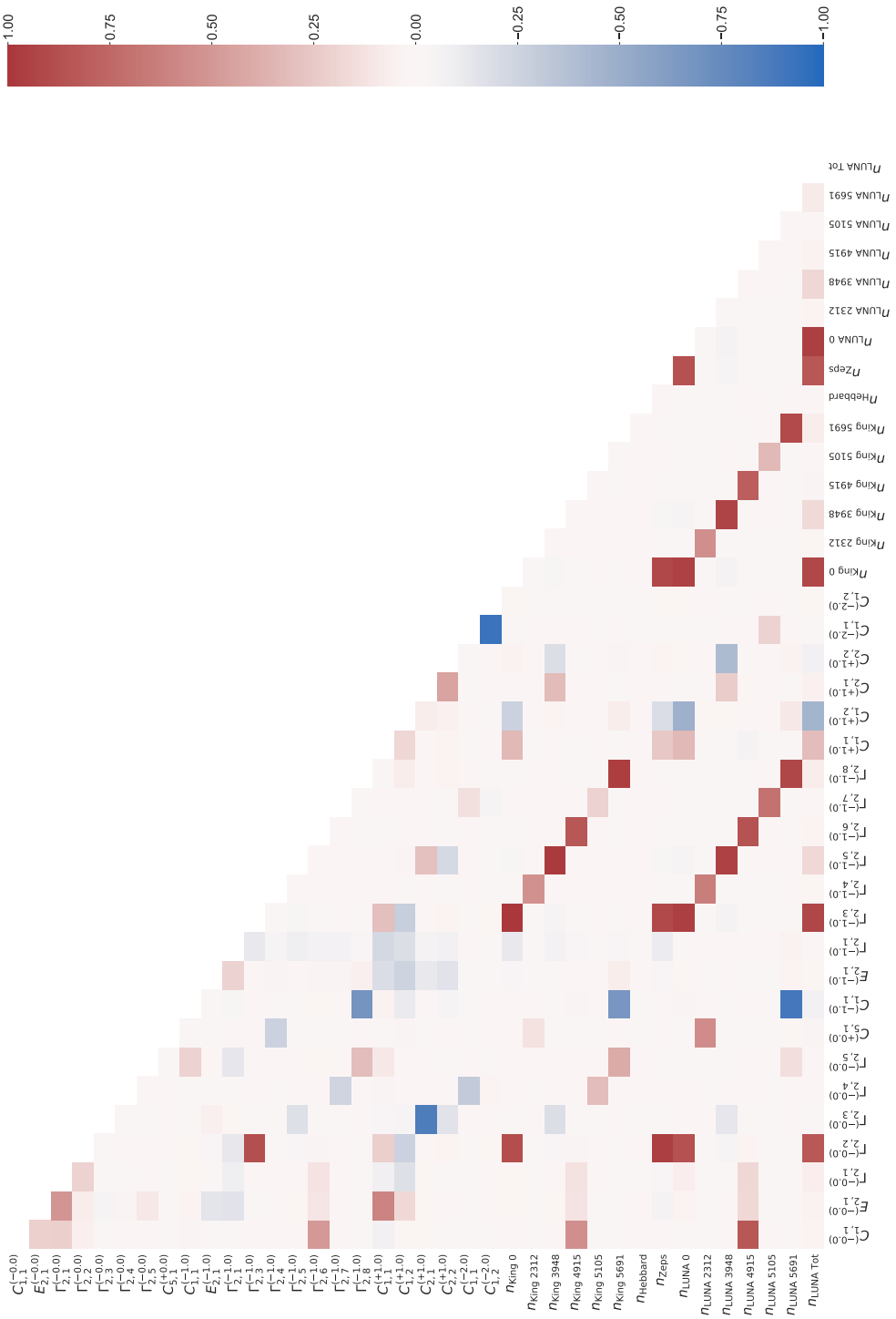

Figure A.19: The correlation matrix for the $^{12}C(p,\gamma)^{13}N$ R-matrix fit with the frequentist approach.

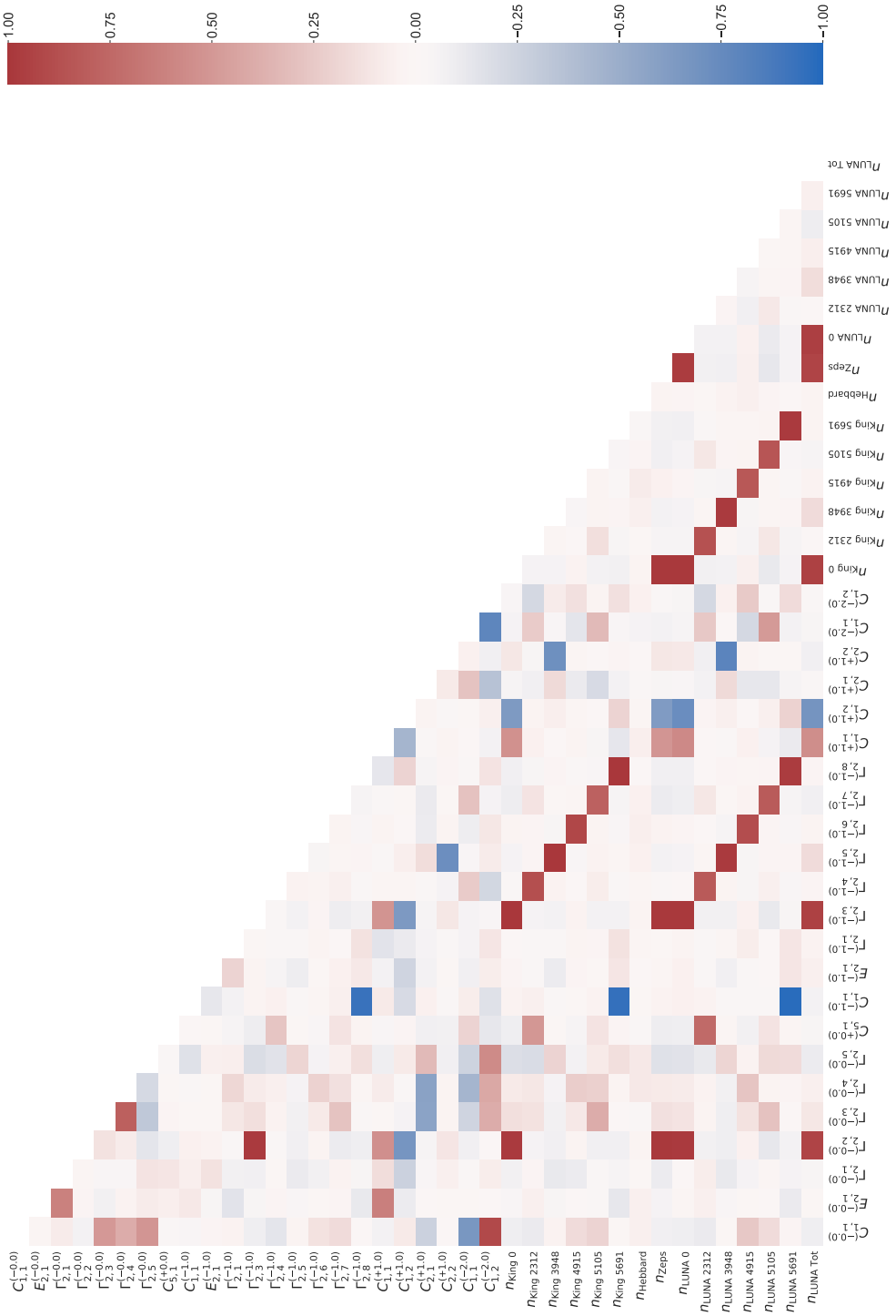

Figure A.20: The correlation matrix for the $^{12}C(p,\gamma)^{13}N$ R-matrix fit with the bayesian approach.

Bibliography

[1] Christian Iliadis. *Nuclear Physics of Stars*. Wiley-VCH, 2007. ISBN 9783527406029.

[2] Frank Timmes. `https://cococubed.com/code_pages/burn_hydrogen.shtml`, 2023. [Online; accessed 23-June-2023].

[3] Falk Herwig. Evolution of Asymptotic Giant Branch Stars. ARA&A, 43(1): 435–479, September 2005. doi: 10.1146/annurev.astro.43.072103.150600.

[4] S. Uttenthaler, I. McDonald, K. Bernhard, S. Cristallo, and D. Gobrecht. Interplay between pulsation, mass loss, and third dredge-up: More about Miras with and without technetium. A&A, 622:A120, February 2019. doi: 10.1051/0004-6361/201833794.

[5] Maria Lugaro, Amanda I. Karakas, and Sara Bisterzo. Models and observations of the s process in agb stars. 2008. URL `https://api.semanticscholar.org/CorpusID:1839849`.

[6] László Szigeti, Szabolcs Mészáros, Verne V. Smith, Katia Cunha, Nadège Lagarde, Corinne Charbonnel, D. A. García-Hernández, Matthew Shetrone, Marc Pinsonneault, Carlos Allende Prieto, J. G. Fernández-Trincado, József Kovács, and Sandro Villanova. $^{12}C/^{13}C$ isotopic ratios in red-giant stars of the open cluster NGC 6791. MNRAS, 474(4):4810–4817, March 2018. doi: 10.1093/mnras/stx3027.

[7] C. Charbonnel and N. Lagarde. Thermohaline instability and rotation-induced mixing. I. Low- and intermediate-mass solar metallicity stars up to the end of the AGB. A&A, 522:A10, November 2010. doi: 10.1051/0004-6361/201014432.

[8] Maurizio Busso, Gerald J. Wasserburg, Kenneth M. Nollett, and Andrea

Calandra. Can Extra Mixing in RGB and AGB Stars Be Attributed to Magnetic Mechanisms? ApJ, 671(1):802–810, December 2007. doi: 10.1086/522616.

[9] Diego Vescovi, Sergio Cristallo, Maurizio Busso, and Nan Liu. Magnetic-buoyancy-induced Mixing in AGB Stars: Presolar SiC Grains. ApJ, 897(2):L25, July 2020. doi: 10.3847/2041-8213/ab9fa1.

[10] N. Langer, A. Heger, S. Wellstein, and F. Herwig. Mixing and nucleosynthesis in rotating TP-AGB stars. A&A, 346:L37–L40, June 1999. doi: 10.48550/arXiv.astro-ph/9904257.

[11] S. Palmerini, M. La Cognata, S. Cristallo, and M. Busso. Deep Mixing in Evolved Stars. I. The Effect of Reaction Rate Revisions from C to Al. ApJ, 729(1):3, March 2011. doi: 10.1088/0004-637X/729/1/3.

[12] R. P. Hedrosa, C. Abia, M. Busso, S. Cristallo, I. Domínguez, S. Palmerini, B. Plez, and O. Straniero. Nitrogen Isotopes in Asymptotic Giant Branch Carbon Stars and Presolar SiC Grains: A Challenge for Stellar Nucleosynthesis. ApJ, 768(1):L11, May 2013. doi: 10.1088/2041-8205/768/1/L11.

[13] Nan Liu, Jens Barosch, Larry R. Nittler, Conel M. O'D. Alexander, Jianhua Wang, Sergio Cristallo, Maurizio Busso, and Sara Palmerini. New Multielement Isotopic Compositions of Presolar SiC Grains: Implications for Their Stellar Origins. ApJ, 920(1):L26, October 2021. doi: 10.3847/2041-8213/ac260b.

[14] S. N. Milam, C. Savage, M. A. Brewster, L. M. Ziurys, and S. Wyckoff. The $^{12}C/^{13}C$ Isotope Gradient Derived from Millimeter Transitions of CN: The Case for Galactic Chemical Evolution. ApJ, 634(2):1126–1132, December 2005. doi: 10.1086/497123.

[15] Maurizio Salaris, Santi Cassisi, and Achim Weiss. Red Giant Branch Stars: The Theoretical Framework. *Publications of the Astronomical Society of the Pacific*, 114(794):375–402, April 2002. doi: 10.1086/342498.

[16] A. Slemer, P. Marigo, D. Piatti, M. Aliotta, D. Bemmerer, A. Best, A. Boeltzig, A. Bressan, C. Broggini, C. G. Bruno, A. Caciolli, F. Cavanna, G. F. Ciani, P. Corvisiero, T. Davinson, R. Depalo, A. Di Leva, Z. Elekes, F. Ferraro, A. Formicola, Zs. Fülöp, G. Gervino, A. Guglielmetti,

C. Gustavino, G. Gyürky, G. Imbriani, M. Junker, R. Menegazzo, V. Mossa, F. R. Pantaleo, P. Prati, O. Straniero, T. Szücs, M. P. Takács, and D. Trezzi. ^{22}Ne and ^{23}Na ejecta from intermediate-mass stars: the impact of the new LUNA rate for ^{22}Ne(p, γ)^{23}Na. *Monthly Notices of the Royal Astronomical Society*, 465(4):4817–4837, March 2017. doi: 10.1093/mnras/stw3029.

[17] M.B. Chadwick, P. Obložinský, M. Herman, N.M. Greene, R.D. McKnight, D.L. Smith, P.G. Young, R.E. MacFarlane, G.M. Hale, S.C. Frankle, A.C. Kahler, T. Kawano, R.C. Little, D.G. Madland, P. Moller, R.D. Mosteller, P.R. Page, P. Talou, H. Trellue, M.C. White, W.B. Wilson, R. Arcilla, C.L. Dunford, S.F. Mughabghab, B. Pritychenko, D. Rochman, A.A. Sonzogni, C.R. Lubitz, T.H. Trumbull, J.P. Weinman, D.A. Brown, D.E. Cullen, D.P. Heinrichs, D.P. McNabb, H. Derrien, M.E. Dunn, N.M. Larson, L.C. Leal, A.D. Carlson, R.C. Block, J.B. Briggs, E.T. Cheng, H.C. Huria, M.L. Zerkle, K.S. Kozier, A. Courcelle, V. Pronyaev, and S.C. van der Marck. ENDF/B-VII.0: Next generation evaluated nuclear data library for nuclear science and technology. *Nuclear Data Sheets*, 107(12):2931–3118, December 2006. doi: 10.1016/j.nds.2006.11.001. URL `https://www.sciencedirect.com/science/journal/00903752`.

[18] Robert Noel Hall and William Alfred Fowler. The Cross Section for the Radiative Capture of Protons by C^{12} near 100 Kev. *Physical Review*, 77(2): 197–204, January 1950. doi: 10.1103/PhysRev.77.197.

[19] Carl L. Bailey and William R. Stratton. Cross Section of the C^{12}(p,γ)N^{13} Reaction at Low Energies. *Physical Review*, 77(2):194–196, January 1950. doi: 10.1103/PhysRev.77.194.

[20] J. L. Vogl. *Radiative capture of protons by ^{12}C and ^{13}C below 700 keV*. PhD thesis, California Institute of Technology, January 1963.

[21] C. Rolfs and R. E. Azuma. Interference effects in ^{12}C(p, γ) ^{13}N and direct capture to unbound states. *Nucl. Phys. A*, 227(2):291–308, July 1974. doi: 10.1016/0375-9474(74)90798-2.

[22] N. Burtebaev, S. B. Igamov, R. J. Peterson, R. Yarmukhamedov, and D. M. Zazulin. New measurements of the astrophysical S factor for ^{12}C(p,γ)^{13}N reaction at low energies and the asymptotic normalization coefficient (nuclear vertex constant) for the p+^{12}C$\rightarrow^{13}$N reaction. *Phys. Rev. C*, 78(3): 035802, September 2008. doi: 10.1103/PhysRevC.78.035802.

[23] Gy. Gyürky, L. Csedreki, T. Szücs, G. G. Kiss, Z. Halász, and Zs. Fülöp. Cross section measurement of the 1^2C(p,γ)1^3N reaction with activation in a wide energy range. *European Physical Journal A*, 59(3):59, March 2023. doi: 10.1140/epja/s10050-023-00974-0.

[24] John D. Seagrave. Radiative Capture of Protons by C^{13}. *Physical Review*, 85 (2):197–203, January 1952. doi: 10.1103/PhysRev.85.197.

[25] Eric John Woodbury and William Alfred Fowler. The Cross Section for the Radiative Capture of Protons by C^{13} at 129 kev. *Physical Review*, 85(1): 51–57, January 1952. doi: 10.1103/PhysRev.85.51.

[26] Ross E. Hester and W. A. Lamb. Radiative Capture of Protons in C^{13}. *Physical Review*, 121(2):584–586, January 1961. doi: 10.1103/PhysRev.121.584.

[27] J. D. King, R. E. Azuma, J. B. Vise, J. Görres, C. Rolfs, H. P. Trautvetter, and A. E. Vlieks. Cross section and astrophysical S-factor for the ^{13}C(p, γ)^{14}N reaction. *Nuclear Physics A*, 567(2):354–376, January 1994. doi: 10.1016/0375-9474(94)90154-6.

[28] V. J. Zeps, E. G. Adelberger, A. García, C. A. Gossett, H. E. Swanson, W. Haeberli, P. A. Quin, and J. Sromicki. Parity mixing of the 0^+-0^- I=1 doublet in ^{14}N. *Phys. Rev. C*, 51(3):1494–1520, March 1995. doi: 10.1103/PhysRevC.51.1494.

[29] G. Genard, P. Descouvemont, and G. Terwagne. S-factor measurement of the ^{13}C(p,γ)^{14}N reaction in reverse kinematics. In *Journal of Physics Conference Series*, volume 202 of *Journal of Physics Conference Series*, page 012015, January 2010. doi: 10.1088/1742-6596/202/1/012015.

[30] C. Broggini, D. Bemmerer, A. Caciolli, and D. Trezzi. LUNA: Status and prospects. *Progress in Particle and Nuclear Physics*, 98:55–84, 2018. ISSN 0146-6410. doi: 10.1016/j.ppnp.2017.09.002.

[31] A. Formicola, G. Imbriani, M. Junker, D. Bemmerer, R. Bonetti, C. Broggini, C. Casella, P. Corvisiero, H. Costantini, G. Gervino, C. Gustavino, A. Lemut, P. Prati, V. Roca, C. Rolfs, M. Romano, D. Schürmann, F. Strieder, F. Terrasi, H. P. Trautvetter, and S. Zavatarelli. The LUNA II 400 kV accelerator. *Nuclear Instruments and Methods in*

Physics Research A, 507(3):609–616, July 2003. doi: 10.1016/S0168-9002(03)01435-9.

[32] G. F. Ciani, L. Csedreki, J. Balibrea-Correa, A. Best, M. Aliotta, F. Barile, D. Bemmerer, A. Boeltzig, C. Broggini, C. G. Bruno, A. Caciolli, F. Cavanna, T. Chillery, P. Colombetti, P. Corvisiero, T. Davinson, R. Depalo, A. Di Leva, L. Di Paolo, Z. Elekes, F. Ferraro, E. M. Fiore, A. Formicola, Zs. Fülöp, G. Gervino, A. Guglielmetti, C. Gustavino, Gy. Gyürky, G. Imbriani, M. Junker, I. Kochanek, M. Lugaro, P. Marigo, E. Masha, R. Menegazzo, V. Mossa, F. R. Pantaleo, V. Paticchio, R. Perrino, D. Piatti, P. Prati, L. Schiavulli, K. Stöckel, O. Straniero, T. Szücs, M. P. Takács, F. Terrasi, D. Trezzi, and S. Zavatarelli. A new approach to monitor ^{13}C-targets degradation in situ for $^{13}C(\alpha, n)^{16}O$ cross-section measurements at LUNA. *European Physical Journal A*, 56(3): 75, March 2020. doi: 10.1140/epja/s10050-020-00077-0.

[33] Gordon R. Gilmore. *Practical Gamma-ray Spectroscopy*. John Wiley & Sons Inc, 2008. ISBN 0470861967.

[34] Ch. Iliadis, Th. Schange, C. Rolfs, U. Schröder, E. Somorjai, H. P. Trautvetter, K. Wolke, P. M. Endt, S. W. Kikstra, A. E. Champagne, M. Arnould, and G. Paulus. Low-energy resonances in ^{25}Mg(p, γ)^{26}Al, ^{26}Mg(p, γ)^{27}Al and ^{27}Al(p, γ)^{28}Si. *Nuclear Physics A*, 512(3):509–530, June 1990. doi: 10.1016/0375-9474(90)90084-Y.

[35] G. Imbriani, H. Costantini, A. Formicola, A. Vomiero, C. Angulo, D. Bemmerer, R. Bonetti, C. Broggini, F. Confortola, P. Corvisiero, J. Cruz, P. Descouvemont, Z. Fülöp, G. Gervino, A. Guglielmetti, C. Gustavino, Gy. Gyürky, A. P. Jesus, M. Junker, J. N. Klug, A. Lemut, R. Menegazzo, P. Prati, V. Roca, C. Rolfs, M. Romano, C. Rossi-Alvarez, F. Schümann, D. Schürmann, E. Somorjai, O. Straniero, F. Strieder, F. Terrasi, and H. P. Trautvetter. S-factor of ^{14}N(p,γ)^{15}O at astrophysical energies*. *European Physical Journal A*, 25(3):455–466, September 2005. doi: 10.1140/epja/i2005-10138-7.

[36] M. E. Rose. The Analysis of Angular Correlation and Angular Distribution Data. *Physical Review*, 91(3):610–615, August 1953. doi: 10.1103/PhysRev.91.610.

[37] S. Agostinelli, J. Allison, K. Amako, J. Apostolakis, H. Araujo, P. Arce,

M. Asai, D. Axen, S. Banerjee, G. Barrand, F. Behner, L. Bellagamba, J. Boudreau, L. Broglia, A. Brunengo, H. Burkhardt, S. Chauvie, J. Chuma, R. Chytracek, G. Cooperman, G. Cosmo, P. Degtyarenko, A. Dell'Acqua, G. Depaola, D. Dietrich, R. Enami, A. Feliciello, C. Ferguson, H. Fesefeldt, G. Folger, F. Foppiano, A. Forti, S. Garelli, S. Giani, R. Giannitrapani, D. Gibin, J.J. Gómez Cadenas, I. González, G. Gracia Abril, G. Greeniaus, W. Greiner, V. Grichine, A. Grossheim, S. Guatelli, P. Gumplinger, R. Hamatsu, K. Hashimoto, H. Hasui, A. Heikkinen, A. Howard, V. Ivanchenko, A. Johnson, F.W. Jones, J. Kallenbach, N. Kanaya, M. Kawabata, Y. Kawabata, M. Kawaguti, S. Kelner, P. Kent, A. Kimura, T. Kodama, R. Kokoulin, M. Kossov, H. Kurashige, E. Lamanna, T. Lampén, V. Lara, V. Lefebure, F. Lei, M. Liendl, W. Lockman, F. Longo, S. Magni, M. Maire, E. Medernach, K. Minamimoto, P. Mora de Freitas, Y. Morita, K. Murakami, M. Nagamatu, R. Nartallo, P. Nieminen, T. Nishimura, K. Ohtsubo, M. Okamura, S. O'Neale, Y. Oohata, K. Paech, J. Perl, A. Pfeiffer, M.G. Pia, F. Ranjard, A. Rybin, S. Sadilov, E. Di Salvo, G. Santin, T. Sasaki, N. Savvas, Y. Sawada, S. Scherer, S. Sei, V. Sirotenko, D. Smith, N. Starkov, H. Stoecker, J. Sulkimo, M. Takahata, S. Tanaka, E. Tcherniaev, E. Safai Tehrani, M. Tropeano, P. Truscott, H. Uno, L. Urban, P. Urban, M. Verderi, A. Walkden, W. Wander, H. Weber, J.P. Wellisch, T. Wenaus, D.C. Williams, D. Wright, T. Yamada, H. Yoshida, and D. Zschiesche. Geant4—a simulation toolkit. *Nuclear Instruments and Methods in Physics Research Section A: Accelerators, Spectrometers, Detectors and Associated Equipment*, 506(3):250–303, 2003. ISSN 0168-9002. doi: https://doi.org/10.1016/S0168-9002(03)01368-8. URL `https://www.sciencedirect.com/science/article/pii/S0168900203013688`.

[38] ¡author/D. Bemmerer, F. Cavanna, R. Depalo, M. Aliotta, M. Anders, A. Boeltzig, C. Broggini, C. Bruno, A. Caciolli, T. Chillery, P. Corvisiero, T. Davinson, Z. Elekes, F. Ferraro, A. Formicola, Zs. Fülöp, G. Gervino, A. Guglielmetti, C. Gustavino, Gy. Gyürky, R. Menegazzo, V. Mossa, F. R. Pantaleo, P. Prati, D. A. Scott, K. Stöcker, O. Straniero, T. Szücs, M. P. Takács, and D. Trezzi. Effect of beam energy straggling on resonant yield in thin gas targets: The cases ^{22}Ne(p, γ)^{23}Na and ^{14}N(p, γ)^{15}O. *EPL (Europhysics Letters)*, 122(5):52001, June 2018. doi: 10.1209/0295-5075/122/52001.

[39] W. K. Chu. Calculation of energy straggling for protons and helium ions.

Physical Review A, 13(6):2057–2060, June 1976. ISSN 0556-2791. doi: 10.1103/PhysRevA.13.2057. URL `https://link.aps.org/doi/10.1103/PhysRevA.13.2057`.

[40] Matej Mayer. Simnra user's guide. In *SIMNRA User's Guide*, 1997.

[41] E. Szilágyi, F. Pászti, and G. Amsel. Theoretical approximations for depth resolution calculations in IBA methods. *Nuclear Instruments and Methods in Physics Research Section B: Beam Interactions with Materials and Atoms*, 100(1):103–121, May 1995. ISSN 0168583X. doi: 10.1016/0168-583X(95)00186-7. URL `https://linkinghub.elsevier.com/retrieve/pii/0168583X95001867`.

[42] M. Hatlo, F. James, P. Mato, L. Moneta, M. Winkler, and A. Zsenei. Developments of Mathematical Software Libraries for the LHC Experiments. *IEEE Transactions on Nuclear Science*, 52(6):2818–2822, December 2005. doi: 10.1109/TNS.2005.860152.

[43] J. Ziegler. `SRIM` version 2008.04, http://www.srim.org. Software SRIM, 2008. URL `http://www.srim.org`.

[44] H. J. Assenbaum, K. Langanke, and C. Rolfs. Effects of electron screening on low-energy fusion cross sections. *Zeitschrift für Physik A*, 327(4):461–468, January 1987. doi: 10.1007/BF01289572.

[45] Martin Berger, J Hubbell, Stephen Seltzer, J Coursey, and D Zucker. Xcom: Photon cross section database (version 1.2), 1999-01-01 1999.

[46] A. Boeltzig, A. Best, G. Imbriani, M. Junker, M. Aliotta, D. Bemmerer, C. Broggini, C. G. Bruno, R. Buompane, A. Caciolli, F. Cavanna, T. Chillery, G. F. Ciani, P. Corvisiero, L. Csedreki, T. Davinson, R. J. deBoer, R. Depalo, A. Di Leva, Z. Elekes, F. Ferraro, E. M. Fiore, A. Formicola, Z. Fülöp, G. Gervino, A. Guglielmetti, C. Gustavino, G. Gyürky, I. Kochanek, R. Menegazzo, V. Mossa, F. R. Pantaleo, V. Paticchio, R. Perrino, D. Piatti, P. Prati, L. Schiavulli, K. Stöckel, O. Straniero, F. Strieder, T. Szücs, M. P. Takács, D. Trezzi, M. Wiescher, and S. Zavatarelli. Improved background suppression for radiative capture reactions at LUNA with HPGe and BGO detectors. *Journal of Physics G Nuclear Physics*, 45(2):025203, February 2018. doi: 10.1088/1361-6471/aaa163.

[47] F. Ajzenberg-Selove. Energy levels of light nuclei A = 13-15. *Nucl. Phys. A*, 523(1):1–196, February 1991. doi: 10.1016/0375-9474(91)90446-D.

[48] Wolfhard Möller. Hydrogen trapping and transport in carbon. *Journal of Nuclear Materials*, 162-164:138–150, 1989. ISSN 0022-3115. doi: https://doi.org/10.1016/0022-3115(89)90264-X. URL `https://www.sciencedirect.com/science/article/pii/002231158990264X`.

[49] Tamás Szücs, Daniel Bemmerer, Detlev Degering, Alexander Domula, Marcel Grieger, Felix Ludwig, Konrad Schmidt, Julia Steckling, Steffen Turkat, and Kai Zuber. Background in γ-ray detectors and carbon beam tests in the Felsenkeller shallow-underground accelerator laboratory. *European Physical Journal A*, 55(10):174, October 2019. doi: 10.1140/epja/i2019-12865-4.

[50] A. Antilla, J. Keinonen, M. Hautala, and I. Forsblom. Use of the ^{27}Al(p, γ) ^{28}Si, E_p = 992 keV resonance as a gamma-ray intensity standard. *Nuclear Instruments and Methods*, 147(3):501–505, December 1977. doi: 10.1016/0029-554X(77)90393-7.

[51] A. E. Richardson and W. W. Sallee. Coincidence summing corrections for positron emitters in germanium gamma spectrometry. *Nuclear Instruments and Methods in Physics Research A*, 299(1-3):344–348, December 1990. doi: 10.1016/0168-9002(90)90803-E.

[52] F. Papillon and P. Walter. Analytical use of the multiple gamma-rays from the ^{12}C(d,p) ^{13}C * nuclear reaction. *Nuclear Instruments and Methods in Physics Research B*, 132(3):468–480, November 1997. doi: 10.1016/S0168-583X(97)00438-2.

[53] K. U. Kettner, H. W. Becker, C. R. Brune, R. J. deBoer, J. Görres, D. Odell, D. Rogalla, and M. Wiescher. Absolute cross section of the ^{12}C(p ,γ)^{13}N reaction. *Phys. Rev. C*, 108(3):035805, September 2023. doi: 10.1103/PhysRevC.108.035805.

[54] A. M. Lane and R. G. Thomas. R-Matrix Theory of Nuclear Reactions. *Reviews of Modern Physics*, 30(2):257–353, April 1958. doi: 10.1103/RevModPhys.30.257.

[55] P. Descouvemont and D. Baye. The R-matrix theory. *Reports on Progress in Physics*, 73(3):036301, March 2010. doi: 10.1088/0034-4885/73/3/036301.

[56] Faïrouz Hammache and Nicolas de Séréville. Transfer reactions as a tool in Nuclear Astrophysics. *Frontiers in Physics*, 8:630, March 2021. doi: 10.3389/fphy.2020.602920.

[57] R. E. Azuma, E. Uberseder, E. C. Simpson, C. R. Brune, H. Costantini, R. J. de Boer, J. Görres, M. Heil, P. J. Leblanc, C. Ugalde, and M. Wiescher. AZURE: An R-matrix code for nuclear astrophysics. *Phys. Rev. C*, 81(4):045805, April 2010. doi: 10.1103/PhysRevC.81.045805.

[58] Daniel Odell, Carl R. Brune, Daniel R. Phillips, Richard James deBoer, and Som Nath Paneru. Performing Bayesian Analyses With AZURE2 Using BRICK: An Application to the 7Be System. *Frontiers in Physics*, 10:888476, June 2022. doi: 10.3389/fphy.2022.888476.

[59] G. D'Agostini. On the use of the covariance matrix to fit correlated data. *Nuclear Instruments and Methods in Physics Research A*, 346(1-2):306–311, July 1994. doi: 10.1016/0168-9002(94)90719-6.

[60] Rene Andrae, Tim Schulze-Hartung, and Peter Melchior. Dos and don'ts of reduced chi-squared, 2010. URL `https://arxiv.org/abs/1012.3754`.

[61] E. G. Adelberger, A. García, R. G. Hamish Robertson, K. A. Snover, A. B. Balantekin, K. Heeger, M. J. Ramsey-Musolf, D. Bemmerer, A. Junghans, C. A. Bertulani, J. W. Chen, H. Costantini, P. Prati, M. Couder, E. Uberseder, M. Wiescher, R. Cyburt, B. Davids, S. J. Freedman, M. Gai, D. Gazit, L. Gialanella, G. Imbriani, U. Greife, M. Hass, W. C. Haxton, T. Itahashi, K. Kubodera, K. Langanke, D. Leitner, M. Leitner, P. Vetter, L. Winslow, L. E. Marcucci, T. Motobayashi, A. Mukhamedzhanov, R. E. Tribble, Kenneth M. Nollett, F. M. Nunes, T. S. Park, P. D. Parker, R. Schiavilla, E. C. Simpson, C. Spitaleri, F. Strieder, H. P. Trautvetter, K. Suemmerer, and S. Typel. Solar fusion cross sections. II. The pp chain and CNO cycles. *Reviews of Modern Physics*, 83(1):195–246, January 2011. doi: 10.1103/RevModPhys.83.195.

[62] Daniel Foreman-Mackey, David W. Hogg, Dustin Lang, and Jonathan Goodman. emcee: The MCMC Hammer. *Publ. Astron. Soc. Pac.*, 125(925): 306, March 2013. doi: 10.1086/670067.

[63] C. Angulo, M. Arnould, M. Rayet, P. Descouvemont, D. Baye, C. Leclercq-Willain, A. Coc, S. Barhoumi, P. Aguer, C. Rolfs, R. Kunz, J. W. Hammer, A. Mayer, T. Paradellis, S. Kossionides, C. Chronidou,

K. Spyrou, S. degl'Innocenti, G. Fiorentini, B. Ricci, S. Zavatarelli, C. Providencia, H. Wolters, J. Soares, C. Grama, J. Rahighi, A. Shotter, and M. Lamehi Rachti. A compilation of charged-particle induced thermonuclear reaction rates. *Nucl. Phys. A*, 656(1):3–183, August 1999. doi: 10.1016/S0375-9474(99)00030-5.

[64] Y. Xu, K. Takahashi, S. Goriely, M. Arnould, M. Ohta, and H. Utsunomiya. NACRE II: an update of the NACRE compilation of charged-particle-induced thermonuclear reaction rates for nuclei with mass number A¡16. *Nucl. Phys. A*, 918:61–169, November 2013. doi: 10.1016/j.nuclphysa.2013.09.007.

[65] F. C. Barker. Calculation of the ^{13}N(p,γ)^{14}O cross section at low energies. *Australian Journal of Physics*, 38(5):657–670, January 1985. doi: 10.1071/PH850657.

[66] F. Riess, P. Paul, J. B. Thomas, and S. S. Hanna. Lifetimes of Levels in ^{12}C, ^{13}C, and ^{13}N. *Physical Review*, 176(4):1140–1146, December 1968. doi: 10.1103/PhysRev.176.1140.

[67] H. O. Meyer, G. R. Plattner, and I. Sick. Elastic p+^{12}C scattering between 0.3 and 2 MeV. *Zeitschrift fur Physik A Hadrons and Nuclei*, 279(1):41–45, March 1976. doi: 10.1007/BF01409090.

[68] S. Mazzoni, M. Chiari, L. Giuntini, P. A. Mandò, and N. Taccetti. Proton elastic scattering cross section on carbon from 350 keV to 3 MeV. *Nuclear Instruments and Methods in Physics Research B*, 136(1-4):86–90, March 1998. doi: 10.1016/S0168-583X(97)00678-2.

[69] Liu Zhengmin, Li Beijing, Duan Zhenzhong, and He Huimin. Cross section measurements for 170° backscattering of protons from carbon in the energy range 0.3-3.0 MeV. *Nuclear Instruments and Methods in Physics Research B*, 74(3):439–442, May 1993. doi: 10.1016/0168-583X(93)95977-D.

[70] S. V. Artemov, R. Yarmukhamedov, N. Burtebayev, B. K. Karakozov, F. Kh. Ergashev, Maulen Nassurlla, S. B. Igamov, N. Amangeldi, A. Morzabayev, J. Burtebayeva, V. S. Zhdanov, G. Yergaliuly, E. Piasecki, K. Rusek, S. B. Sakuta, A. Demyanova, O. R. Tojiboev, A. Trzcińska, A. Sabidolda, R. Khojayev, K. I. Tursunmakhatov, Marzhan Nassurlla, M. Wolińska-Cichocka, T. Kh. Sadykov, and N. Saduyev. Asymptotic normalization coefficient for ^{12}C +p $\rightarrow^{13}$N from the ^{12}C (^{10}B ,^{9}Be) ^{13}N

reaction and the ^{12}C (p ,γ) ^{13}N astrophysical S factor. *European Physical Journal A*, 58(2):24, February 2022. doi: 10.1140/epja/s10050-021-00652-z.

[71] Zhihong Li, Jun Su, Bing Guo, Zhichang Li, Xixiang Bai, Jiancheng Liu, Yunju Li, Shengquan Yan, Baoxiang Wang, Youbao Wang, Gang Lian, Sheng Zeng, Ertao Li, Yongshou Chen, Nengchuan Shu, Qiwen Fan, and Weiping Liu. Determination of the ^{12}C(p, γ)^{13}N reaction rates from the ^{12}C(^{7}Li,^{6}He)^{13}N reaction. *Science China Physics, Mechanics, and Astronomy*, 53(4):658–663, April 2010. doi: 10.1007/s11433-010-0128-8.

[72] S. V. Artemov, A. G. Bajajin, S. B. Igamov, G. K. Nie, and R. Yarmukhamedov. Nuclear asymptotic normalization coefficients for ^{14}N $\rightarrow$ ^{13}C + p configurations and astrophysical S factor for radiative proton capture. *Physics of Atomic Nuclei*, 71(6):998–1011, June 2008. doi: 10.1134/S1063778808060045.

[73] A. M. Mukhamedzhanov, A. Azhari, V. Burjan, C. A. Gagliardi, V. Kroha, A. Sattarov, X. Tang, L. Trache, and R. E. Tribble. Asymptotic normalization coefficients from proton transfer reactions and astrophysical /S factors for the CNO ^{13}C(p,/γ)^{14}N radiative capture process. *Nucl. Phys. A*, 725:279–294, September 2003. doi: 10.1016/S0375-9474(03)01618-X.

[74] Suprita Chakraborty, Richard deBoer, Avijit Mukherjee, and Subinit Roy. Systematic R -matrix analysis of the ^{13}C(p ,γ)^{14}N capture reaction. *Phys. Rev. C*, 91(4):045801, April 2015. doi: 10.1103/PhysRevC.91.045801.

[75] D. F. Hebbard and J. L. Vogl. Elastic scattering and radiative capture of protons by C ^{13}. *Nuclear Physics*, 21:652–675, December 1960. doi: 10.1016/0029-5582(60)90084-5.

[76] Edmund A. Milne. Energy Levels in N^{14} from the Scattering of Protons by C^{13}. *Physical Review*, 93(4):762–767, February 1954. doi: 10.1103/PhysRev.93.762.

[77] C. D. Latorre and J. M. Irvine. The structure of ^{14}N and ^{16}O. *Nucl. Phys. A*, 188(3):524–534, July 1972. doi: 10.1016/0375-9474(72)90217-5.

[78] W. Galster, P. Leleux, I. Licot, E. Lienard, P. Lipnik, D. Mertens, T. Delbar, J. Vervier, P. Decrock, M. Huyse, P. van Duppen, P. Duhamel, J. Vanhorenbeeck, G. Roters, C. Rolfs, U. Schroeder, H. P. Trautvetter, K. Wolke, J. Lambert, and W. S. Rodney. Target and detection techniques

for the ^{13}N(p,γ)^{14}O reaction using radioactive ion beams: ^{13}C(p,γ)^{14}N reaction as a test case. *Phys. Rev. C*, 44(6):2776–2787, December 1991. doi: 10.1103/PhysRevC.44.2776.

Acknowledgements

I would like to express my heartfelt gratitude to the following people who have played a pivotal role in my journey towards the completion of this PhD thesis. First and foremost, I extend my deepest appreciation to my supervisor, Antonio Caciolli, for his unwavering guidance, unyielding support and tireless encouragement throughout these years. Your dedication to pushing me beyond my limits has been essential in shaping my academic growth. I also want to thank Denise Piatti for her invaluable assistance and for infusing moments of laughter and discussions. You have added a touch of joy to this demanding journey. My sincere appreciation goes out to Axel Boeltzig, whose mentorship has provided me with a immeasurable wealth of knowledge about both experimental setups and data analysis. Your meticulous and composed approach to research has been a constant source of inspiration and forever will be. I am profoundly grateful to Eliana, with whom I shared meaningful discussions about our mental health challenges. Our chats have been a source of solace during the difficult phases of this academic pursuit. I extend my thanks to the entire LUNA collaboration for their guidance and the invaluable opportunity they provided me to learn and grow. Your collective wisdom and support have enriched me immensely. To my family, I owe an immense debt of gratitude. Your belief in me and your willingness to let me embark on this challenging journey have been the cornerstones of my success. Lastly, I want to express deepest gratitude to my better half, Luana. Your constant support, love and understanding have been my anchor throughout this academic odyssey. Your presence has illuminated the darkest moments and made the brightest ones even more beautiful.

To all of you, I am indebted for your contributions to my academic and personal growth. This thesis would not have been possible without your support and encouragement.